

Self-Assembly of Complex Structures through Competing Entropic and Enthalpic Patchiness

by

Jaime A. Millan

A dissertation submitted in partial fulfillment
of the requirements for the degree of
Doctor of Philosophy
(Materials Science and Engineering)
in The University of Michigan
2015

Doctoral Committee:

Professor Sharon C. Glotzer
Research Investigator Michael Engel
Professor Nicholas A. Kotov
Professor Chris B. Murray
Associate Professor Anish Tuteja

© Jaime A. Millan 2015
All Rights Reserved

TABLE OF CONTENTS

LIST OF FIGURES	v
ABSTRACT	xix
CHAPTER	
I. Introduction	1
1.1 Nanotechnology	1
1.1.1 Self-assembly	3
1.1.2 Ordering by shape entropy	5
1.1.3 Patchy interactions <i>via</i> van der Waals forces	7
1.1.4 Objectives	8
1.1.5 Thesis organization	8
II. Numerical methods and enthalpic interaction model	10
2.1 Introduction	10
2.1.1 Monte Carlo method	11
2.1.2 Metropolis algorithm	12
2.1.3 Free energies of crystals	15
2.1.4 Interaction model	17
III. Competition of shape and interaction patchiness for self-assembling nanoplates	19
3.1 Abstract	19
3.2 Introduction	20
3.3 Results and discussion	21
3.3.1 Synthesis	21
3.3.2 Monte Carlo simulation of hard plates	26
3.3.3 Density functional theory calculations	34
3.3.4 Interaction asymmetry between nanoplate edges	35
3.3.5 Conclusions	38

IV. Effect of shape transformations on the self-assembly of faceted patchy nanoplates with irregular shape into tiling patterns .	45
4.1 Abstract	45
4.2 Introduction	46
4.3 Model and method	50
4.4 Shape transformation	51
4.5 Results	54
4.5.1 Faceting	56
4.5.2 Pinching	57
4.5.3 Elongation	63
4.5.4 Truncation	65
4.6 Discussion	68
4.7 Conclusion	83
V. Self-assembly of Archimedean tilings with enthalpically and entropically patchy polygons	84
5.1 Abstract	84
5.2 Introduction	85
5.3 Model and approach	88
5.4 Results	90
5.4.1 Entropic interactions	91
5.4.2 Symmetric Enthalpic interactions	95
5.4.3 Shape-Specific Enthalpic interactions	99
5.4.4 Edge-Specific Enthalpic interactions	103
5.5 Discussion	104
5.6 Conclusion	106
VI. Shape alloys of nanorods and nanospheres from self-assembly	108
6.1 Abstract	108
6.2 Introduction	109
6.3 Numerical and analytical approach	112
6.3.1 Determination of densest spherocylinder-sphere packings	112
6.3.2 Numerical method	113
6.3.3 Interaction model	113
6.4 Results	114
6.5 Densest rod-sphere packings	117
6.6 Monte Carlo simulations of the hard spherocylinder-sphere system	118
6.6.1 Short-range attractive interactions	123
6.6.2 Role of relative interaction strength	128

6.7	Conclusions	129
VII.	Conclusion and outlook	130
7.1	Conclusions and outlook	130
7.1.1	Outlook	133
7.1.2	Towards complex structures in two-dimensional tilings	133
7.1.3	Two-dimensional melting of hard and sticky with irregular shape	134
7.1.4	Three-dimensional self-assembly from sticky polyhedral particles	135
BIBLIOGRAPHY	137

LIST OF FIGURES

Figure

- 1.1 Representative examples of the new generation of anisotropic colloidal building blocks with varying size (left to right) and anisotropy type (top to bottom). 4
- 2.1 Potential of mean force *vs.* facet separation between tip-to-tip hexagonal prisms. Each hexagonal facet is modeled with a United Atom model where nanocrystal and ligand molecules are represented by pseudoatoms that interact *via* Lennard-Jones potential and for the case of the oleic acid molecules bonding, stretching, bond bending are included. Multiple simulations starting from different configurations corroborate the Lennard-Jones-like shape of the interaction potential. 18
- 3.1 Synthesis and structural characterization of monodisperse lanthanide fluoride nanocrystals. (a) Schematic representation of the synthesis method. (b) General trend of stable phases from trigonal LnF_3 to orthorhombic LnF_3 and to tetragonal LiLnF_4 phases as a function of the type of lanthanide ions. Experimental results for Eu^{3+} and Ho^{3+} show the possibility of coexisting phases. (c) Powder XRD patterns of different LnF_3 and LiLnF_4 nanocrystals. (d-i), HRTEM images of NdF_3 (d), DyF_3 (e), TbF_3 (f), TbF_3 (g), DyF_3 (h), EuF_3 (i) nanoplates. Scale bars: (d,e,h) 5 nm, (f,g,i) 10 nm. 22

3.2	<p>Two-dimensional superlattices self-assembled from lanthanide fluoride nanoplates. (a-c) Parallel arrangements of DyF₃ rhombohedral nanoplates (a), small aspect ratio TbF₃ hexagonal nanoplates (b), and EuF₃ large aspect ratio hexagonal nanoplates (c). (d-e) Alternating arrangements of intermediate aspect ratio hexagonal nanoplates of composition DyF₃ (d) and TbF₃ (e). TEM images (left), wide-angle (upper right) and small-angle (lower right) electron diffraction patterns. f, Dark-field TEM image taken from the same area as shown in e. All scale bars in (a-f) represent 100 nm. (g-h) AFM three-dimensional topography images of EuF₃ (g) and TbF₃ (h) nanoplate superlattices. The scan sizes are 450 nm x 450 nm (g) and 500 nm x 500 nm (h).</p>	25
3.3	<p>(a) Monte Carlo simulations of hard polygonal plates. The geometry of the particles is characterized by the opening angle $\alpha = 68^\circ$ and the two edge lengths A and B parallel to (101) and (001), respectively. (b) Alternating arrangements are only space-filling for B/A = 0 and B/A = 1 and otherwise have voids. This is apparent in the densest packings as a function of aspect ratio. Parallel arrangements are always space-filling. (c-e) Final particle configurations assembled in simulation from disordered starting configurations. Simulation conditions mimic experimental conditions for nanoplate assembly. The particles assemble into the parallel arrangement for all choices of the edge ratio; shown are B/A = 0 (d), B/A = 1 (e), B/A = 2 (f). Due to periodic boundary conditions, structural defects in the form of twin layer (T), partial dislocations (P), dislocation (D), and vacancies (V) remain in the system. Similar defects are also frequently observed in experiments.</p>	27
3.4	<p>Self-assembly of hard rhombs with opening angle $\alpha = 68^\circ$. Hard rhombs self-assemble into a parallel tiling. Here the pressure is slowly increased during several tens of millions MC cycles. Starting from the disordered initial state (a) the system orders locally (b). (c) The order slowly grows until most of the rhombs are oriented identically. Chain-like stacking faults are frequently observed. (d) The stacking faults disappear very slowly by rotational jumps of the rhombs. Diffraction images are shown on the right hand sides of the subfigures.</p>	29
3.5	<p>(a-b) The assembly of slightly elongated hard rhombs of irregular hexagonal shape. (a,b) The irregular hexagons assemble much faster than rhombs, because stacking faults can only occur in connection with small vacancies. (c,d) The system again forms a parallel arrangement. Growth is fastest along the long symmetry axis of the particles.</p>	30

3.6	Assembly of equilateral elongated rhombs with $B/A = 1.0$. These irregular particles can assemble equally well into a parallel space-filling tiling or an alternating space-filling tiling. Without interactions, the particles entropically prefer the parallel arrangement. The simulation is run at constant pressure.	31
3.7	(a-d) Strongly elongated hexagons align quickly and assemble into the parallel pattern. Stacking faults have relatively low angles and single domains can be obtained robustly in simulation.	32
3.8	Free energy difference $\Delta F_{AP} = F_{Alt} - F_{Para}$ between the alternating and the parallel pattern for hard (a) rhombi with $B/A=0$ and (b) equilateral elongated hexagons with $B/A = 1.0$. Both plots show a positive free energy difference, which demonstrates that the parallel arrangement is more stable than the alternating pattern. The free energy difference is in the range 0.045 ± 0.015 over the stability regime of the crystal and increases linearly with packing fraction. Different size initial configurations were chosen to test for finite size effects. The free energy calculation employs the Frenkel-Ladd method. (c) Melting and crystallization curves sketching out the hysteresis around the fluid-solid transition for hard irregular hexagon with $B/A = 1$. From the jump in the inverse packing density $\Delta\phi^{-1}$ and the transition pressure P_{melt}^* we estimate the jump in entropy between fluid and solid, $S_{melt}/k_B = P_{melt}^* - 1$, to be 1.7 ± 0.1	33
3.9	Atomic structure of DyF_3 surfaces. Density functional theory calculations reveal the structure of (a,b) the (001) surface and (c,d) the (101) surface. The figure shows pristine surfaces in top view (a,c) and surfaces with adsorbed oleic acid viewed from the side (b,d). The depicted atoms are Dy (grey), F (green), C (black), O (red), and H (white). The dashed squares in (a,c) are primitive unit cells on the surfaces. Letters A, B, C and D indicate different types of surface Dy atoms that have less nearest neighbor F atoms than bulk Dy atoms. For each bulk Dy atom, there are 9 nearest neighbor F atoms. On the (001) surface, this number is 7 for A and 8 for B, and on the (101) surface both C and D have 7 nearest F atoms.	36
3.10	Modeling interacting rare earth fluoride nanoplatelets. Oleic acid tethers cause an effective interaction of nanoplatelet edges. The interaction strength depends on the orientation angle θ , the shift d_{II} parallel to the bisector of the two edges, and the normal distance d_{\perp} perpendicular to the bisector.	37

3.11	Modeling and simulation of interacting lanthanide fluoride nanoplates. (a) Oleic acid tethers cause an effective attraction of nanoplate edges that is asymmetric with respect to the two edge types A and B. (b) The phase diagram as a function of edge length ratio obtained from Monte Carlo simulations shows the stability regions of the parallel arrangement and the alternating arrangement. An interaction asymmetry greater than zero is required to stabilize the alternating arrangement. Error bars span from the lowest ϵ that exclusively forms the alternating arrangement to the highest ϵ that exclusively forms the parallel arrangement. (c-e), Simulation results for the interaction asymmetry $\epsilon = 0.2$ demonstrate the formation of the alternating arrangement (from left to right: early, middle, and late stage assembly). (f-l), Electron microscopy snapshots in original contrast (f,i) and colored using image processing (g,k) are compared to simulation results (h,l). A close similarity of the local order is apparent for $B/A = 0$ (f-h) and $B/A = 1$ (i-l).	39
3.12	Equilateral elongated rhombs with an interaction that prefers the alternating tiling. (a-b) The attraction between edges of different type (A-B) is stronger than the attraction between edges of the same type (A-A and B-B) as observed in the experimental systems of LnF_3 nanoplates. Interaction speeds up the assembly compared to the hard systems. Between (c) and (d) the biggest crystalline grain takes over the whole simulation box. Note that in (d) one stacking fault still remains. This stacking fault cannot heal because of the periodic boundary conditions.	40
3.13	(a) TEM image of a multicrystalline state of TbF_3 plates.(b) Coloring the plates based on their orientation using image analysis tools helps identifying coexisting grains. The plates assemble robustly into the alternating tiling. Note that impurities are abundant on the grain boundaries. (c) In the simulation of a large system (5000 particles), the formation of multiple grains with alternating patterns was also observed. This figure is a larger version of the subfigures 3.11 i,k,l.	41
3.14	Comparison of experiment (a,b) and simulation in a larger system of interacting rhombs (c). (a) The TEM image shows the existence of multiple grains. (b) The experimental image is colored with an image analysis code. The orientation of rhombs is detected automatically by determining the inertia tensor. A clear tendency for forming parallel arrangements can be observed. (c) A large (5000 rhombs) simulation with interacting rhombs. The interaction makes it harder for the rhombs to crystallize. This figure is a larger version of the subfigures 3.11 f,g,h.	42

3.15	Representative TEM images of (a) DyF ₃ rhombohedral nanoplate, (c) TbF ₃ nanoplate and (e) DyF ₃ nanoplate superlattices and the corresponding (b, d and f, respectively) statistical analysis of interparticle distance. A denotes ($\{101\}$ facets and B denotes ($\{101\}$ facets. For each histogram, at least two hundred measurements are carried out. It is noteworthy that in both alternating configuration (c and e), each nanoplate is surrounded by nearly uniform interparticle separations (2 A-A contacts and 4 A-B contacts).	43
4.1	Shape transformations for nanoplates. The first column corresponds to the classification of experimentally observed shape transformations corresponding to faceting, pinching, elongation, and truncation. The second column depicts the effect of each transformation on particle shape. Experimental examples of each transformation are shown in the third column. The faceting shape transformation is shown for silver nanoplates ¹ . The pinch transformation is shown for the growth of a silver triangular nanoplate on a nanorod ² . The elongation transformation is shown for uranium oxide hydroxide hexagonal nanoplates ³ . The truncation transformation is shown for hexagonal and triangular nanoplates ⁴	49
4.2	(a) The interactions between the nanoplates is edge-to-edge and scales linearly with d_{para} , quadratically with d_{per} and quadratically with orientation angle θ . (b) Pinching alters the shape of the nanoplates continuously by translating inwardly or outwardly a single vertex along the radial direction.	52
4.3	Schematics of the pinching, truncation and elongation shape transformation. (a) Pinching modifies the shape of a regular polygon continuously by translating a single vertex inwardly or outwardly along the radial direction (axis connecting vertex i and particle center O). (b) Elongation is achieved by rescaling the length (l') of a pair of opposite edges (red arrows) with initial length l_o . Left, mid- and right panels correspond to the cases when ($\zeta = 0, 0.5$) and 1. (c) Left panel shows vertex i and unitary vectors (\hat{a}_1) and (\hat{a}_2) along which vertex i splits.	55

4.4	<p>Self-assembly of n-gons. (a) The faceting transformation is summarized by a geometric axis showing the regular polygons. Grey n-gons imply a frustrated assembly, while a colored regular n-gon indicates that shape assembles into a crystal. (b-l) Each snapshot shows a portion, cut from a larger sample containing as many as 1000 nanoplates, of a representative assembly of the nanoplates. The assemblies for the regular n-gon family are (b) the (3^6) Archimedean tiling for the regular triangle, (c) the (4^4) Archimedean tiling for the regular square, (d) a frustrated assembly for the regular pentagon, (e) the (6^3) Archimedean tiling for the regular hexagon, (f) a frustrated assembly for the regular heptagon, (g) the (4.8^2) Archimedean tiling for the regular octagon, (h) a frustrated assembly for the regular nonagon, (i) a sheared rhombic tiling for the regular decagon, (j) a sheared $(3^2.3.4.3)$ Archimedean tiling for the regular undecagon, (k) the (3.12^3) Archimedean tiling for the regular dodecagon, and (l) a sheared $(3^2.3.4.3)$, (l) a sheared $(3^2.3.4.3)$ Archimedean tiling for the regular tridecagon and (m) a center rectangular tiling formed for the regular tetradecagon.</p>	58
4.5	<p>Self-assembled structures from sticky pentadecagons and hexadecagons. (a) Pentadecagons show no global order and (b) hexadecagons exhibit a sheared snub square lattice illustrated by the underlying nearest neighbor bond structure. This structure is similar to the structures self-assembled by hendecagons and tridecagons.</p>	59
4.6	<p>Effect of pinch transformation on the self-assembly of polygons. (a) Faceting vs. pinching phase diagram. Grey n-gons imply a frustrated assembly. The regular n-gons at $\xi = 0.5$ are shown with the symbols and crystal structures observed in Fig 2. The building blocks for each geometric phase point are shown in the geometric phase diagram. Representative snapshots of all crystal structures observed by applying the pinch transformation are shown for the regular polygons between the regular triangle and the regular hendecagon (b-k). The assemblies for the pinched n-gon family are: (b) a shortened kite assembly for $\xi = 0.25$ and $n = 4$, (c) a lengthened kite assembly for $\xi = 0.75$ and $n = 4$, (d) a trapezoidal assembly for $\xi = 0.0$ and $n = 6$, (e) a pentagonal Cairo tiling for $\xi = 0.25$ and $n = 5$, (f) a shifted prismatic tiling for $\xi = 0.25$ and $n = 6$, (g) a alternating triangular tiling for $\xi = 1.0$ and $n = 6$, (h) a dodecagonal quasicrystal for $\xi = 0.25$ and $n = 7$, (i) a $(3^2.4.3.4)$ Archimedean tiling for $\xi = 0.75$ and $n = 7$, (j) a triangular tiling for $\xi = 0.75$ and $n = 8$, (k) a triangular tiling for $\xi = 0.75$ and $n = 9$.</p>	61

- 4.7 Effect of elongation on the self-assembly of polygons. (a) Faceting vs elongation phase diagram. The building blocks for each geometric state point are shown in the geometric phase diagram. Representative snapshots (b-I) of crystal structures self-assembled from elongated polygons that deviate from those formed from regular n -gons ($\zeta = 0.5$) are: (b) a space-filling structure for compressed hexagons ($\zeta = 0.25$) hexagons ($n = 6$), (c) a space-filling structure for elongated ($\zeta = 0.8$) hexagons ($n = 6$), (d) a space-filling tiling formed from fully compressed ($\zeta = 0.0$) octagons ($n = 8$), (e) a stretched (4.8^2) Archimedean tiling for elongated ($\zeta = 0.8$) octagons ($n = 8$), (f) a complex porous structure for fully compressed ($\zeta = 0.75$) decagons ($n = 10$), (g) an oblique porous tiling for elongated ($\zeta = 0.8$) decagons ($n = 10$), (h) a degenerate triangle lattice for compressed odecagons ($\zeta = 0.0$), (i) an Archimedean tiling for elongated ($\zeta = 1.0$) dodecagons ($n = 12$). 66
- 4.8 Effect of truncation on the assembly of polygons. (a) A geometric diagram for the faceting and truncation anisotropy dimensions shows the crystal phases observed. Grey n -gons imply a frustrated assembly. The building blocks for each geometric state point are shown on the phase diagram. Representative snapshots of crystal structures (b-e) observed for truncated polygons that deviate from those structures observed for regular n -gons ($\gamma = 0$). (b) A porous (3^6) Archimedean tiling for slightly truncated ($\gamma = 0.25$) triangles ($n = 3$), (c) Mediterranean tiling for truncated ($\gamma = 0.5$) squares ($n = 4$), (d) dodecagonal quasicrystal at $\gamma = 0.38$ and $n = 7$, and (e) a regular star polygon tiling for truncated ($\gamma = 0.5$) octagons ($n = 8$). 69
- 4.9 A classification of the different tilings observed as a function of shape transformation. (a) A summary of all the transformed polygons (nanoplates) that formed space-filing tilings. Judiciously pinched and non-pinched triangles, squares and hexagons assemble into space-filling tilings. Elongated hexagons formed structures that completely tile the two-dimensional plane. (b) Degenerate and regular porous structures form from truncated triangles, squares, hexagons, heptagons, octagons, nonagons, decagons, hendecagons, dodecagons and tridecagons. Regular octagons, decagons, hendecagons, dodecagons and tridecagons also form long-range ordered porous structures. (c) Complex structures can be assembled from pinched squares, pentagons, hexagons, heptagons, regular decagons, (elongated) hendecagons and tridecagons. 70

- 4.10 Phase behavior of triangles along the shape transformations pinching (ξ) and truncation (γ). Pinching a regular triangle leads towards a transformation from (3^3) Archimedean tilings ($\xi = 0.25$) to oblique lattices ($\xi = 0.50, 0.75$ and 1.0). Slight truncations of triangles nanoplates forms porous triangular tilings. As truncation increases, triangles transform into hexagon, and a transition from triangular tilings towards hexagonal (6^6) Archimedean tilings are observed. At intermediate and higher values values of γ , degenerate $((6^6)$ Archimedean tilings are self-assembled. 73
- 4.11 Phase behavior of squares along the shape transformations: pinching (ξ), truncation (γ) and elongation (ζ). Pinching transforms a squares into a kite leading to the formation of hierarchical kite crystal ($\xi = 0.25$), square (degenerate) Archimedean tilings ($\xi = 0.5$ and 0.5) and alternating hierarchical tilings ($\xi = 0.75$ and 1). Truncation of regular squares leads to the formation of squares lattices ($\gamma = 0.25, 0.5$ and 0.75) and $(4^2.8^2)$ Archimedean tilings ($\gamma = 1.0$). Slight elongation of regular squares leads to the formation of degenerate squares ($\zeta = 0.25$) and of disorder lattices for $\zeta > 0.25$ 74
- 4.12 Phase behavior of pentagons along the shape transformations pinching (ξ) and truncation (γ). Pinching leads to the formation of trapezoidal tilings ($\xi = 0.00$), Cairo tilings ($\xi = 0.25$), frustrated ($\xi = 0.50$) and disorder assemblies ($\xi = 0.75$ and 1.0). Slight truncation of pentagons leads to disorder phases. For higher truncation values, the shape of the truncated pentagons resemble ($\gamma = 0.75$) and become that of decagons ($\gamma = 1.00$), leading to the formation of oblique structures reminiscent of those formed from regular decagons. 75
- 4.13 Phase behavior of hexagons along the shape following transformations: pinching (ξ), truncation (γ) and elongation (ζ). Pinching transforms an irregular pentagon ($\xi = 0.00$) into a pinched hexagon ($\xi = 1.0$). The following structures are observed for the pinching transformation: a prismatic structure ($\xi = 0.00$ and $\xi = 0.25$), a hexagonal (6^6) Archimedean Tilings ($0.25 < \xi = 0.75$) and alternating triangular tilings. Truncation of regular hexagons does not alter the hexagonal tiling but it introduces pores or empty tilings to the self-assembled structure. Elongation transforms rhombs with 60 degrees openings at opposite sides into regular and irregular hexagons. For the (compressed hexagon) rhombs, random tilings are observed and as the elongation transformation modifies rhombs into hexagons, shortened hexagonal (6^6) Archimedean tilings that elongate with the increase of ζ are observed. 76

4.14 Phase behavior of heptagons along the shape pinching (ξ) and truncation (γ) shape transformations. Pinching leads to the formation of disorder tilings ($\xi = 0.00$), dodecagonal quasicrystals ($\xi = 0.25$), frustrated ($\xi = 0.5$) structures, sigma phase ($\xi = 0.75$) and frustrated structures (1.0). Slight truncation of heptagons leads to dodecagonal quasicrystal ($\xi = 0.25$ and 0.5) formation values. The shape highly truncated pentagons starts to resemble ($\gamma = 0.75$) and become that of tetradecagon ($\gamma = 1.0$), leading to the formation of oblique structures reminiscent of those formed from regular decagons. 77

4.15 Phase behavior of octagons along the pinching (ξ), truncation (γ) and elongation (ζ) shape transforms. The following structures are for the observed for the pinching transformation: an ($3^3.4^2$) Archimedean Tiling ($\xi = 0.00$), a (4.8^2) Archimedean tiling ($\xi = 0.25, 0.5$) which is degenerate for $\xi = 0.75$, and a degenerate structure with an underlying triangular tiling ($\xi = 1.00$) and an alternating triangular tilings. Truncation of regular octagons transform Archimedean tilings into star polygon tilings for $\gamma = 0.25$ and 0.5. Further truncations lead to disk behavior. Elongation leads to parallel arrangements (ζ) and elongated ($8^2.4$) Archimedean tiling $\zeta = 0.50, 0.75$ and 1.00. 78

4.16 Phase behavior of nonagons along the shape pinching (ξ) and truncation (γ) shape transformations. Pinching leads to the formation of disorder tilings ($\xi = 0.00, 0.25$ and 0.5), and degenerate triangular lattice ($\xi = 0.75$). Slightly truncated nonagons form disorder structures, and further truncations leads to disk behavior were nonagons form hexagonal degenerate tilings ($\xi = 0.25$ and 0.5). The shape highly truncated pentagons starts to resemble ($\gamma = 0.5$) and become that of tetradecagons ($\gamma = 0.5, 0.75$ and 1.0). 79

4.17 Phase behavior of decagons for the pinching (ξ), truncation (γ) and elongation (ζ) shape transformations. The following structures are for the observed for the pinching transformation: a disorder tilings ($\xi = 0.00$), and parallel lattices ($\xi = 0.25, 0.50, 0.75$) and triangular tilings ($\xi = 1.00$) Truncation (γ) leads to disk behavior. Elongation leads complex porous structures ($\zeta = 0.25$ and 0.5), further truncations leads to (elongated) parallel lattices that resemble structures self-assembled from sticky decagons for $\zeta = 0.50, 0.75$ and 1.00. 80

4.18 Phase behavior of hendecagons for the pinching (ξ) and truncation (γ) shape transformations. Regarding of the amount of pinching applied on the nonagons; a sheared ($3^2.3.4.3$) Archimedean tiling is observed. Slightly truncated nonagons form ($3^2.3.4.3$) Archimedean tiling, and further truncations leads to disk behavior were nonagons form hexagonal degenerate tilings ($\xi = 0.25$ and 0.5, 0.75 and 1.0). 81

4.19	.	Phase behavior of dodecagons for the pinching (ξ), truncation (γ) and elongation (ζ) shape transformations. Regardless of pinching applied on the dodecagons, hexagonal center-to-center tilings are observed. ($\xi = 0.25, 0.50, 0.75$ and 1.00). For intermediate and high pinching (3.12^3) Archimedean tiling are self-assembled. Truncation (γ) leads to disk behavior. Elongation leads to degenerate triangular lattices for compressed dodecagons ($\zeta=0.00$ and 0.25), further truncations leads to (elongated) 3.12^3) Archimedean tiling for $\xi = 0.50, 0.75$ and 1.00	82
5.1	The 11 space-filling Archimedean tilings and published images of representative assemblies of the triangular(3^6), square (4^4), and hexagonal (6^3) AT tilings. Regular tilings: (a) square (4^4), (d) triangular (3^6) and (g) hexagonal (6^3). The experimental images of the regular tilings are (b) (4^4) β -NaYF ₄ AT <i>Ye et al. (2010)</i> ⁵ , (c) NaYF ₄ : Yb/Er (4^4) AT <i>Ye et al. (2010)</i> ⁵ , (e) LaF ₃ (3^6) AT <i>Zhang et al. (2005)</i> ⁶ , (f) Cu _{2-x} Se (3^6) AT <i>Shen et al. (2010)</i> ⁷ , (h) Cu _{2-x} Se (6^3) AT ⁷ , and (i) β -NaYF ₄ (6^3) AT ⁵ . Semi-regular tilings: (j) truncated hexagonal (3.12^2), (k) truncated square (4.8^2), (l) rhombitrihexagonal ($3.4.6.4$), (m) snub square ($3^2.4.3.4$), (n) trihexagonal (or kagome) ($3.6.3.6$), (o) snub hexagonal tiling ($3^4.6$), (p) elongated triangular ($3^3.4^2$), and (q) truncated trihexagonal ($4.6.12$) tilings, which comprise the entire family of Archimedean tilings. In our simulations we consider colored and white polygons as hard nanoplatelets and pores, respectively.	86	
5.2	Schematic indicating the shape-specific interactions between nanoplates used for the shape-selective interaction case. (Left) Each shape is surrounded by a soft shell, which represents the range of the enthalpically patchy interaction. The interaction between the nanoplates is edge-to-edge and short-ranged, and depends on the distance shift $d_{ }$, the normal distance d_{\perp} and angle (θ) between the edges. (Right) Schematic for hexagon-hexagon, hexagon-triangle, and triangle-triangle interaction shows the selectivity of the patchy interaction.	89	
5.3	Representative snapshots of sections of larger simulations for the (3^6), (4^4), (6^3), and (3.12^2) ATs self-assembled with excluded volume interactions only. Insets show the nanoplate, a diffraction pattern of the snapshots, and a compressed close-up. (a) Triangles self-assemble the (3^6) tiling at a packing fraction of 0.90, (b) squares self-assemble the (4^4) tiling at a packing fraction of 0.94, (c) hexagons self-assemble the (6^3) tiling at a packing fraction of 0.93, and (d) dodecagons self-assemble the (3.12^2) tiling at a packing fraction of 0.85.	92	

5.4	(a) Free energy difference between different configurations of hard triangles as a function of density. (b) The effect of shape on the free energy difference at fixed density. The free energy difference is shown as a function of misalignment factor f , which quantifies the edge-edge coverage between two pairs of anisotropic particles. In (a), the free energy gain for edge-edge alignment in triangles is $1.2k_B T$, $1.2k_B T$, $1.5k_B T$, and $1.8k_B T$ at densities fractions 0.5, 0.6, 0.7 and 0.8, respectively. In (b), the free energy gain for edge-edge alignment at packing fraction 0.8 is $2.k_B T$ for triangles, $1.1k_B T$ for square, $0.6k_B T$ for hexagons, and $0.2k_B T$ for dodecagons (b).	93
5.5	Flow diagram representing the design process for the ATs. The paths show how to self-assemble the ATs. Hard interactions are for assemblies that coincide with their densest packings in single component systems. Shape specific patches are for mixtures with lines of alternating building blocks. Mixtures with complex bond networks need edge specific patches. The two rightmost columns show the state-of-the-art in particle synthesis and self-assembly for each corresponding AT.	96
5.6	Hard <i>vs.</i> symmetrically attractive octagons. (a) Hard octagons (upper-right inset) assemble into a hexagonal crystal structure. (b) Symmetric attractive octagons (upper-right inset) form the defect-free (4.8^2) AT where the squares are treated as pores. Both snapshots are accompanied by a diffraction pattern showing long-range order. (C) Truncated square tiling formed from octagons and squares with symmetric attractive interactions in a 1:2 mixture ratio. Excess squares formed the (4^4) square tiling upon further annealing.	97
5.7	Representative snapshots of the design process for the ($3^2.4.3.4$), ($3.4.6.4$), ($3.6.3.6$), ($3^3.4^2$), ($3^4.6$), and ($4.6.12$) ATs. Insets show the design rules and a diffraction pattern. A red halo implies a weakly attractive interaction, while a green halo implies a strong attractive interaction. Left column panels shows symmetrically attractive mixtures of (a) square-triangle, (d) square-hexagon and (g) triangle-hexagon mixtures. Center column panels correspond to the mixtures in the left column with shape-specific patches that readily self-assembles (b) the ($3^2.4.3.4$), (e) ($3.4.6.4$), and (h) ($3.6.3.6$) ATs. Right column panels show shape-specific attractive square-triangle, hexagon-square and hexagon-triangle mixtures that self-assemble the (c) ($3^3.4^2$) tiling, (f) ($4.6.12$) and (i) ($3^4.6$) ATs, respectively.	98

5.8	Phase diagram of packing fraction <i>vs.</i> interaction asymmetry σ for hexagon-triangle mixtures. Symbols represent simulation data points for different asymmetry interaction (shape-specific attraction) and packing fraction values. Each data point represents either the predominantly or always observed phase upon slow annealing (10^7 timesteps) in multiple parallel (five or more) simulations for a given density and interaction asymmetry with systems of 1000 particles.	100
5.9	Simulation results summary. The first column shows the polygons necessary for the assembly of ATs under the design rules proposed. The remaining columns indicate the configurations observed with the different interaction sets.	102
6.1	Self-assembled superlattices of NSs and NRs. Depending on the aspect ratio of the rods and the size ratio of the rods to the spheres, we observe three different phases: (a,d) bulk demixing, (b,e) the lamellar phase with disordered (mobile) spheres, and (c,f) the AB ₂ BNSA with full positional order. TEM images (a-c) are accompanied by theoretical reconstructions (d-f). Scale bars: (a) 25 nm, (b,c) 50 nm.	111
6.2	Geometric parameters for the interaction model. (a) We calculate the interaction of two NCs by MC integration over the surface areas. Here, two spherocylinders (AR = 1.97) are arranged parallel side-by-side. Randomly distributed points on the surface of both spherocylinders (blue and red points) represent the surface elements of the spherocylinders. Points close enough to interact are colored green. (b) We parameterize the relative arrangement of two spherocylinders by the surface-to-surface distance of closest approach, d , (not shown), the projections of the closest points onto the long axis, h_1 and h_2 , and the angle θ between the particle directors u_1 and u_2 .	115
6.3	Plots of the tabulated interaction potentials for spherocylinders with aspect ratio AR = 1.97 and using the interaction kernel described in Methods. (a) Sphere-sphere potential. (b) Spherocylinder-sphere potential. (c,d) Spherocylinder-spherocylinder potential. For the spherocylinder-spherocylinder potential, we show as examples of two different cuts through the 4D parameter space. In (c), spherocylinders are kept parallel, $\theta = 0$, and we set $h_1 = h_2$. In (d), we keep the spherocylinder in contact at their midpoints ($h_1=h_2=0$) and vary their separation and relative orientation. We use the parameterization for the relative arrangement of two spherocylinders specified in Figure 6.2. The relative arrangement of a sphere relative to a spherocylinder is described by a restriction of this parameterization. . .	116

6.4	Densest packings and MC simulations of hard spheres and hard spherocylinders (AR=1.97). (a) Comparison of the packing fractions for the AB ₂ BNSA and for bulk demixing. The AB ₂ BNSA is the densest packing close to size ratio $\gamma = 0.56$. (b) Towards lower ($\gamma = 0.40$) and higher ($\gamma = 0.62$) size ratios, the spherocylinders caps or the spheres, respectively, touch. This introduces additional packing constraints and reduces the packing efficiency. (c) Isotensile MC simulations started from the AB ₂ BNSA show a rapid change in the box aspect ratio Lz/L_x indicative of a transition to the lamellar phase at packing fraction $\phi=0.68$. (d) At $\phi=0.618$, the lamellar phase separates into the rod crystal and a mixed fluid.	119
6.5	Densest packings with buckled interlayers. (a) Unit cells of the AB ₂ BNSA with flat (non-buckled) sphere interlayers at size ratio $\gamma = 0.62$ and with buckled sphere interlayers at $\gamma = 0.63$. (b) Comparison of the packing fractions with and without buckling showing a crossover at $\gamma = 0.6247$. However, for the γ -range shown in the figure, neither arrangement packs as densely as the completely demixed bulk phase.	120
6.6	Densest packing fractions for spheres and rods with curvatures of the caps $\kappa=0.8$. (a), and $\kappa=0.4$ (b). As the curvature is reduced, the packing fraction of the demixed phase increases faster than that of the AB ₂ BNSA. (c,d) Comparison between sheared and non-sheared AB ₂ BNSA for $\kappa=1.0$ (c) and $\kappa=0.8$ (d).	121
6.7	Simulation snapshots of hard spherocylinder-hard sphere mixtures for aspect ratios equal to 1.97 (a) and 2.97 (b). In (a), no global order is observed (nor expected) due to the low aspect ratio. In (b), spherocylinders with higher aspect ratio form monolayers and (smectic) multi-layers, but the order is highly defective. The spheres are mostly separated and demonstrate no clear intention to form sphere-populated interlayers.	122
6.8	a-d) TEM images of rod-sphere BNSAs self-assembled from NaYF ₄ NRs and 11.0 nm Fe ₃ O ₄ NSs. The samples shown in (a) and (b) are formed with a higher total NC concentration in the spreading solution compared to those shown in (c) and (d). (e,f) TEM images of structures self-assembled from CdSe NRs and 5.5 nm Au NSs. The system shows bulk phase separation instead of rod-sphere BNSA formation. Scale bars: (a) 1 μm , (b) 200 nm, (c) 1 μm , (d) 100 nm, (e) 200 nm, (f) 100 nm.	124

6.9	Phase behavior of the spherocylinder-sphere system from MC simulations. (a) Schematic representation of NSs and NRs with molecular ligands. NC interaction is dominated by the attraction of the ligands. Ligand lengths are exaggerated by a factor of about 3 for visualization purposes. (b-e) Reduced pressure PV_0/kT vs. reduced temperature kT/E_{SS} phase diagrams are shown for different values of the rod-sphere attraction asymmetry kT/E_{SS} (see text) at (a,b) $\xi_{RS} = 1.0$, (c) $\xi_{RS} = 1.4$, and (d) $\xi_{RS} = 1.6$. The symbols represent simulation data points. The small region of stability for the AB ₂ BNSA in (a) is magnified and shown in (b). The purple line in (d) represents a possible self-assembly pathway for the assembly of the AB ₂ BNSA from the fluid phase observed in experiment.	125
6.10	Self-assembly simulation of the AB ₂ binary spherocylinder-sphere crystal. (a-c) Time evolution of a simulation of 1536 particles (512 spherocylinders and 1024 spheres) at packing fraction $\phi = 0.58$ and temperature $T = 0.519$ using $\xi_{RS}=1.5$. Snapshot are taken during crystallization after (a) 0.5×10^6 , (b) 1.35×10^6 , and (c) 3.3×10^6 MC sweeps. (d,e) A small part of the system cut out from the simulation demonstrates the local order corresponding to the AB ₂ BNSA. Hexagonal layers of spherocylinders are separated by honeycomb layers of spheres as visible from the side (d) and from the top (e). . . .	126
7.1	Octagonal quasicrystal (left) and P1 Penrose tiling (right).	134

ABSTRACT

Self-Assembly of Complex Structures through Competing Entropic and Enthalpic Patchiness

by

Jaime A. Millan

Chair: Sharon C. Glotzer

With the growing availability of anisotropic particles at different scales, bottom-up self-assembly of such particles is an alternative strategy for the formation of complex structures with promising and applicable collective properties. In particular, particles that exhibit anisotropic shape carrying tunable patchy interactions are of central importance for nanoengineering due to their ability to spontaneously assemble into exotic structures. Inspired by experimental results, in this thesis we present and elucidate the role of entropy in the self-assembly of nanoparticles, and also show the competition between entropic and enthalpic forces at the nanoscale as a mechanism to realize single- and multi-component superlattices with rich phase behavior.

Guided by experimental results, we perform analytical calculations of densest packings and simulations of two-dimensional self-assembly of nanoplates, where we introduce the exact shape of the nanoparticles. Thus, excluded volume effects were correctly introduced in our simulations, which allow for the identification of the role of

packing entropy. These entropic effects proved to be behind the self-assembly of some experimentally observed structures, that are not completely captured in simulation once selective short-range interactions are introduced. Therefore, the rich phase behavior we observe in experiments are the product of the subtle interplay between the entropic and enthalpic forces.

Inspired by advances in particle synthesis, we propose a minimal set of design rules to self-assemble the eleven Archimedean tilings from nanoplates. These design rules are based on the exploitation of the entropic forces that arise solely from nanoplate shapes and on the current ability to program patchy interactions onto modern building blocks. We expect these design rules obtained from anisotropy considerations to guide future experiments that need not be restricted to the nanoscale. Also we show the effect of shape of four particular transformations applied to nanoplates with attractive interactions. These transformations lead to a wide variety of structures that can be categorized into three classes: space-filling, porous and complex structures. We present design rules to obtain each of these structural classes from nanoplates.

Finally, we focus on the three-dimensional co-assembly of nanorods and nanospheres. Our studies were motivated by experimental results that showed three close-packed competing phases: complete bulk-demixing, a lamellar phase and a novel binary co-crystal. We focus on the formation of the binary crystal, which we refer to as a binary crystal shape alloy. Via analytical and numerical calculations we show that this structure is stable at high densities for the given geometrical characteristics of the nanoparticles used in experiments, but its formation is impeded by a natural bulk-demixing at intermediate densities. When we introduce short-range interactions arising from van der Waals effects, the binary system overcomes the demixing trend and forms the shape alloy. Based on regions of stability of the shape alloy and the isothermal experimental protocol, we show that the attraction between nanorods and

nanospheres needs to be favored to self-assemble the shape alloy. These results show that enthalpic forces can cooperate with entropic forces by opening new kinetic pathways and allow the formation of the densest structure.

CHAPTER I

Introduction

1.1 Nanotechnology

Nanotechnology can be defined as the science and engineering that studies the ability to precisely manipulate matter on the atomic, molecular and supramolecular length scales. Initially, the widespread intentions of this engineering discipline was to manipulate atomic and molecular building blocks with desired precision allowing for the synthesis and design of novel and exotic macrostructures. The National Nanotechnological Initiative (NNI) defined nanotechnology as the manipulation of matter exhibiting at least one dimension with size scale between 1 to 100 nanometers. Under this definition, nanotechnology covers multiple recently founded fields such as surface science, organic chemistry, semiconductor physics, among others⁸.

Surprisingly, nanotechnology is not a new engineering discipline since indirect practices of this discipline date back to the Bronze Age. For example, in the Asian continent Japanese artisans were able to manipulate microscopic and macroscopic properties of well-crafted samurai swords implementing smelting and hardening and other processes for its manufacture. From about 800 to 1000 A.D. Vikings manufactured a powerful sword, the "Ulfberht", that was completely mysterious to its enemies. It

was later revealed that these swords were largely made of pure steel. However, these artisans shared no clear understanding of why and how these methods enhanced the desired macroscopic properties of their metallurgic inventions.

It was during the visionary talk "There is Plenty of Room at the Bottom", by Richard Feynman, that the ideas and visions behind nanoscience were initially exposed, to later be further developed by the simultaneous growth of modern atomic theory, experimental procedures, and microscopic techniques. It was the fast-paced emergence of these intellectual pillars that led to the rebirth of nanotechnology and its establishment as a serious and exciting scientific discipline. Precise control at the microscopic scale seemed unachievable. To introduce advances to the field, Richard Feynman concluded his talk with two challenges, offering a prize of 1000 dollars to the first individuals to solve each one. The first challenge involved the construction of a tiny motor that could fit in a 1/64 inch. In less than a year, this was achieved by the meticulous William McLellan, who collected the prize, by using a microscope, a toothpick and a watchmakers lathe. The second challenge demanded the ability of scaling down letters small enough to the point that the entire Encyclopedia Britannica could be fit on the head of a pin. This was achieved in 1985 by Tom Newman, a Stanford graduate student, who successfully scaled down by 1/25,000 the size of the letters of the first paragraph of A Tale of Two Cities. The rapid correct answer to these challenges proved that nanoengineering was a feasible discipline worth pursuing by scientists.

Although the direct intervention of humans during the design of microstructures (*top-down self-assembly*) proved to be successful as mentioned above, the manipulation of many-body systems comprised by building blocks with nanometer-sized dimensions clearly demands the implementation of other techniques. In fact, the solution of Feynman's challenges didn't introduce serious advances to the engineering

of considerably small structures. One strong candidate pathway that became the center of attention in the scientific community in the last decades is self-assembly, namely *bottom-up self-assembly*.

1.1.1 Self-assembly

Self-assembly can be defined as the self-organization of multiple components into patterns or structures in the absence of human intervention⁹. Self-assembly processes involves multiple interacting components with different sizes ranging from the nanometer to the planetary scales in the presence of multiple interactions⁹. As mentioned in Section 1.1, recent progress of hierarchical self-assembly techniques that led to the production of nano- and micro-structure highlights self-assembly as a potential pathway towards the formation of novel patterns that can mimic and, potentially, deviate from those observed in molecular systems. In fact, self-assembly remains as one of the few strategies to form groups of patterns⁹.

Initially, researchers studied self-assembly focusing on the patterns that will formed from a given set of building blocks (forward self-assembly), hoping to being able to identify the governing interactions and thus learn about the self-assembly process. Recently, the scientific community experimented a shift towards the identification of the underlying design rules that will allow us to determine which building blocks would formed the target structure (backward self-assembly).

Inspired by the advent of a new generation of anisotropic building blocks, Glotzer and Solomon¹⁰ proposed that these properties of the building blocks determine the potential of the self-assembly. Thus, a systematic exploration of these anisotropies is imperative and stands as a promising route towards the fabrication of novel structures and identification of generalized design rules. As shown in Figure 1.1, anisotropies

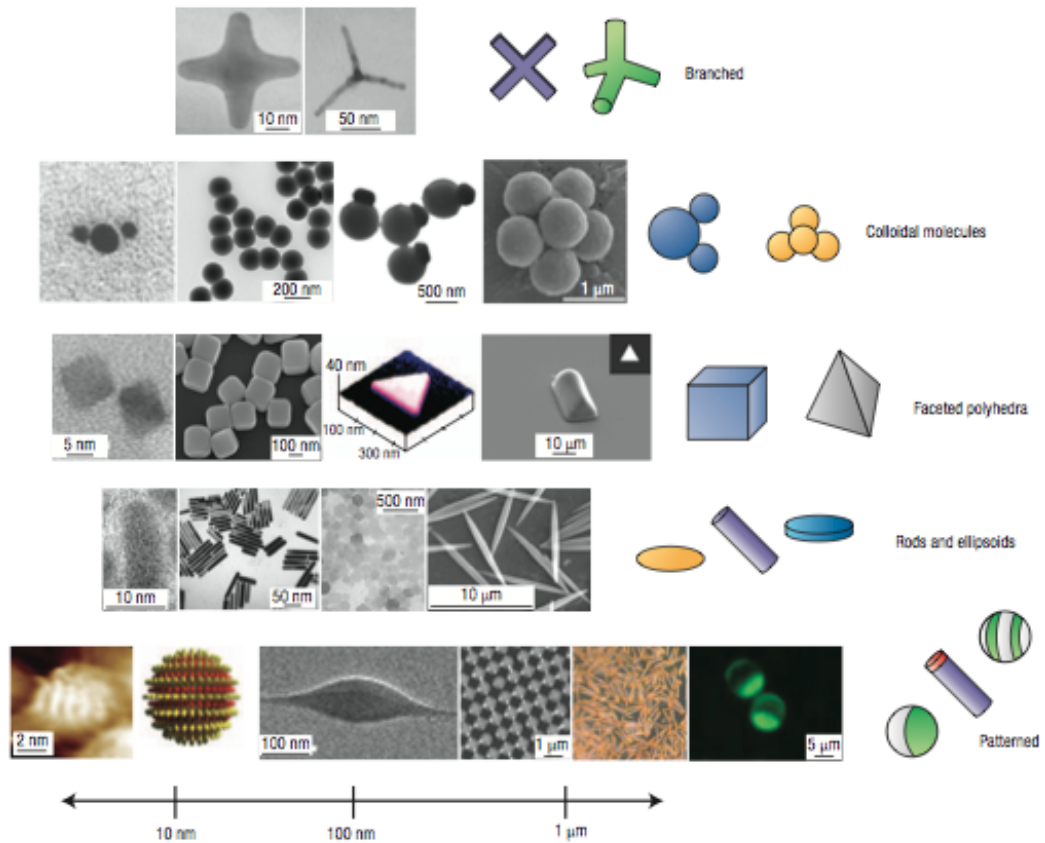


Figure 1.1: Representative examples of the new generation of anisotropic colloidal building blocks with varying size (left to right) and anisotropy type (top to bottom).¹⁰.

come in different flavors, e.g. the shape of the building block can significantly deviate from the isotropic shapes - depending on the dimensions of interest - and adopt anisotropic shapes such as branched or polyhedral shapes, among other. Also, the patterning on the surface of the building block exemplifies another anisotropy dimension that would directly affect the governing interactions during the self-assembly process and thus the final fabrication. If geometry and interaction range and strength relative to particle size and thermal forces govern self-assembly of the building blocks (from micro to nanoparticle), then the above anisotropy dimensions provide a framework for a systematic studying of the particle assembly¹⁰. In fact, this work proves that under the guidance of this framework and experimental results, the subtle interplay between particle geometry (entropic forces) and particle patterning patchiness (enthalpic forces) leads to the formation of complex structures and identification of the underlying design rules that will allow the experimental community to move from discovery to design and fabrication.

1.1.2 Ordering by shape entropy

Ordering by entropy sounds counterintuitive. In 1949¹¹, a seminal publication by Onsager showed unquestionably that as an isotropic fluid of thin hard rods with high aspect ratio - e.g. mosaic tobacco viruses exhibit a hollow rod-like appearance - experiences a gradual increase in concentration, this colloidal system experience a transition to a nematic phase in which the rods exhibit a preferred orientation. In fact, tobacco mosaic virus was the first virus to be successfully crystallized. This was achieved by Wendell Meredith Stanley in 1935¹² who was awarded 1/3 of the Nobel prize 1946 but Stanley incorrectly explained the mechanisms behind the crystallization. Onsager correctly argued that the loss of entropy due to orientational ordering is more than compensated for by the gain in entropy associated with the increase in

free volume in the ordered structure¹¹. Basically, rods arranged in parallel take up less space than do randomly orientated rods, thus providing more accessible space to each rod in the colloidal system.

Entropy as the driving force behind ordering can also be observed with the particles possessing an isotropic shape, namely hard spheres. Kirkwood in 1939 first speculated such a transition which was convincingly revealed in the late 1950's, but this time *via* computational simulations¹³. The explanation was of the same nature: the loss of entropy due to coherent positioning of the sphere is more than compensated for by the gain in entropy associated with the increase in free volume. Again, this type of crystallization constituted an example of entropy-driven crystallization that highlighted the importance of hard interactions arising solely from the shape of the building block in the assembly.

Both types of transitions have been experimentally observed in colloidal model systems and corroborated with computer simulations which also exactly reproduced more crystalline phases such as the smectic-A phase, that arise from entropic forces. The pioneering work of Adams *et al.*¹⁴ shows that binary systems of rods and spheres leads to much richer phase behavior composed of complex binary crystals. These transitions are a manifestation of entropy maximization: the free volume gains from ordered structure more than compensate for positional, orientational, mixing entropic losses associated with bulk demixing. These excluded volume effects induced by the shape of the building blocks, pose challenges to understand the role of entropy in self-assembly that were tackled by Damasceno *et al.*¹⁵.

In a recent numerical study, Damasceno *et al.*¹⁵ studied the role of shape in self-assembly by studying 145 hard convex polyhedra. This ambitious work showed a strong propensity to self-assembly by anisotropic hard particles, at least in simulation time-scales where a wide variety of structures were observed: 22 Bravais and

non-Bravais crystals, 66 plastic crystals, 21 liquid crystals (nematic, smectic, and columnar) and 44 glasses¹⁵. Interestingly, the manifestation of "entropic bonds" which favor the alignment of facets was observed as a product of entropic forces that govern the assembly. Under the proper conditions, these entropic forces can compete or cooperate with other primary or secondary enthalpic forces during the self-assembly of colloids.

1.1.3 Patchy interactions *via* van der Waals forces

The concept of patchy particles was introduced by Zhang and Glotzer⁽¹⁶⁾ which encompassed colloidal particles that exhibit directional interactions strong enough to govern the self-assembly process. This can potentially be achieved with gold-tipped tetrapods that form three-dimensional (3D) arrays through attractive van der Waals interactions¹⁷, and heterogeneous distribution of polymer coating - e.g adsorption of additional polymer at the tips of the tetrapods - will introduce diversity to the phase behavior¹⁸. Thus van der Waals forces obtained from particle patterning stands as potential route to mimic the bond directionality observed in molecular systems.

Van der Waals (vdW) forces are arguably the most ubiquitous interactions in nanocolloids. These forces derive from electromagnetic fluctuations of positive and negative charges in all type of atoms and molecules. Van der Waals forces are responsible for the undesired precipitation of nanoparticles in solutions given that these forces compare a few or hundreds of times with respect to thermal fluctuations. However, with proper manipulation of ligand distribution on the surface of particles or solvent, the vdW forces can be adequately rescaled and act as guiding forces in the assembly process. In general, vdW forces scale linearly with the size of the particle while their range remains constant and of short-range character regardless of increase in particle size¹⁹. Furthermore, theoretical treatment proved that the inter-

action strength necessary to induce particle organization for nanoparticles is of a few $k_B T$. Thus, under proper experimental conditions these forces can overcome entropic penalizations and guide the self-assembly.

1.1.4 Objectives

The objectives of this work are to:

1. Perform computer simulations to elucidate the role of shape entropy in the self-assembly of nanoparticles of two- and three- dimensional systems of single and binary components.
2. Introduce the ubiquitous van der Waals interactions in simulations to capture the interplay between entropic and enthalpic forces to reproduce experimental results.
3. Provide design rules to obtain a wide variety of structures from anisotropic particles.

1.1.5 Thesis organization

This thesis is organized as follows: Chapter 1 describes the motivation and objectives of this work.

Chapter 2 provides the details of the methods and models used in this work. This includes Markovian Chain Monte Carlo (MCMC), Frenkel-Ladd thermodynamic integration, and a description of the interaction model. This chapter discusses the assumptions made to apply these methods.

Chapter 3 discusses the subtle interplay between entropic and short-ranged enthalpic forces under the guidance of experimental assemblies of irregular hexagonal

nanoplatelets that proved to be an ideal model system. Analytical and numerical results confirm that this type of competition arising from particle patterning and shape is behind the experimentally observed patterns. A phase diagram to summarize the results is presented.

Chapter 4 focuses on the effect of a set of shape transformations applied to regular polygons in the presence of short-ranged enthalpic forces. The types of shape transformations are motivated from synthesis progress in the last decade. This systematic study reveals unexpected phase behavior that deviates from previous studies of three-dimensional shapes under the same transformations, and it also exposed a wide variety of assemblies. The observed assemblies are categorized into three groups: porous, complex and space-filling tilings. Finally, design rules to obtain structures belonging to these groups from regular or transformed polygons are presented to guide future experimental work.

Chapter 5 presents the necessary entropic and attractive enthalpic forces necessary to robustly self-assemble all of the Archimedean tilings from polygonal tiles. We briefly motivate our approach on current synthesis results of nanoplatelets. The complexity in the interactions are extracted based on the target structures and their effects on the phase behavior are presented. Ultimately a minimal set of design rules to fully assemble the Archimedean tilings are presented to guide future experimental work.

Chapter 6 summarizes the contributions of this thesis. It also introduces related projects being studied by other group members, and presents future directions in this field.

CHAPTER II

Numerical methods and enthalpic interaction model

2.1 Introduction

This chapter provides the details of the methods and model we implemented in our simulations to produce the self-assembly results and calculation of relative stability between competing structures *via* free energy calculations. Justification for the phenomenological model to capture the enthalpic forces is also provided. The main numerical method we implemented is the Metropolis Monte Carlo algorithm. This methods allow us to reach thermodynamic equilibrium in many body systems and correctly sample their thermodynamic properties. The relative stability of two competing phases is calculated *via* the Frenkel-Ladd method to calculate the relative free energies of these structures²⁰. This thermodynamic integration approach is ideal for the type of structures we encounter in our studies. To capture the enthalpic interactions in our system, namely the van der Waals interactions between the capping molecules, we introduced short-range attractive interactions between pair of edges of different particles. We present justifications for the attractive character and relatively short scale of interactions with respect the particles size for our interaction model.

2.1.1 Monte Carlo method

One of the most successful techniques developed in the last half century for the evaluation and solution of multidimensional integrals is the Monte Carlo Method. Basically, the method consists in randomly taking points in a defined region and then proceeding to evaluate the weighted data as a statistical approach to estimate the value of some integrals. For example, this method could solve the one dimensional integral $S = \int_0^1 f(x)dx$. However, when solving this integral, the Monte Carlo method does not provide any advantage over other approaches (e.g. the trapezoid rule). The reason is that the error form for the Monte Carlo quadrature is :

$$\Delta S \propto \frac{1}{M^{\frac{1}{2}}}, \quad (2.1a)$$

where M is the number of randomly sampled points. In contrast, the trapezoidal rule displays a lower estimated error corresponding to:

$$\Delta S \propto \frac{1}{M^2}, \quad (2.2a)$$

which considerably diminishes as M increases. The true advantages of the Monte Carlo method surfaces in the case of multidimensional (d-dimensional space) integration where the same error preserved its proportional form $1/ M^{\frac{1}{2}}$ and the trapezoid rules estimated error changes to :

$$\Delta S \propto \frac{1}{M^{\frac{2}{d}}}, \quad (2.3a)$$

which significantly greater if the number of dimensions d is greater than 4, which is the case for real many-body systems where the dimensionality is at least $3N$.

2.1.2 Metropolis algorithm

Consider the case in which there are $3N$ data points represented by the tuple $R = (r_1, r_2, \dots, r_N)$, where each r_i is a three-dimensional vector. Imagine that it is desired to calculate the three dimensional integral:

$$S = \int_D G(R) dR, \quad (2.4a)$$

where D is the domain of the integral and the Function $G(R)$ is not a smooth function. Metropolis *et al.*²¹ proposed a quick and innovative way to sample points obtained from a non-uniform distribution. If there is distribution function $P(r)$ that resembles the changes in $G(R)$, fast er convergence can be achieved with:

$$S \simeq \sum_{i=1}^{i=M} \frac{G(R)}{P(R)}, \quad (2.5a)$$

where M is the total number of points of the configurations R_i sampled according to the distribution function $P(R)$. Equation 2.5a can be rewritten as :

$$S = \int_D P(R) F(R) dR, \quad (2.6a)$$

where

$$S = \int_D G(R) dR, \quad (2.7a)$$

From equations 2.5a and 2.7a we conclude that $F(R) = G(R)/P(R)$. Thus, equation 2.6a, is simply a statistical average of $F(R)$. A powerful way to evaluate this statistical average can be obtained via the Metropolis algorithm as presented below.

This approach is based on the assumption that the sampling can be represented by a Markovian process and that the $P(R)$ distribution corresponds to that observed in equilibrated states in a canonical ensemble, that is :

$$P(R) = \frac{e^{-U(R)/k_B T}}{\int e^{-U(R)/k_B T} dR}, \quad (2.8a)$$

Notice that this $P(R)$ depends on the potential energy of the given configuration. In equilibrium, the distribution values between two different states are related by the following expression:

$$P(R)T(R \rightarrow R') = P(R')T(R' \rightarrow R) \quad (2.9a)$$

normally referred as *detailed balance* in statistical mechanic. The transition from one sample point R to R' is accepted if the ratio of the transition rates satisfies:

$$\frac{P(R)T(R \rightarrow R')}{P(R')T(R' \rightarrow R)} = \frac{P(R')}{P(R)} \geq p_i, \quad (2.10a)$$

where p_i is a number obtained from a uniform random number generator and it is between 0 and 1. An outline of the simulation steps in this work can be described as follows. Starting from a configuration $R_0 = (r_1, r_2, \dots, r_N, q_0, q_1, \dots, q_N)$, r_i and q_i correspond to the spatial and orientational coordinates of the set of particles $K = 1, 2, \dots, N$, a new configuration R_1 is created by performing a translational move per particle

$$R_1 = R_0 + \Delta R, \quad (2.11a)$$

$$(2.11b)$$

or by performing an orientational move per particle

$$R_1 = R_0 + \Delta Q, \quad (2.12a)$$

where ΔR and ΔQ are multi-dimensional vectors with component obtained from two distributions $[h_0, -h_0]$ and $[h_1, -h_1]$, respectively. For example:

$$\Delta x_i = h(2\eta_i - 1), \quad (2.13a)$$

and,

$$\Delta q_i = h(2\eta_i - 1), \quad (2.14a)$$

for x and q components of the multidimensional vector r_i . The random variable η corresponds to a uniform distribution between $[0,1]$. The value of h is determined from an acceptance ratio = 0.3. Also the value of h can be changed from shape to shape in binary multi-component systems. We can loop from particle to particle to obtain new configurations that are accepted under the criteria:

$$r = P(R_1)/P(R_0), \quad (2.15a)$$

and r is compared with a uniform random number g_i extracted from the $[0,1]$ set. If $r \geq g_i$, the new configuration is accepted; otherwise it is rejected and the system does not experience a modification. By adopting new configurations a new set A_k is

obtained for $k = n_1, n_1 + n_0, \dots, (M-1)n_0$. When the system has achieved equilibrium, one can evaluate the physical quantity A for each member of the set and obtain an statistical average of A as follows:

$$\langle S \rangle \simeq \sum_{i=0}^{i=M-1} A(R_{n_1+n_0i}), \quad (2.16a)$$

where n_0 and n_1 help to avoid the any spurious effect due to the initial configuration and any correlation between subsequent configurations. Notice that this scheme does not follow a continuous integration as in the case of *molecular dynamics*, where continuous interaction potentials are desired. Strikingly, in the Metropolis algorithm, we need to only calculate the potential energy of configurations, allowing for the implementation of discontinuous potentials. Hence, hard systems can be represented with a pair interaction potential:

$$U_{hard}(ij) = \begin{cases} 0, & \text{if no overlap between particles } i \text{ and } j \text{ exists} \\ \infty, & \text{if overlap between particles } i \text{ and } j \text{ exists} \end{cases} \quad (2.17a)$$

$$(2.17b)$$

2.1.3 Free energies of crystals

In this subsection a thermodynamic method to calculate the Helmholtz free energy of an atomic solid is discussed, where the solid structure of interest is transformed from into an Einstein crystal in a reversible way. This is achieved by coupling the particles to their lattice sites *via* harmonic potentials. If the harmonic potential is strong, the system behave as an Einstein crystal for which the free energy can be calculated exactly. For interacting systems, the free energy of a particular system can

be calculated with the following expression:

$$F = F_{Ein} + \int_{\lambda=1}^{\lambda=0} \left\langle \frac{U(\lambda)}{d\lambda} \right\rangle d\lambda, \quad (2.18a)$$

where $U(r^N)$ is:

$$U(\lambda) = U_0 + \lambda U = U_0 + \lambda \sum_{i=0}^{i=N} (r_i - r_{0,i}^2), \quad (2.19a)$$

where U_0, N and $r_{0,i}$ corresponds to the hard potential, total number of particles and the initial lattice site to which the particles are assigned. In the limit when λ_{max} is sufficiently high, the hard particles stop "touching" each other and the free energy reduces to that of a Einstein crystal. One can then rewrite the free energy of a hard system (F_{hs}) as follows,

$$F_{hs} = F_{\lambda_{max}} + \int_{\lambda_{max}}^{\lambda=0} \left\langle \frac{U(\lambda)}{d\lambda} \right\rangle d\lambda, \quad (2.20a)$$

and after computing the integral between two competing structures A and B , the relative free energy can obtained as follows:

$$\Delta F = F_A - F_B \quad (2.21a)$$

where equation 2.18a is used to calculate the free energy. It is noteworthy to mention that $F(\lambda_{max})$ attains the same value regardless of the system of interest and thus these references would cancel each other in equation 2.21a. Thus one can simply compute the integral $\int_{\lambda_{max}}^{\lambda=0} \lambda$ for competing structures and its difference determines the relative stability between both structures.

2.1.4 Interaction model

The enthalpic interactions in our simulations arise from the van der Waals interaction induced by the coating ligand shell surrounding the nanoparticles. Potential of mean force exhibit a Lennard-Jones-like shape (Figure 2.1). Each nanoplate is modeled as a mathematically hard polygon with short-ranged attractive patches on each edge. In the vicinity of two nanoplates, a pair of edges each with characteristic lengths l_1 and l_2 ($l_1 \geq l_2$) interacts *via* a pair potential that depends on three independent parameters : relative orientation angle θ , parallel shift d_{\parallel} , and normal distance d_{\perp} . In that case, the potential energy can then be written as a product of independent terms so that $V(\theta, d_{\parallel}, d_{\perp}) = \epsilon V(\theta)V(d_{\parallel})V(d_{\perp})$ with attraction strength $\epsilon > 0$, where

$$V(\theta) = 1 - \left(\frac{1 - \cos(\theta)}{1 - \cos(\theta_0)} \right), \quad (2.22a)$$

$$f(d_2) = \begin{cases} l_2, & \text{if } d_{\parallel} \leq (l_1 - l_2)/2 \\ (l_1 + l_2/2 - d_{\parallel}), & \text{if } d_{\parallel} > (l_1 - l_2)/2 \end{cases} \quad (2.22b)$$

$$V(d_{\perp}) = 1 - (1 + d_{\perp}/d_0)^2, \quad (2.22c)$$

for $\cos(\theta) \geq \cos(\theta_0) = 0.95$, $d_{\parallel} < (l_1 + l_2)/2$, $d_{\perp} < 2d_0 = 0.4 l_1$ and 0 otherwise. The attractive interaction strength ϵ can be adjusted to be selective between pair of edges. These characteristic parameters were modified throughout my studies to properly suit the characteristic length scales of current experimental protocols.

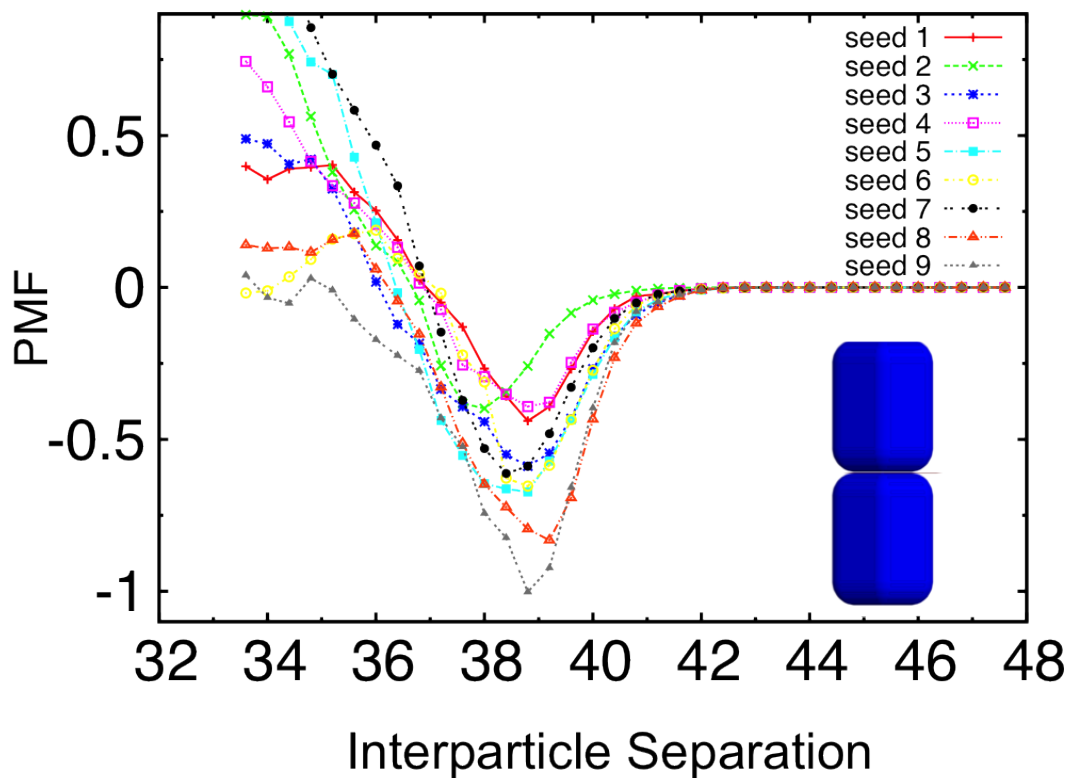


Figure 2.1: Potential of mean force vs facet separation between tip-to-tip hexagonal prisms. Each hexagonal facet is modelled with a United Atom model where nanocrystal and ligand molecules are represented by pseudoatoms that interact via Lennard-Jones potential and for the case of the oleic acid molecule bond bonding, bond stretching, bond bending are included. Multiple simulations starting from different configurations corroborate the Lennard-Jones-like shape of the interaction potential¹⁰.

CHAPTER III

Competition of shape and interaction patchiness for self-assembling nanoplates

The results of this chapter were published in:

X. Ye, J. Chen, M. Engel, J. A. Millan, W. Li, L. Qi, G. Xing, J. E. Collins, C. R. Kagan, J. Li, S. C. Glotzer, C. B. Murray, Competition of shape and interaction patchiness for self-assembling nanoplates, Nature Chemistry, 5, pp 466-473, June 2013

3.1 Abstract

Progress in nanocrystal synthesis and self-assembly enables the formation of highly ordered superlattices. Recent studies focus on spherical particles with tunable attraction and polyhedral particles with anisotropic shape and excluded volume repulsion, but the interplay between shape and particle interaction is only starting to be exploited. Here we present a joint experimental-computational, multi-scale investigation of a class of highly faceted planar lanthanide fluoride (LnF_3) nanocrystals (nanoplates, nanoplatelets). The nanoplates self-assemble in a hexane wetting layer at the liquid-

air interface into long-range ordered tilings. Using Monte Carlo simulation, we demonstrate that the nanoplate assembly can be understood from maximization of packing density only in first approximation. Explaining the full phase behavior requires an interaction specificity of nanoplate edges, which originates from the atomic structure as confirmed by density functional theory calculations. Despite the apparent simplicity in particle geometry, the combination of shape-induced entropic and edge-specific energetic effects directs the formation and stabilization of unconventional long-range ordered assemblies not attainable otherwise.

3.2 Introduction

Nanocrystals often exhibit well-defined facets resulting in a three-dimensional polyhedral shape^{5,10,22–24} or, if crystal growth is suppressed in one direction, in a polygonal two-dimensional (2D) shape^{5,18,24,25}. The assembly of such faceted particles is dominated by driving forces maximizing face-to-face (or, in 2D, edge-to-edge) contact, which is both energetically and entropically favored. Similar to crystals of spherical colloids dominated by inter-particle interactions^{26–31}, even perfectly hard nanocrystals can order without explicit attractive interactions at high enough densities^{32–42}, with recent simulations predicting a rich diversity of entropically-stabilized nanocrystal superlattices¹⁵. Inherent attractive forces between nanocrystals can add further complexity to their assembly. To grow and stabilize nanocrystals in solution, they are coated with ligand molecules^{5,24}, which interact *via* hydrocarbon chains to generate an effective attraction between the nanocrystals. Because crystallographically distinct facets and edges have different atomic structure and density of cationic sites, they can have different densities of ligand molecules and therefore different strength and range of interactions with other facets and edges. Such patchiness of the ligand shell has been observed with DNA surface-bound ligands on gold nanoprisms^{43,44} and

with oleic acid on PbSe nanocrystals⁴⁵, but not yet been exploited for self-assembly of nanocrystal superlattices. The delicate balance between entropic and energetic effects in complex self-assembly processes was highlighted in systems of supramolecular rhombi adsorbed on graphite^{46–48}. In a similar fashion, complex crystalline assemblies should also be obtainable on a larger scale through rational and predictive design by combining entropic and interaction patchiness made possible by the unique shape of nanocrystals. As a demonstration of this fundamental principle, we investigate the spontaneous organization of nanoplates into planar superstructures in a hexane wetting layer at the liquid-air interface. We choose LnF_3 nanocrystals as model systems because of their diverse anisotropic crystal structures and recent advances in the synthesis of lanthanide fluoride nanomaterials^{5,18,49}. A systematic study of nanocrystal growth reveals a correlation between nanocrystal phase stability and lanthanide contraction while yielding a series of monodisperse faceted nanocrystals including circular, rhombic and irregular hexagonal plates as well as tetragonal bipyramids. We demonstrate that the rhombic and irregular hexagonal nanoplates represent a fascinating class of planar nanotiles exhibiting rich and subtle phase behavior.

3.3 Results and discussion

3.3.1 Synthesis

Nanocrystals are synthesized by rapid thermal decomposition of lanthanide trifluoroacetate precursors in the presence of oleic acid as a colloidal stabilizer (Fig. 3.1a). The choice of lanthanide elements and the addition of lithium trifluoroacetate or LiF salts control nanocrystal composition and the evolution of nanocrystal shape: for lighter Ln^{3+} ions (from La to Sm) with larger ionic radii, LnF_3 adopts the trigonal tysonite structure and produces circular nanoplates. However, for heavier Ln^{3+}

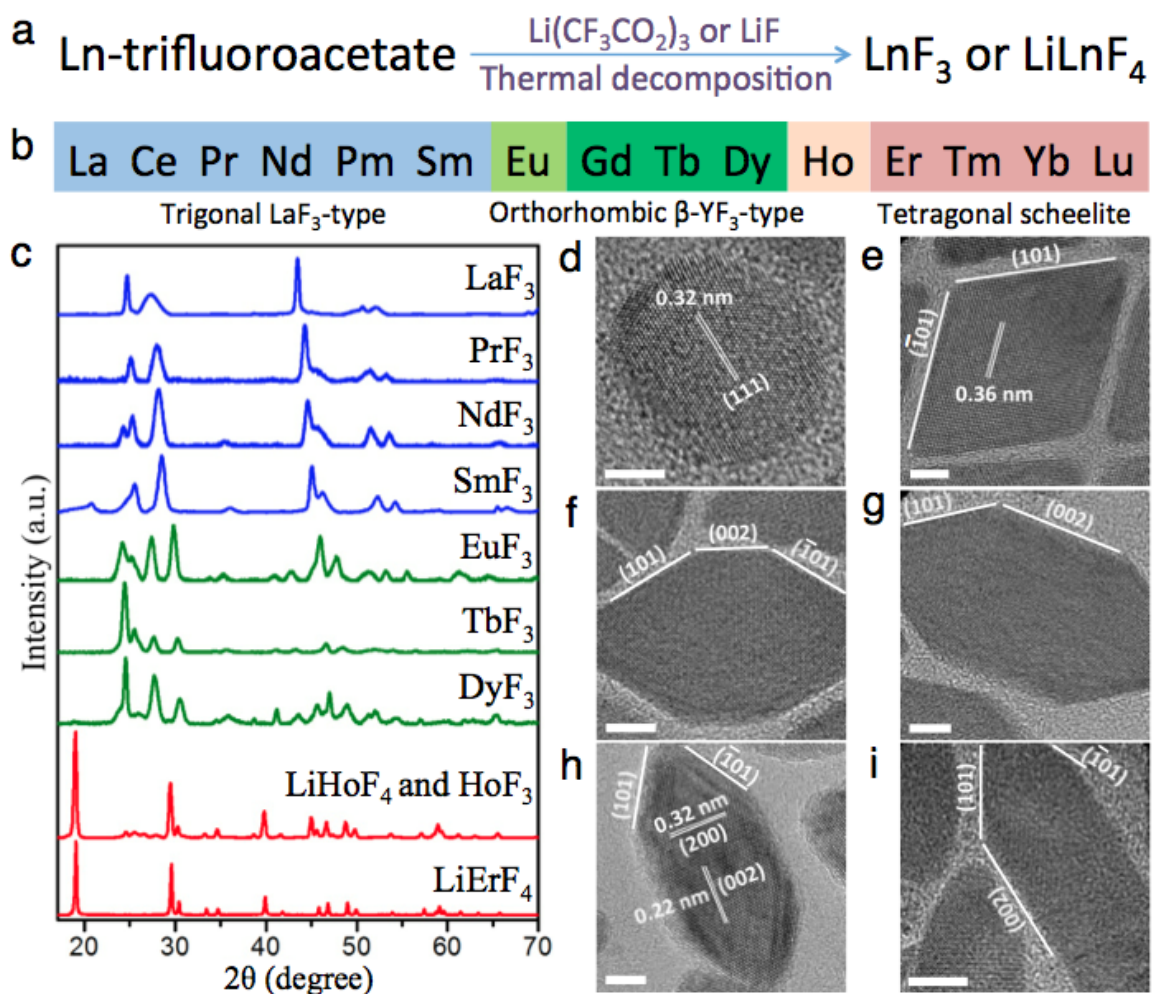


Figure 3.1: Synthesis and structural characterization of monodisperse lanthanide fluoride nanocrystals. (a) Schematic representation of the synthesis method. (b) General trend of stable phases from trigonal LnF_3 to orthorhombic LnF_3 and to tetragonal LiLnF_4 phases as a function of the type of lanthanide ions. Experimental results for Eu^{3+} and Ho^{3+} show the possibility of coexisting phases. (c) Powder XRD patterns of different LnF_3 and LiLnF_4 nanocrystals. (d-i), HRTEM images of NdF_3 (d), DyF_3 (e), TbF_3 (f), TbF_3 (g), DyF_3 (h), EuF_3 (i) nanoplates. Scale bars: (d,e,h) 5 nm, (f,g,i) 10 nm.

ions (Er-Lu), LiLnF_4 (tetragonal scheelite structure) nanocrystals with a tetragonal-bipyramidal-shape are formed. In the middle of the lanthanide series (Ln=Eu-Dy), irregular hexagonal nanoplates with the orthorhombic $-\text{YF}_3$ structure (space group Pnma) are produced as confirmed by powder x-ray diffraction (Fig. 3.1c). High-resolution transmission electron microscopy (HRTEM) images show that each nanoplate is comprised of four symmetry equivalent edges ($\{101\}$ facets) at the tips with an apex angle of $68^\circ \pm 0.5^\circ$, separated by two $\{002\}$ side facets in the middle (Figs 3.1f- 3.1j). The plate shape is further confirmed by HRTEM images of nanoplates standing edge-on. The Ln^{3+} ions dominate the $\{010\}$ planes and therefore we postulate that nanocrystal growth along the $\langle 010 \rangle$ direction is retarded due to oleic acid coordination of lanthanide cations, giving rise to the plate morphology. While systems of four-sided rhombs have been studied before in supramolecular tilings^{46,48,50} and polymeric platelets fabricated by photolithography⁵¹, the irregular six-sided geometry of LnF_3 nanoplates has not yet been reported. Our results overlap with these works only in the boundary case of the 68° rhomb. The lateral dimensions of the irregular hexagonal nanoplates can be adjusted by the choice of lanthanide elements and nanocrystal growth conditions while keeping the plate thickness between 4.5 and 7.0 nm. The lanthanide contraction determines the lanthanide fluoride phase stability: lighter Ln^{3+} ions with larger ionic radii favor a higher coordination number, as evidenced by the fact that eleven fluoride ions surround each Ln^{3+} ion in the trigonal LaF_3 -type structure. As the atomic number of the lanthanide increases, crystal structures featuring lower coordination numbers of nine (orthorhombic $-\text{YF}_3$ type) or eight (tetragonal LiYF_4 -type) dominate⁵², reflecting the effect of cation size and polarizability⁴⁹. Interfacial self-assembly. To study the shape-directed packing behavior of nanoplates, an interfacial assembly strategy is employed^{5,53}. The viscous polar ethylene glycol subphase provides individual nanoplates sufficient mobility even at high particle volume fractions to anneal out defects and access thermodynamically

stable assemblies over extended areas. Face-to-face stacked superstructures have been observed in many plate-like colloids^{18,22,25,54,55} and are often rationalized on the basis of maximization of local packing fraction and van der Waals interactions between neighboring plates. In this work, the nanoplate concentration in the spreading solution is carefully adjusted to ensure that uniform planar 2D superstructures dominate. The as-synthesized nanoplates are subjected to several rounds of purification steps using a solvent/nonsolvent combination to minimize the amount of free oleic acid molecules that may act as depletants and induce lamellar face-to-face stacking during self-assembly.

A library of 2D superlattices self-assembled from rhombic and irregular hexagonal nanoplates of different aspect ratios is shown in Fig. 3.2. For rhombic nanoplates, the superlattices display *cmm* symmetry as manifested by the small-angle electron diffraction pattern (Fig. 3.2a). The clear-cut edges allow the nanoplates to be crystallographically registered in the superlattices, as confirmed by the bright spots in the wide-angle electron diffraction pattern arising from the periodicity of atomic lattice planes. Moreover, point defects or stacking faults are commonly seen in the rhombic nanoplate superlattice, which has been predicted by simulations of random rhombus tiling^{48,50} and observed experimentally in molecular rhombus tilings⁵⁰. Further symmetry breaking of the nanoplates shape anisotropy from rhombus to irregular hexagon offers dramatic packing precision. For nanoplates with either a short or long middle segment ($\{002\}$ side facets) relative to the tip dimension ($\{101\}$ side facets), we observe only a parallel arrangement in which nanoplates pack densely and preferentially align along their $[100]$ axis (Figs 3.2b, 3.2c and 3.2g). On the other hand, for nanoplates with an intermediate middle segment, a striking alternating arrangement resembling the herringbone packing occurs exclusively. Examples are DyF_3 and TbF_3 nanoplates that are similar in aspect ratio but differ in overall dimensions (Figs 2d, 2e and 2h). The simultaneous in-plane positional and orientational ordering of the irreg-

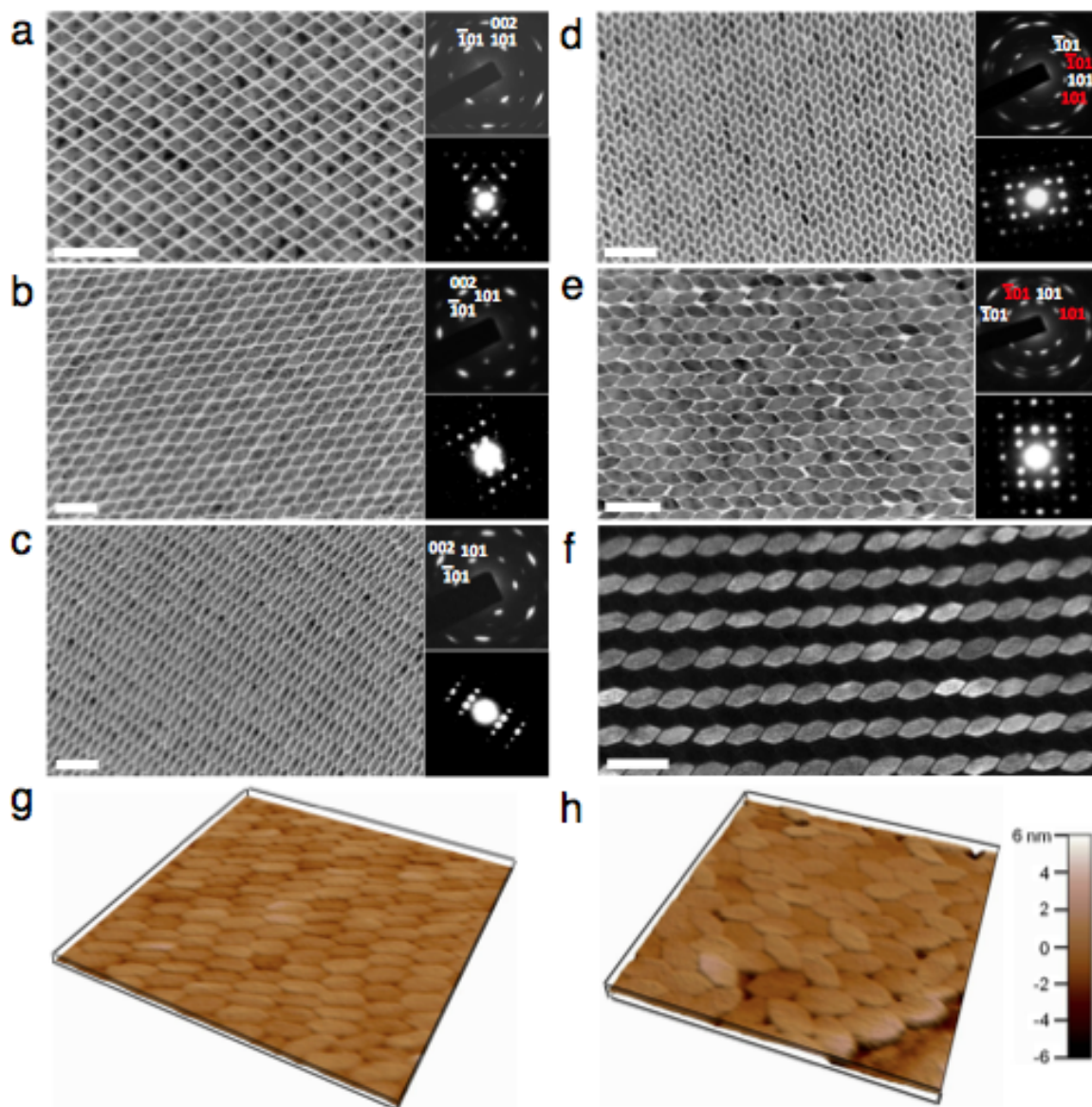


Figure 3.2: Two-dimensional superlattices self-assembled from lanthanide fluoride nanoplates. (a-c) Parallel arrangements of DyF_3 rhombohedral nanoplates (a), small aspect ratio TbF_3 hexagonal nanoplates (b), and EuF_3 large aspect ratio hexagonal nanoplates (c). (d-e) Alternating arrangements of intermediate aspect ratio hexagonal nanoplates of composition DyF_3 (d) and TbF_3 (e). TEM images (left), wide-angle (upper right) and small-angle (lower right) electron diffraction patterns. f, Dark-field TEM image taken from the same area as shown in e. All scale bars in (a-f) represent 100 nm. (g-h) AFM three-dimensional topography images of EuF_3 (g) and TbF_3 (h) nanoplate superlattices. The scan sizes are 450 nm x 450 nm (g) and 500 nm x 500 nm (h).

ular hexagonal nanoplate superlattices is also reflected in the corresponding electron diffraction patterns and, more remarkably, in the dark-field TEM image of the TbF_3 nanoplate superlattice where only one set of evenly spaced linear chains of orientationally invariant nanoplates is visible (Fig. 3.2f). Therefore, unprecedented control over shape monodispersity of the LnF_3 nanoplates provides a unique opportunity to apply shape anisotropy for directing assembly along a preferred pathway.

3.3.2 Monte Carlo simulation of hard plates

To identify the physical mechanism that drives the assembly, we perform Monte Carlo computer simulations of nanoplates constrained to a two-dimensional plane. Such a constraint mimics the experimental conditions during the final stage of the hexane evaporation process, which we interpret as follows. A thin layer of hexane on top of the ethylene glycol solubilizes the nanoplates before the hexane is completely dried. When the thickness of the hexane layer as it evaporates becomes comparable to the largest dimension of an individual nanoplate, the plates are forced to orient horizontally. Since the nanoplates do not clump together face-to-face (maximizing contact) prior to the formation of a single layer, there are likely no strong attractions between them. Only when the hexane layer evaporates further and pushes the nanoplates together are they close enough for their tethers (oleic acid ligands) to interact strongly. This picture is supported by the observation that when the nanoplate concentration is increased in the spreading solution, lamellar face-to-face stacking becomes the dominant structure.

The geometry of the nanoplates is an elongated hexagon characterized by two parameters, the opening angle α and the edge length ratio B/A (Fig. 3.3a). Although the angle is fixed to α by the crystallographic relationships among the nanocrystal facets in the orthorhombic LnF_3 structure, the edge length ratio can be varied from

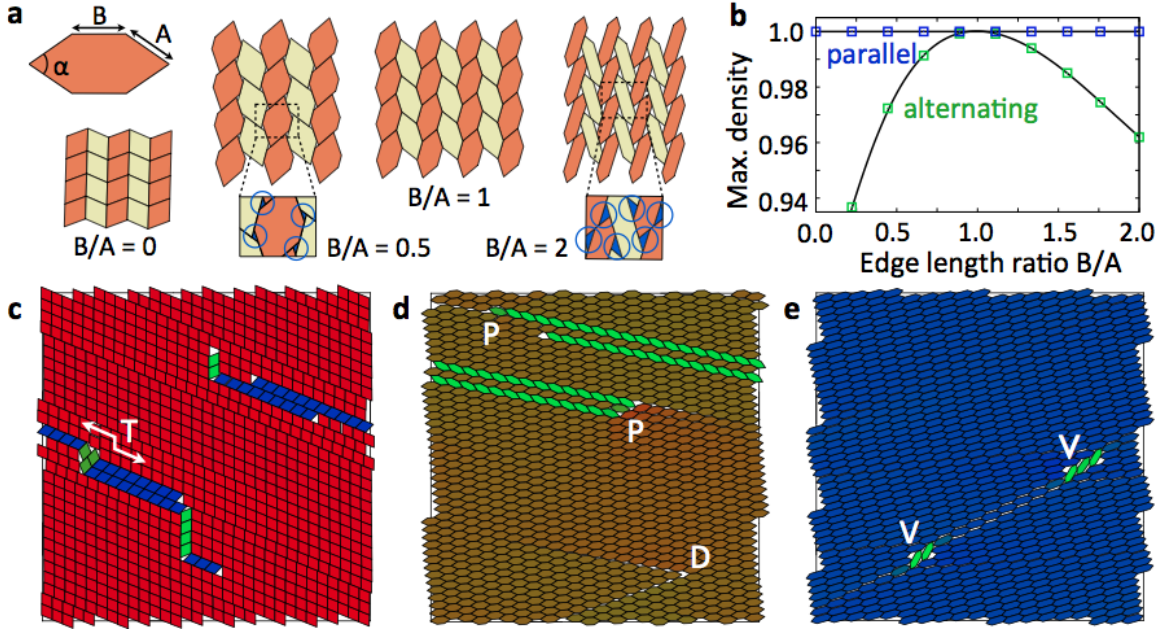


Figure 3.3: (a) Monte Carlo simulations of hard polygonal plates. The geometry of the particles is characterized by the opening angle $\alpha = 68^\circ$ and the two edge lengths A and B parallel to (101) and (001) , respectively. (b) Alternating arrangements are only space-filling for $B/A = 0$ and $B/A = 1$ and otherwise have voids. This is apparent in the densest packings as a function of aspect ratio. Parallel arrangements are always space-filling. (c-e) Final particle configurations assembled in simulation from disordered starting configurations. Simulation conditions mimic experimental conditions for nanoplate assembly. The particles assemble into the parallel arrangement for all choices of the edge ratio; shown are $B/A = 0$ (d), $B/A = 1$ (e), $B/A = 2$ (f). Due to periodic boundary conditions, structural defects in the form of twin layer (T), partial dislocations (P), dislocation (D), and vacancies (V) remain in the system. Similar defects are also frequently observed in experiments.

a degenerate rhomb ($B/A = 0$) to the equilateral elongated hexagon ($B/A = 1$) and a strongly elongated hexagon ($B/A = 2$) through the choice of lanthanide elements and nanocrystal growth conditions. To a first approximation, we consider plates without interaction except excluded volume effects. Hard particle systems maximize entropy during equilibration at constant volume. In the limit of high pressure the plates maximize packing, because the pressure term dominates the entropy term in the Gibbs free energy. While elongated hexagons can fill space for all aspect ratios, the tilings are not always unique. Two candidate structures compete. For all values of B/A , the parallel arrangement is space-filling. Alternating arrangements are space-filling only for $B/A = 0$ and $B/A = 1$ with relative particle rotations of α and $\alpha/2$, respectively. For other edge length ratios, small voids remain between the plates (Figs 3.3a and 3.3b).

We simulate the self-assembly of hard elongated hexagons by slowly compressing the disordered fluid. The compression is chosen to mimic the conditions present during the evaporation process responsible for nanoplate assembly in experiment. We observe that elongated hexagons of all aspect ratios assemble exclusively into single crystals corresponding to the parallel arrangement with few point defects and stacking faults (Figs. 3.3c- 3.3e, 3.4, 3.5, 3.6 and 3.7). The 68° opening angle of the rhombs is important for efficient alignment. For comparison, experiments of rhomb-shaped molecule tiles with an opening angle of 60° on graphite surfaces show a strong tendency for forming a random hexagonal tiling^{46,47}. Indeed, when we simulate 60° rhombs, only random tilings are observed.

The preference of the parallel arrangement is confirmed by free energy calculations. We obtain free energy differences of $F_{alt} - F_{para} = (0.047 \pm 0.005)k_B T$ for both $B/A = 0$ and $B/A = 1$ (Fig. 3.8). The differences depend only slightly on packing fraction and are only 3 of the entropy jump $(T\Delta S)_{melt} = (P\Delta V)_{melt} = (1.7 \pm 0.1)k_B T$ during

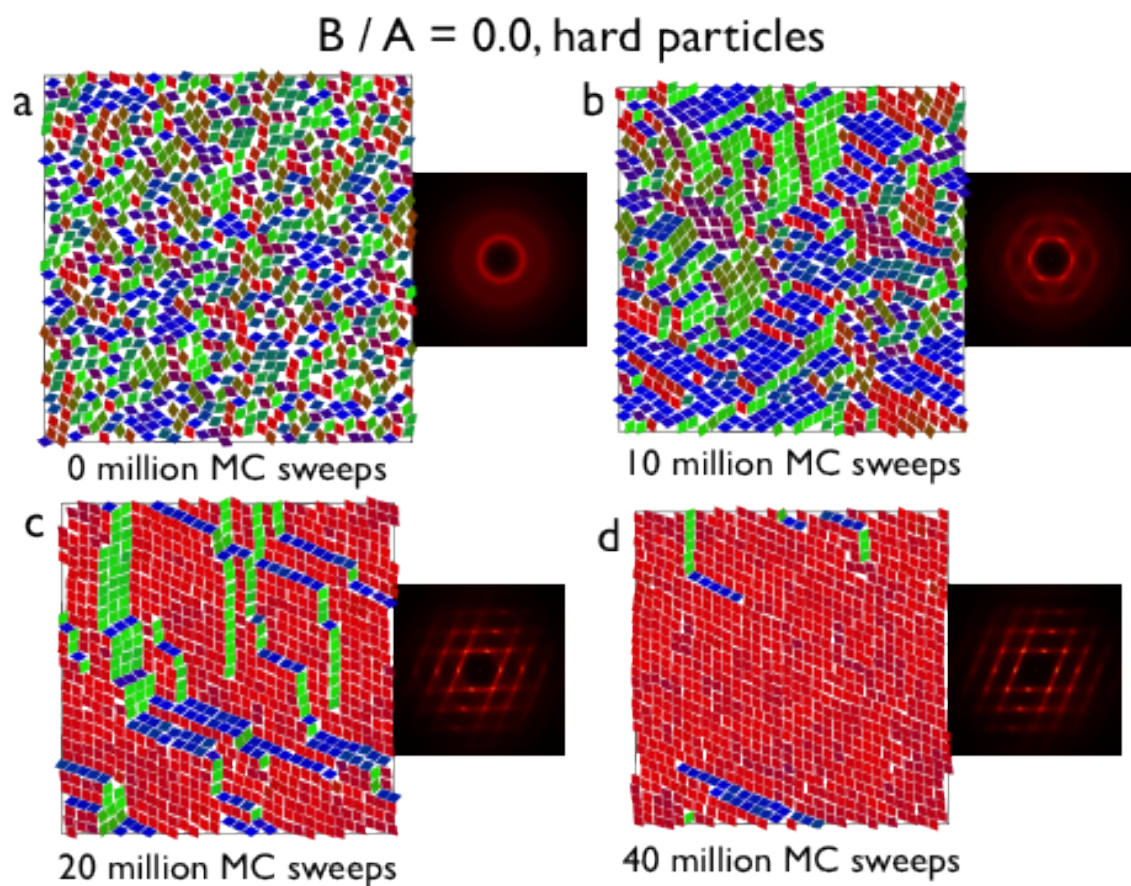


Figure 3.4: Self-Assembly of hard rhombs with opening angle $\alpha = 68^\circ$. Hard rhombs self-assemble into a parallel tiling. Here the pressure is slowly increased during several tens of millions MC cycles. Starting from the disordered initial state (a) the system orders locally (b). (c) The order slowly grows until most of the rhombs are oriented identically. Chain-like stacking faults are frequently observed. (d) The stacking faults disappear very slowly by rotational jumps of the rhombs. Diffraction images are shown on the right hand sides of the subfigures.

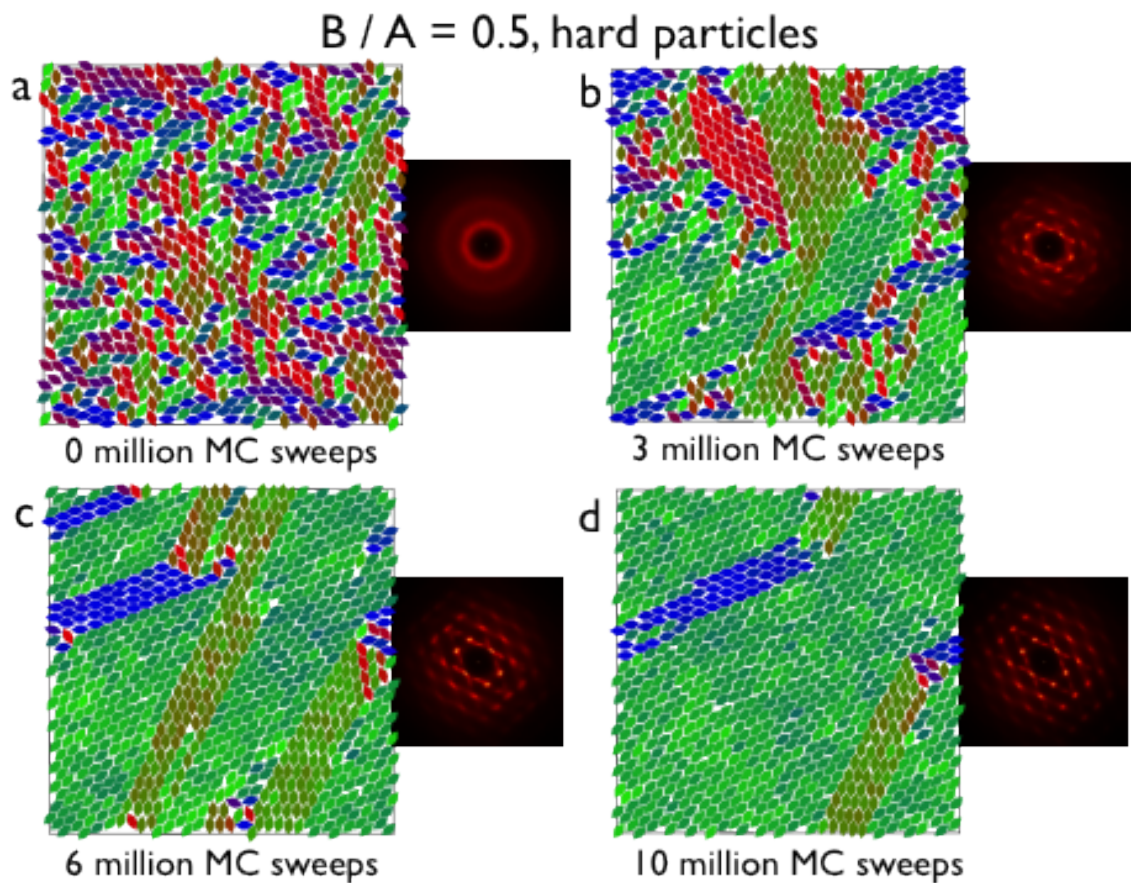


Figure 3.5: (a-b) The assembly of slightly elongated hard rhombs of irregular hexagonal shape. (a,b) The irregular hexagons assemble much faster than rhombs, because stacking faults can only occur in connection with small vacancies. (c,d) The system again forms a parallel arrangement. Growth is fastest along the long symmetry axis of the particles.

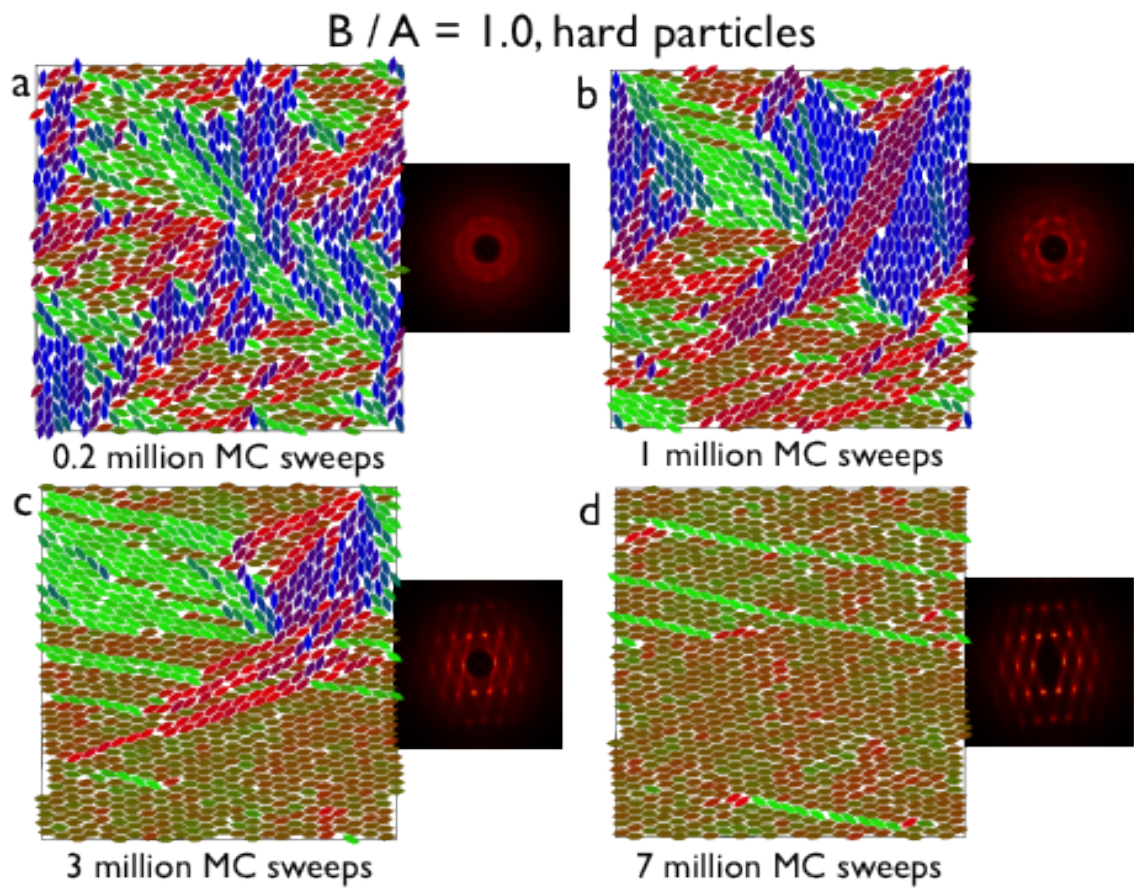


Figure 3.6: Assembly of equilateral elongated rhombs with $B/A = 1.0$. These irregular particles can assemble equally well into a parallel space-filling tiling or an alternating space-filling tiling. Without interactions, the particles entropically prefer the parallel arrangement. The simulation is run at constant pressure.

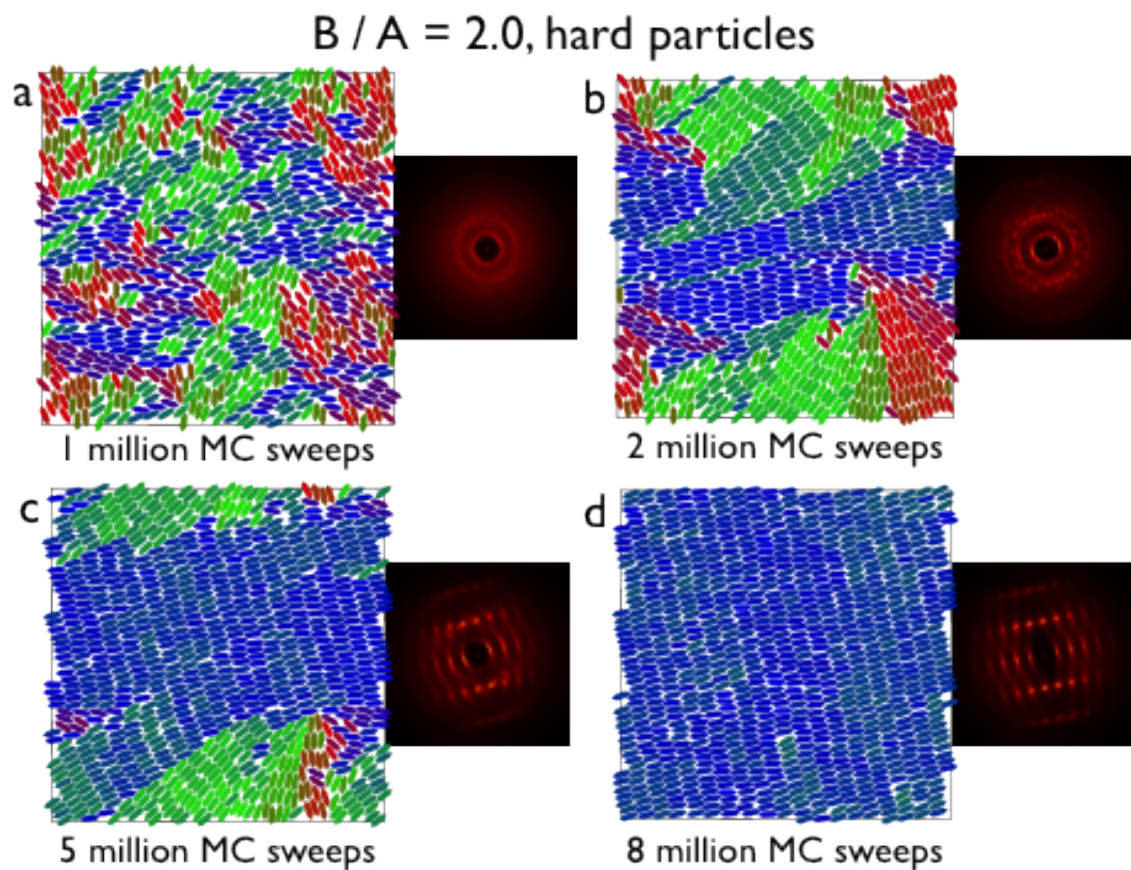


Figure 3.7: (a-d) Strongly elongated hexagons align quickly and assemble into the parallel pattern. Stacking faults have relatively low angles and single domains can be obtained robustly in simulation.

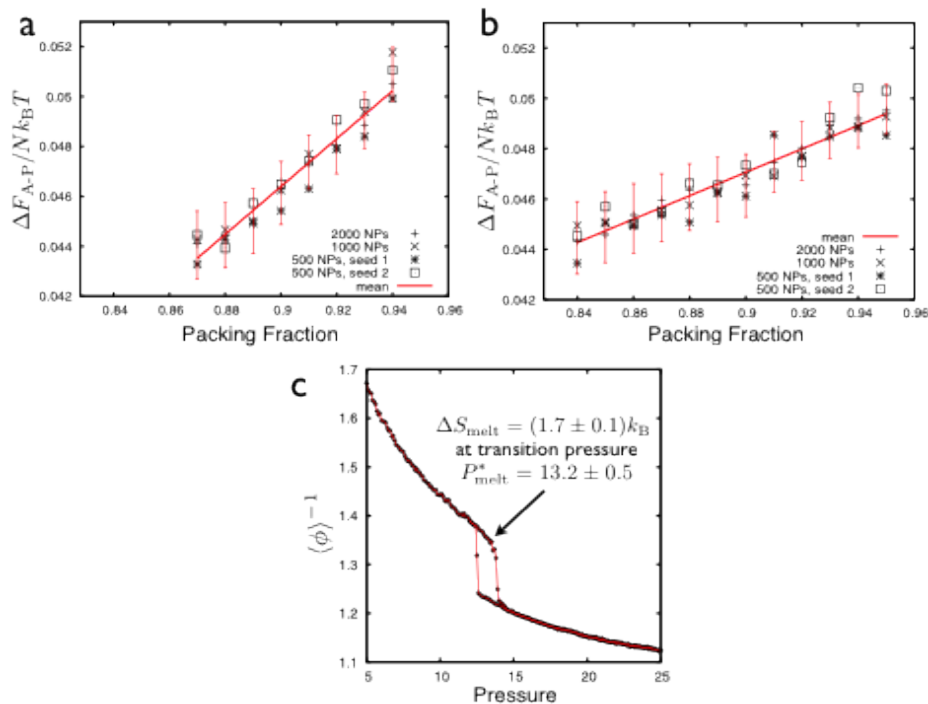


Figure 3.8: Free energy difference $\Delta F_{AP} = F_{Alt} - F_{Para}$ between the alternating and the parallel pattern for hard (a) rhombi with $B/A=0$ and (b) equilateral elongated hexagons with $B/A = 1.0$. Both plots show a positive free energy difference, which demonstrates that the parallel arrangement is more stable than the alternating pattern. The free energy difference is in the range 0.045 ± 0.015 over the stability regime of the crystal and increases linearly with packing fraction. Different size initial configurations were chosen to test for finite size effects. The free energy calculation employs the Frenkel-Ladd method. (c) Melting and crystallization curves sketching out the hysteresis around the fluid-solid transition for hard irregular hexagon with $B/A = 1$. From the jump in the inverse packing density $\Delta\phi^{-1}$ and the transition pressure P_{melt}^* we estimate the jump in entropy between fluid and solid, $S_{melt}/k_B = P_{melt}^* - 1$, to be 1.7 ± 0.1 .

melting for the equilateral elongated hexagon. Hence, entropy alone always favors parallel alignment and never stabilizes an alternating pattern.

3.3.3 Density functional theory calculations

To explain the appearance of the alternating arrangement for equilateral elongated hexagons, interparticle interactions are explicitly taken into account. We perform density functional theory (DFT) calculations to assess the relative strength of van der Waals interactions between nanoplate edges induced by a difference in the coverage density of oleic acid ligands/tethers. Van der Waals interaction between the nanoplate inorganic cores can be neglected in the edge-to-edge configuration. Of particular interest is the atomistic origin of possible interaction anisotropies between the crystallographically distinct nanoplate edges, which we will later identify as the reason for the formation of the alternating pattern. We obtained the most stable atomic structures of DyF_3 (001) and (101) surfaces (edges) by DFT calculations as shown in Figs 4a and 4c. We also calculate the surface dipoles of pristine edges and edges with adsorbed formate (HCOO). In both cases the dipoles on these two edges have similar values. This demonstrates that dipolar interactions cannot be responsible for edge interaction anisotropy. Furthermore, zeta-potential measurements indicate that the LnF_3 nanoplates are nearly neutral, and therefore the contribution of electrostatic forces to the interparticle interactions is negligible. On the other hand, the surface atomic structures in Figs 9a and 9c show that Dy atoms on the (101) edge have fewer nearest neighbor F atoms than those on the (001) edge, suggesting that Dy atoms on the (101) edge should have stronger adsorption ability than those on the (001) edge. Indeed, DFT calculations show that only one oxygen atom of each oleic acid molecule is coordinated to a Dy atom on the (001) edge as opposed to two on the (101) edge (Figs. 3.9c and 3.1d). As a result, the adsorption energy of oleic acid molecules on the

(001) edge is 0.1 eV compared to 0.7 eV on the (101) edge, which suggests a significant difference in the surface coverage density of oleic acid ligands between these two edges. While DFT calculations were performed in vacua, the calculated adsorption energy difference should be robust regardless of the presence of solvents. In light of the large difference in adsorption energies, we believe that secondary solvent effects such as an induced conformation change of alkyl chains of ligands⁵⁶ will not change significantly the relative effective interaction between different types of nanoplate edges.

3.3.4 Interaction asymmetry between nanoplate edges

We introduce an empirical model for the interaction between neighboring particles for use in Monte Carlo simulations. Since the particles do not possess significant charges or dipole moments, they interact only locally with an attractive van der Waals interaction induced by their oleic acid tethers (Fig. 3.11j). We further assume that the interaction energy is linearly proportional to the contact area of the tethers, which means it is proportional to the edge-to-edge contact length in the 2D model. In our interaction model the potential energy is minimal for parallel arrangement with neighbor distance equal to twice the tether length. It remains to choose an attraction strength ξ_{A-A} , ξ_{B-B} , and ξ_{A-B} for each pair of edge types. For the equilateral elongated hexagon, by adding up all the neighbor contributions to the potential energy, we achieve a total energy difference $E_{alt} - E_{para} \propto 4\xi_{A-B} - 2\xi_{A-A} - 2\xi_{B-B}$. The alternating arrangement will be preferred, if the contact of unlike edges is energetically advantageous, on average, compared to the contact of like edges, i.e. if the interaction asymmetry $\epsilon = 2\xi_{A-B}/(\xi_{A-A} + \xi_{B-B}) - 1 > 0$. Indeed, this is confirmed in simulation in Fig. 3.11b.

A slight preference for contact of unlike edges ($\epsilon = 0.2$) results in alternating patterns (Figs 3.11 c-e Supplementary Figs 3.12 and 3.13). The introduction of interac-

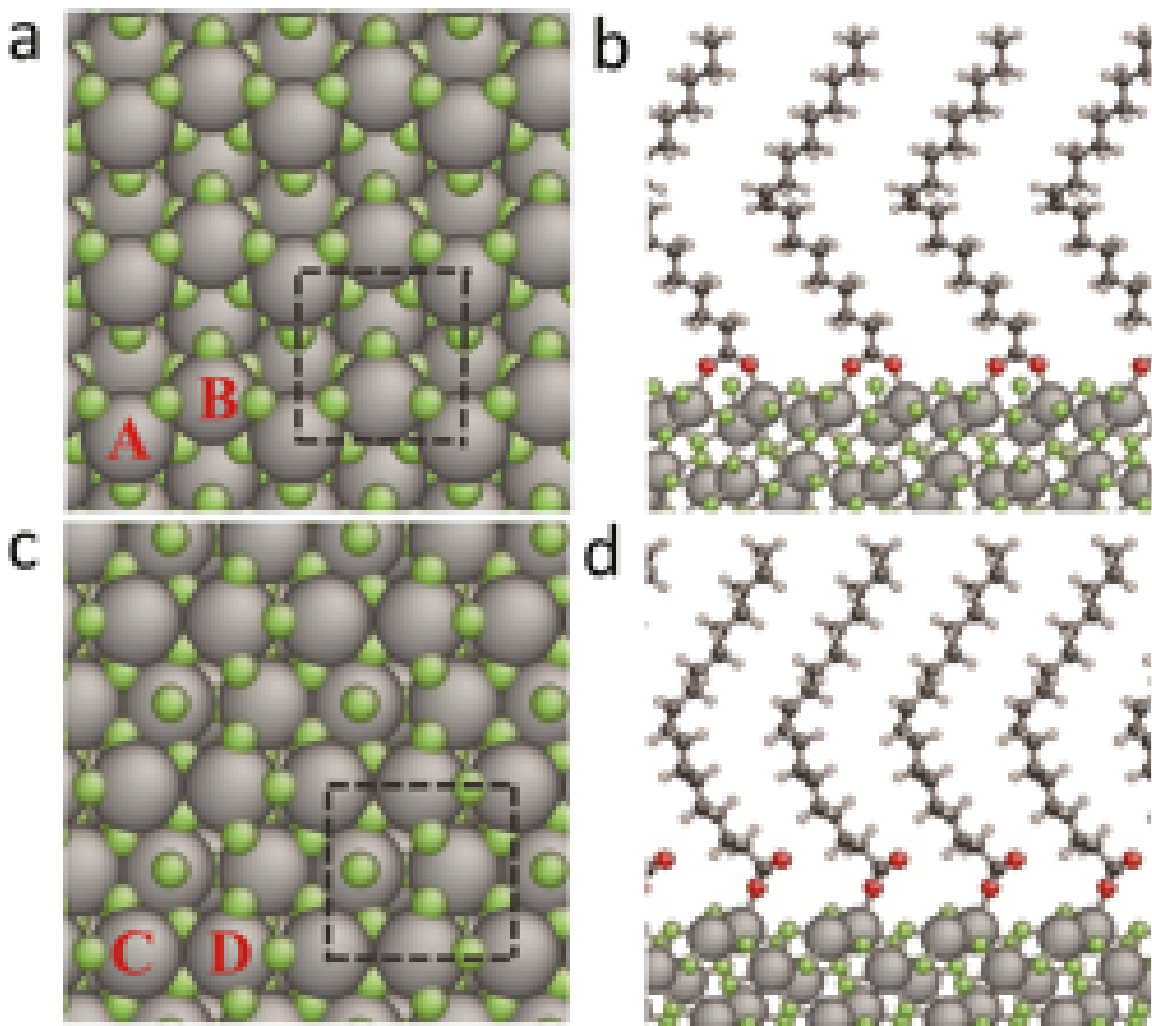


Figure 3.9: Atomic structure of DyF_3 surfaces. Density functional theory calculations reveal the structure of a-b the (001) surface and c-d the (101) surface. The figure shows pristine surfaces in top view (a,c) and surfaces with adsorbed oleic acid viewed from the side (b,d). The depicted atoms are Dy (grey), F (green), C (black), O (red), and H (white). The dashed squares in (a,c) are primitive unit cells on the surfaces. Letters A, B, C and D indicate different types of surface Dy atoms that have less nearest neighbor F atoms than bulk Dy atoms. For each bulk Dy atom, there are 9 nearest neighbor F atoms. On the (001) surface, this number is 7 for A and 8 for B, and on the (101) surface both C and D have 7 nearest F atoms.

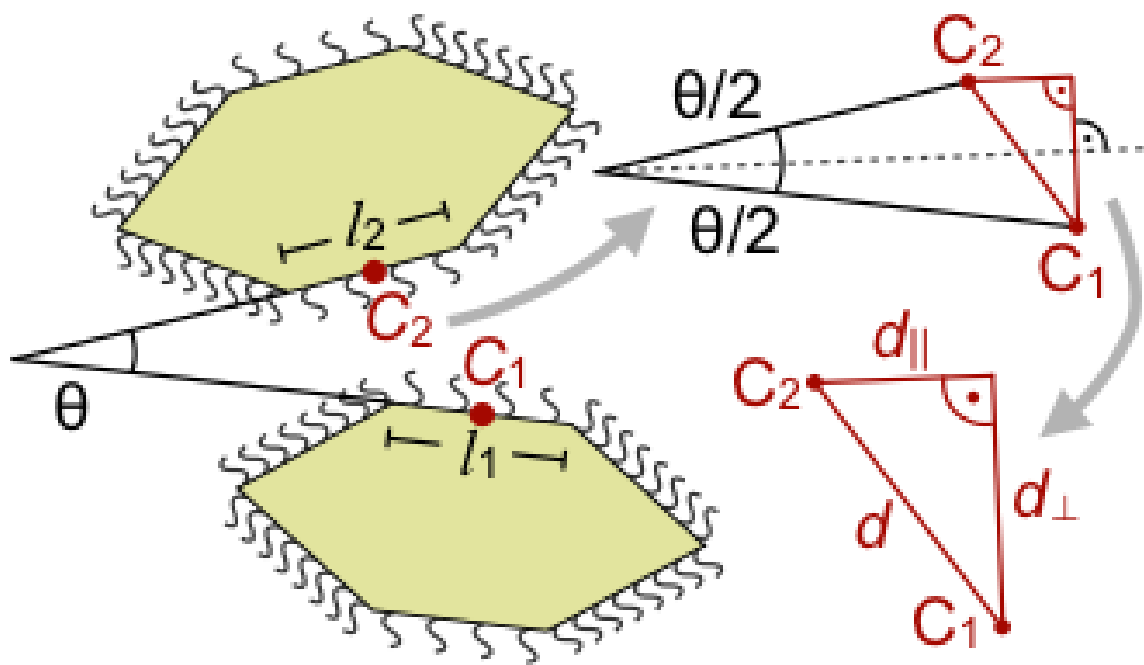


Figure 3.10: Modeling interacting rare earth fluoride nanoplatelets. Oleic acid tethers cause an effective interaction of nanoplatelet edges. The interaction strength depends on the orientation angle θ , the shift d_{\parallel} parallel to the bisector of the two edges, and the normal distance d_{\perp} perpendicular to the bisector.

tions to the rhomb system leads to a polycrystal, closely resembling the experimental results (Fig. 3.14). For B/A either sufficiently greater or smaller than one, entropy dominates and the parallel arrangement prevails again. Fast compression of large systems results in polycrystalline assemblies with excellent agreement between simulations and experimental findings (Figs. 3.11f-l).

In close-packed nanocrystal superlattices, the interparticle distances can be regarded as an indication of the strength of van der Waals attractions arising from partially interdigitated ligands connecting opposing edges. In the parallel arrangement of self-assembled superlattices of irregular hexagonal nanoplates, the B-B distance is consistently larger than the A-A distance regardless of the nanoplate aspect ratio (Figure 3.15).

Since configurations where the A-A distance is larger than the B-B distance and the reverse have very similar packing densities, they are entropically degenerate. Therefore, the experimentally observed nonuniformity in interparticle distances implies an asymmetry in the attractions between A-A and B-B edges. Finally, from DFT calculations we know that the B edges are much less covered by the oleic acid tethers compared to the A edges, which suggests $\xi_{A-A} > \xi_{B-B}$. On the other hand, A-B and A-A distances are very similar for nanoplates in the alternating arrangement (and is also close to the A-A distance in superlattices of rhombic nanoplates), suggesting $\xi_{A-B} \approx \xi_{A-A}$. The result is an interaction asymmetry $\epsilon > 0$.

3.3.5 Conclusions

In conclusion, we have reported the synthesis of a family of highly faceted planar nanotiles with rich and subtle self-assembly behavior. The aspect ratio of the nanoplates is broadly tunable by exploiting the trend of LnF_3 nanocrystal formation

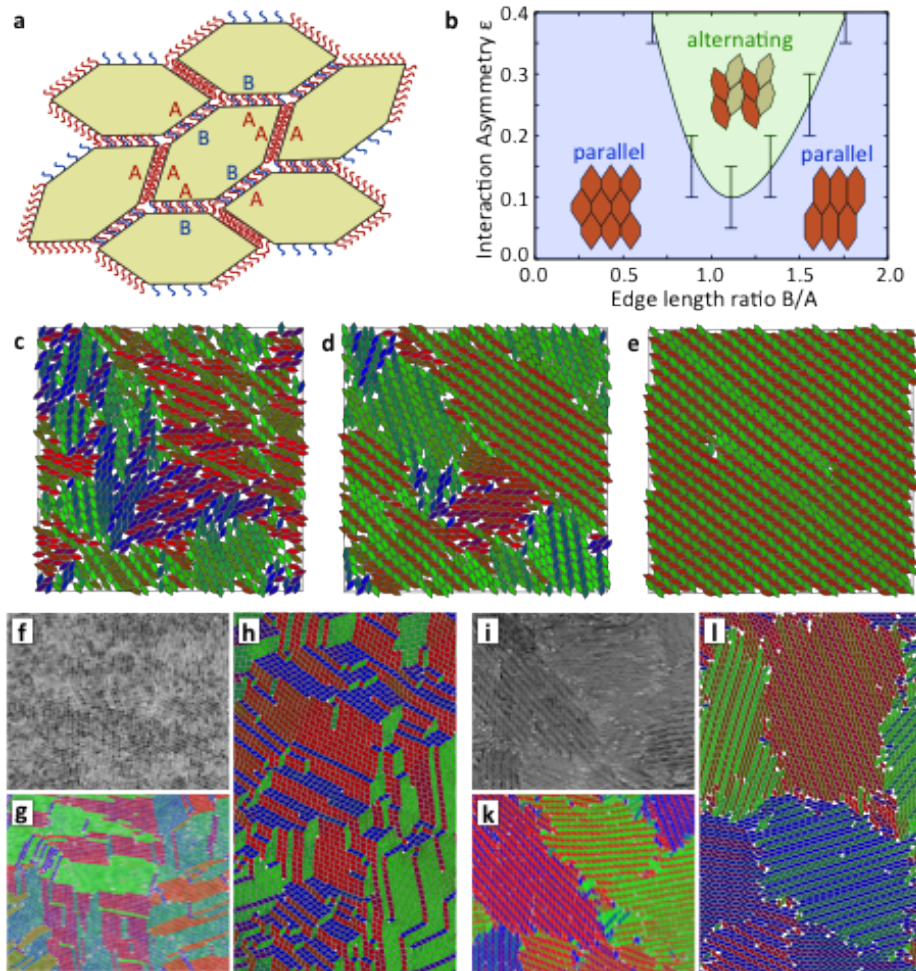


Figure 3.11: Modeling and simulation of interacting lanthanide fluoride nanoplates. (a) Oleic acid tethers cause an effective attraction of nanoplate edges that is asymmetric with respect to the two edge types A and B. b, The phase diagram as a function of edge length ratio obtained from Monte Carlo simulations shows the stability regions of the parallel arrangement and the alternating arrangement. An interaction asymmetry greater than zero is required to stabilize the alternating arrangement. Error bars span from the lowest ϵ that exclusively forms the alternating arrangement to the highest ϵ that exclusively forms the parallel arrangement. (c-e), Simulation results for the interaction asymmetry $\epsilon = 0.2$ demonstrate the formation of the alternating arrangement (from left to right: early, middle, and late stage assembly). (f-l), Electron microscopy snapshots in original contrast (f,i) and colored using image processing (g,k) are compared to simulation results (h,l). A close similarity of the local order is apparent for $B/A = 0$ (f-h) and $B/A = 1$ (i-l).

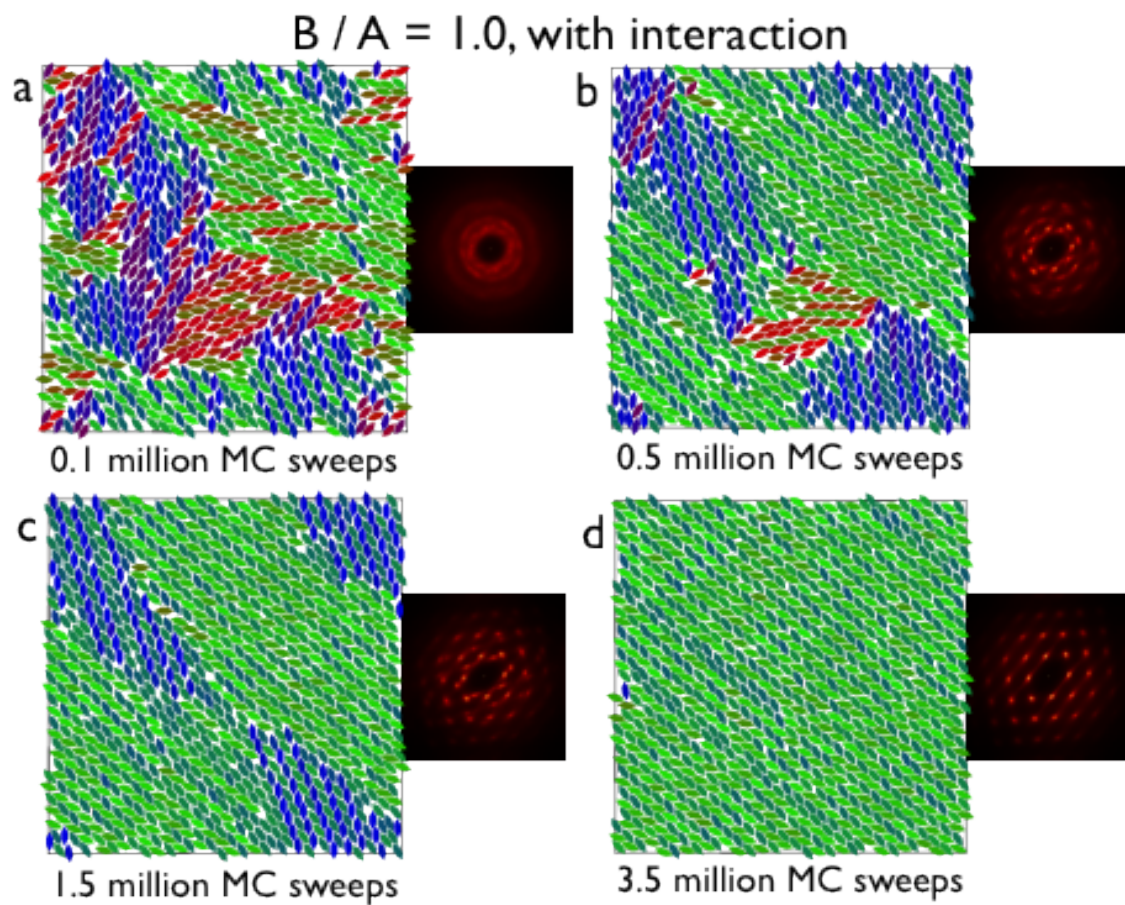


Figure 3.12: Equilateral elongated rhombs with an interaction that prefers the alternating tiling. (a-b) The attraction between edges of different type (A-B) is stronger than the attraction between edges of the same type (A-A and B-B) as observed in the experimental systems of LnF_3 nanoplates. Interaction speeds up the assembly compared to the hard systems. Between (c) and (d) the biggest crystalline grain takes over the whole simulation box. Note that in (d) one stacking fault still remains. This stacking fault cannot heal because of the periodic boundary conditions.

$B / A = 1.0$, with interaction

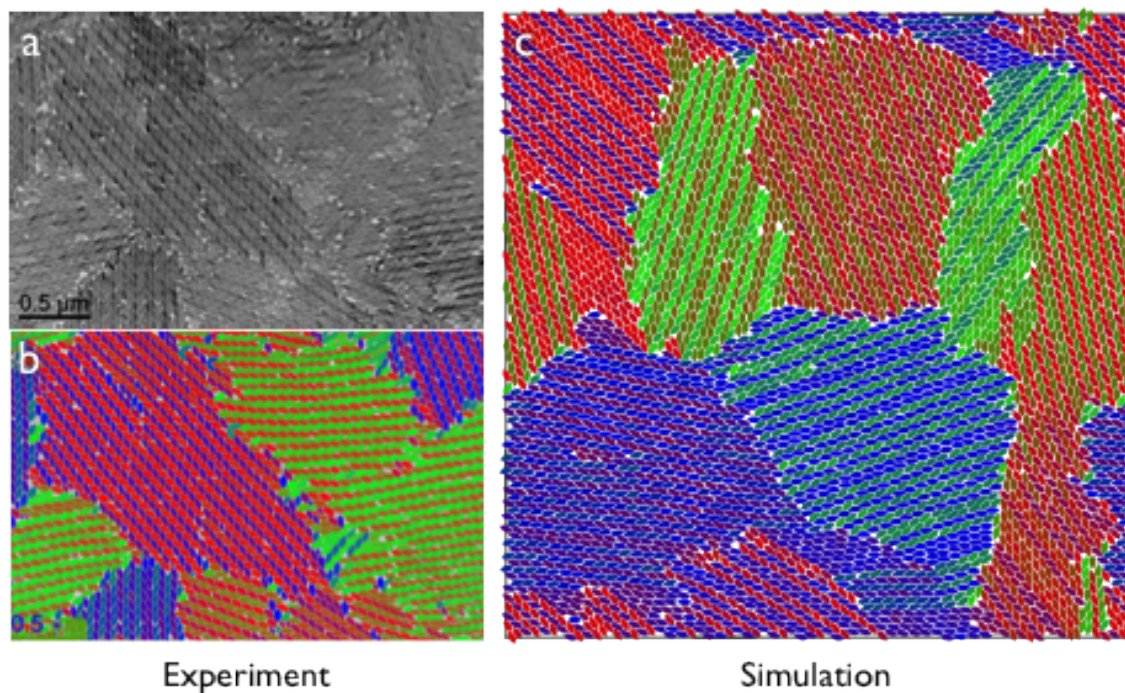


Figure 3.13: (a) TEM image of a multicrystalline state of TbF_3 plates. (b) Coloring the plates based on their orientation using image analysis tools helps identifying coexisting grains. The plates assemble robustly into the alternating tiling. Note that impurities are abundant on the grain boundaries. (c) In the simulation of a large system (5000 particles), the formation of multiple grains with alternating patterns was also observed. This figure is a larger version of the subfigures 3.10 i,k,l.

$B / A = 0.0$, with interaction

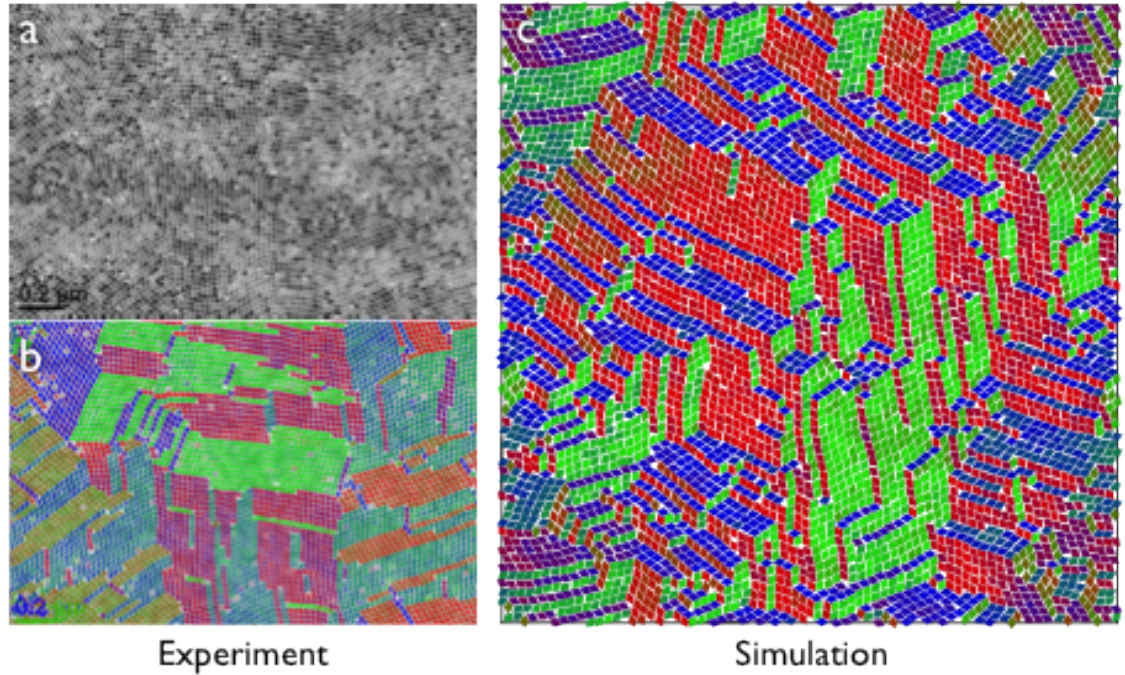


Figure 3.14: Comparison of experiment (a,b) and simulation in a larger system of interacting rhombs (c). (a) The TEM image shows the existence of multiple grains. (b) The experimental image is colored with an image analysis code. The orientation of rhombs is detected automatically by determining the inertia tensor. A clear tendency for forming parallel arrangements can be observed. (c) A large (5000 rhombs) simulation with interacting rhombs. The interaction makes it harder for the rhombs to crystallize. This figure is a larger version of the subfigures 3.11f,g,h.

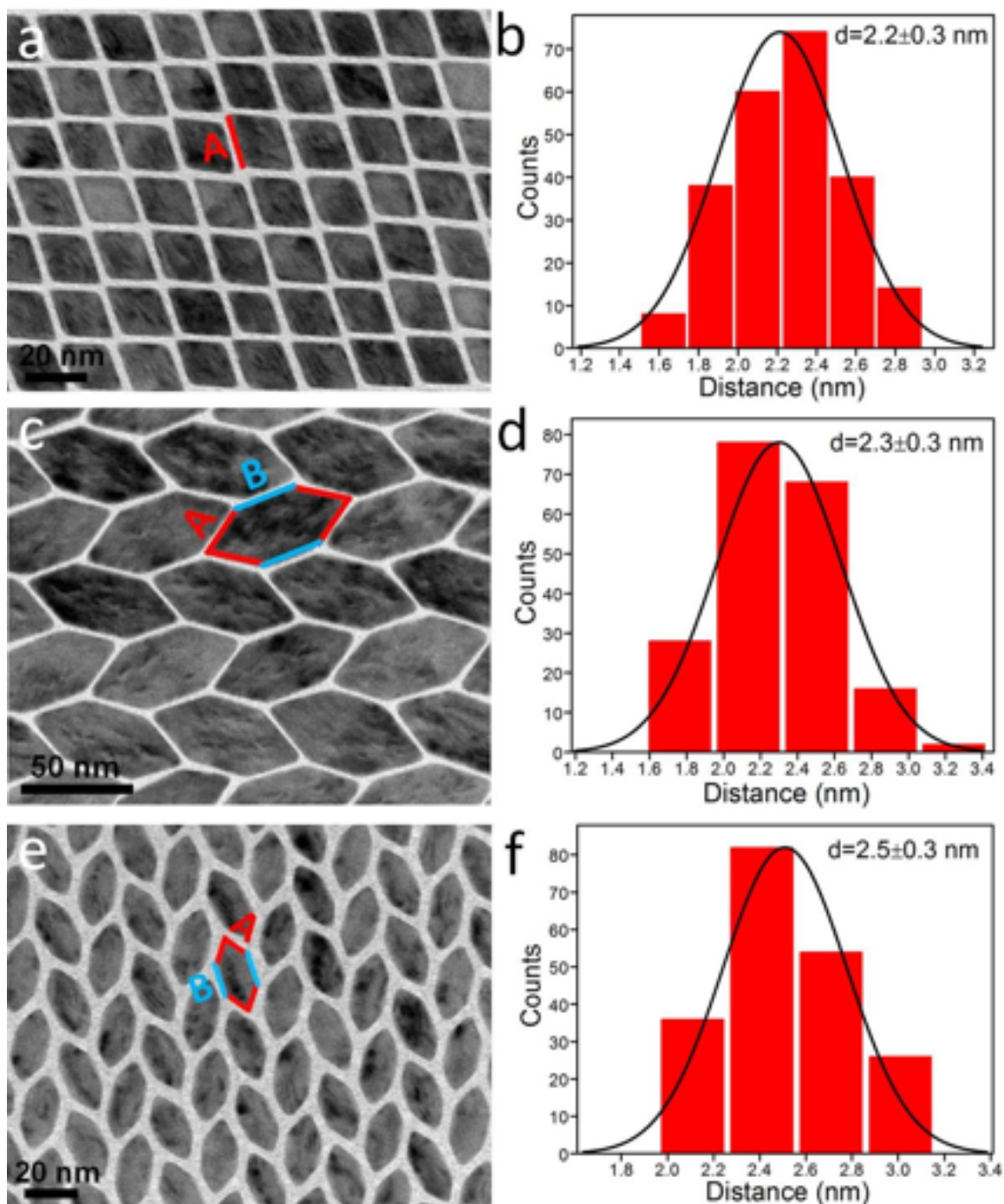


Figure 3.15: Representative TEM images of (a) DyF_3 rhombohedral nanoplate, (c) TbF_3 nanoplate and (e) DyF_3 nanoplate superlattices and the corresponding (b, d and f, respectively) statistical analysis of interparticle distance. A denotes ($\{101\}$ facets and B denotes ($\{001\}$ facets. For each histogram, at least two hundred measurements are carried out. It is noteworthy that in both alternating configuration (c and e), each nanoplate is surrounded by nearly uniform interparticle separations (2 A-A contacts and 4 A-B contacts.)

as a function of the type of lanthanide ions. Our results demonstrate that a combination of particle shape and directional attractions resulting from the patchy coverage of ligands around the nanoplate edges is responsible for the self-assembly of nanocrystal superlattices different in structure from those resulting from entropic forces alone. Controlled synthesis of shaped and faceted nanoplates not only enables the study of interplay between energy and entropy during self-assembly, but also provides further opportunity to amplify the interaction asymmetry through edge- and facet-selective chemical modification.

CHAPTER IV

Effect of shape transformations on the self-assembly of faceted patchy nanoplates with irregular shape into tiling patterns

The results of this chapter were published in:

J. A. Millan, D. Ortiz, S. C. Glotzer, Effect of Shape on the Self-Assembly of Faceted Patchy Nanoplates with Irregular Shape into Tiling Patterns, Soft Matter, January 2015

4.1 Abstract

Recent reports of the synthesis and assembly of faceted nanoplates with a wide range of shapes and composition motivates the possibility of a new class of two-dimensional materials with specific patterns targeted for a host of exciting properties. Yet, studies of how nanoplate shape controls their assembly knowledge necessary for their inverse design from target structures has been performed for only a handful of systems. By constructing a general framework in which many known faceted nanoplates may be described in terms of four orthogonal anisotropy dimensions, we

discover design rules to guide future synthesis and assembly. We study *via* Monte Carlo simulations attractive polygons whose shape is altered systematically under the following four transformations: faceting, pinching, elongation and truncation. We report that (i) faceting leads to regular porous structures; (ii) pinching stabilizes complex structures such as dodecagonal quasicrystals; (iii) elongation leads to asymmetric phase behavior, where low and high aspect ratio nanoplates self-assemble completely different structures; and (iv) low and high degrees of truncation transform a complex self-assembler into a disk-like assembler, providing design ideas that could lead to switchable structures. Our numerical results provide important insight into how the shape and attractive interactions of a nanoplate can be exploited or designed to target specific classes of structures, including space-filling, porous, and complex tilings.

4.2 Introduction

Particle shape can influence profoundly the catalytic⁵⁷, plasmonic^{58,59}, photonic⁶⁰ and mechanical⁶¹ properties of complex crystal structures¹⁵. In particular, nanoplates^{6,62,63} - nanocrystal with lateral dimensions that are approximately an order of magnitude larger than one specific orthogonal dimension or thickness - have excellent catalytic⁶⁴, optical⁶⁵, and antibacterial⁶⁶ properties. Two-dimensional assemblies of perovskites, such as PbTiO_3 ⁶⁶, have interesting ferroelectric and storage properties⁶⁷. Truncation can alter the plasmon resonance of silver nanomaterials by red-shifting the extinction spectra⁵⁹. Truncated nanoplates of single crystal berzelianite can alter the near-infrared band optical absorption properties of this nonstoichiometric semiconductor⁶⁷. By controlling the shapes of nanoplates, targeted and tunable properties should be possible.

For a range of materials, nanoplate shape emerges during the growth process; in others, shapes below several microns (i.e. within the Brownian limit) may be molded, printed, or otherwise obtained. One may envision that nanoplates may attain different shapes through either passive or active means. By passive we refer to transformations made from one system to another during synthesis, as in the case of parallel studies of two related shapes, but not in the context of a single experiment or during the assembly process^{68–70}. By active we refer to in situ morphing, or shape-shifting, of nanoplates among multiple shapes^{71–74}. In this work we focused on the passive case, where one considers which of many possible synthesizable shapes to make in order to obtain a desired target structure. In both scenarios, a fundamental understanding of the relationship between nanoplate shape, the thermodynamically preferred state of a system of nanoplates, and the kinetic accessibility of those states, is desired.

We consider four shape-related anisotropy dimensions¹⁰ along which systematic shape transformations are possible for faceted, convex nanoplates: faceting, pinching, elongation (aspect ratio) and truncation. All four are shown applied to polygons (See Fig. 4.1). Faceting, elongation, and truncation (of vertices) are self-explanatory. Pinching is a symmetry-breaking transformation that converts a regular polygon into an irregular one (see Figure 4.2a). All four shape transformations alter the directional entropic⁷⁵ and enthalpic⁷⁶ forces between nanoplates by altering one or more edge lengths. Figure 4.1 shows example experimental manifestations of these four transformations taken from the literature. Gold provides an example of the faceting transformation because it can form triangular, square, pentagonal, hexagonal, nonagonal, and dodecagonal nanoplates and microplates^{77,78}. The pinch transformation is observed in silver nanorods that grow into triangular nanoflags². Uranium oxide hydroxide and gold both can form hexagonal and elongated hexagonal nanoplates, demonstrating a passive elongation transformation^{3,4,76,79}. Gold and silver nanoplates provide examples of truncation; gold forms triangular, truncated triangular, and hexagonal

nanoplates⁸⁰, and silver nanoplates can actively transform between triangular and hexagonal nanoplates *via* truncation under UV irradiation⁸¹.

Shape transformations in nanocrystal formed from different materials can lead to the introduction or suppression of different types of interaction forces comparable to thermal energies and thus crucial during self-assembly. For example, for a specific amount truncation, CdTe truncated tetrahedra exhibit a permanent dipole that act as one of the driving forces behind the formation of free-floating nanosheets¹⁹. Highly elongated CdSe nanorods also show electrostatic dipoles that scales linearly with the volume of the nanorod⁸². Near field forces can also be introduced with external electric fields and can either red-shift or blue-shift the surface plasmon resonance of two-dimensional silver⁸³ or gold⁸⁴ nanoparticle arrangements with varying interparticle distance. However, for a systematic and extensive study on the effect of shape, we assume that shape-induced entropic and ligand-induced attractive forces mainly govern the self-organization process of nanoplates.

Here we investigate the pinch, elongation, and truncation shape transformations applied to the complete family of regular n -sided polygons (n -gons) (i.e. the faceting dimension) to understand the role of shape on nanoplate assembly. First, we establish that with the exception of the regular pentagon, heptagon and octagon the regular n -gons self-assemble into Archimedean tilings. We then systematically transform each regular n -gon using the pinch, elongation or truncation transformations. The effect of each transformation on self-assembly is categorized to identify commonalities and trends. This library of shape transformations serves to guide the development of a design framework to improve the assembly properties of a faceted nanoplate.

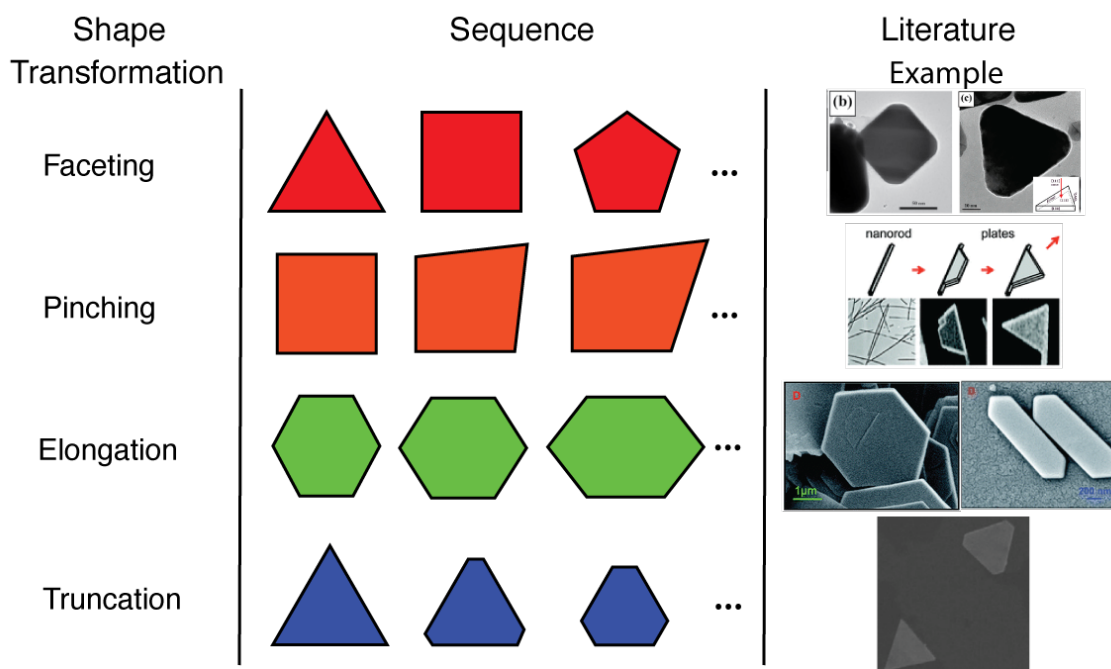


Figure 4.1: Shape transformations for nanoplates. The first column corresponds to the classification of experimentally observed shape transformations corresponding to faceting, pinching, elongation, and truncation. The second column depicts the effect of each transformation on particle shape. Experimental examples of each transformation are shown in the third column. The faceting shape transformation is shown for silver nanoplates⁸⁵. The pinch transformation is shown for the growth of a silver triangular nanoplate on a nanorod². The elongation transformation is shown for uranium oxide hydroxide hexagonal nanoplates³. The truncation transformation is shown for hexagonal and triangular nanoplates⁴.

4.3 Model and method

Each nanoplate is modeled as a mathematically hard polygon with short-ranged attractive patches on each edge. In the vicinity of two nanoplates, a pair of edges each with characteristic lengths l_1 and l_2 ($l_1 \geq l_2$) interacts *via* a pair potential that depends on three independent parameters: relative orientation angle θ , parallel shift d_{\parallel} , and normal distance d_{\perp} . In that case, the potential energy can then be written as a product of independent terms so that $V(\theta, d_{\parallel}, d_{\perp}) = \epsilon V(\theta)V(d_{\parallel})V(d_{\perp})$ with attraction strength $\epsilon > 0$, where,

$$V(\theta) = 1 - \left(\frac{1 - \cos(\theta)}{1 - \cos(\theta_0)} \right), \quad (4.1a)$$

$$f(d_2) = \begin{cases} l_2, & \text{if } d_{\parallel} \leq (l_1 - l_2)/2 \\ (l_1 + l_2/2 - d_{\parallel}), & \text{if } d_{\parallel} > (l_1 - l_2)/2 \end{cases} \quad (4.1b)$$

$$V(d_{\perp}) = 1 - (1 + d_{\perp}/d_0)^2, \quad (4.1c)$$

for $\cos(\theta) < \cos(\theta_0) = 0.95$, $d_{\parallel} < (l_1 + l_2)/2$, $d_{\perp} < 2d_0 = 0.4l_1$ and 0 otherwise. The attractive strength is set n -gon $\epsilon = 1k_B T$ for each patch. The geometric constrain $\cos(\theta) \geq \cos(\theta_0) = 0.95$ enforces the interaction between a misoriented pair of edges to vanish in the limit of multiple edges allowing for a finite convergence in the energy calculations per particle. The edge-edge interaction potential can be decomposed into three components: parallel, perpendicular, and angular (Fig. 4.2). Each component of the interaction potential models, in a minimal way, different aspects of the ligand-induced van der Waals, solvophobic or other attractive interactions (e.g. DNA linkers) that may be present between nanoparticles⁸¹. The perpendicular component ($V(d_{\perp})$) is chosen to be strongest at twice the length of ligand stabilizers,

while the parallel ($V(d_{\perp})$) and angular ($V(\theta)$) components model the contact area and steric repulsion between ligands. Assuming ligand-ligand attractive forces dominate over other type of forces (electrostatic or magnetic forces), we scale the angular and distance cutoff based on the length of the ligands. The angular and perpendicular components scale quadratically with separation distance and relative misalignment between adjacent edges, and the parallel component scales linearly with the amount of edge-to-edge contact (Fig.4.2). The overall attraction is maximized when the edges are aligned, centered, and almost in contact. The simplified model we used does not include thermodynamic effects such as ligand reorganization (e.g. bundling or ligand crystallization) or explicit solvent effects during the self-assembly process. Instead, it provides a zeroth ideal modeling of nanoplate-nanoplate interactions based on net attraction and particle shape.

4.4 Shape transformation

Pinching: This transformation can be described as a continuous translation of a single vertex i of a regular polygon towards or away from the center of the particle (O). If the interception between the radial axis (line that goes through the particle center O and vertex i and a perpendicular line segment connecting the nearest vertices $i - 1$ and $i + 1$) is used as a new reference \hat{O} (See upper panel in 4.3)a), the new position of the vertex i can be defined by the vector (\vec{a}_i) :

$$\vec{a}_i = 2 * \xi * l_o * \hat{a}_0, \quad (4.2a)$$

where (\hat{a}_0) is unitary vector pointing along the radial direction and away from the center of the polygon, and ξ is the pinching parameter defined as $\xi = x/(2 * l_o)$. ξ ranges from 0 to 1. For $\xi=0$ the vertex i coincides with \hat{O} (left panel in Fig.S1a)

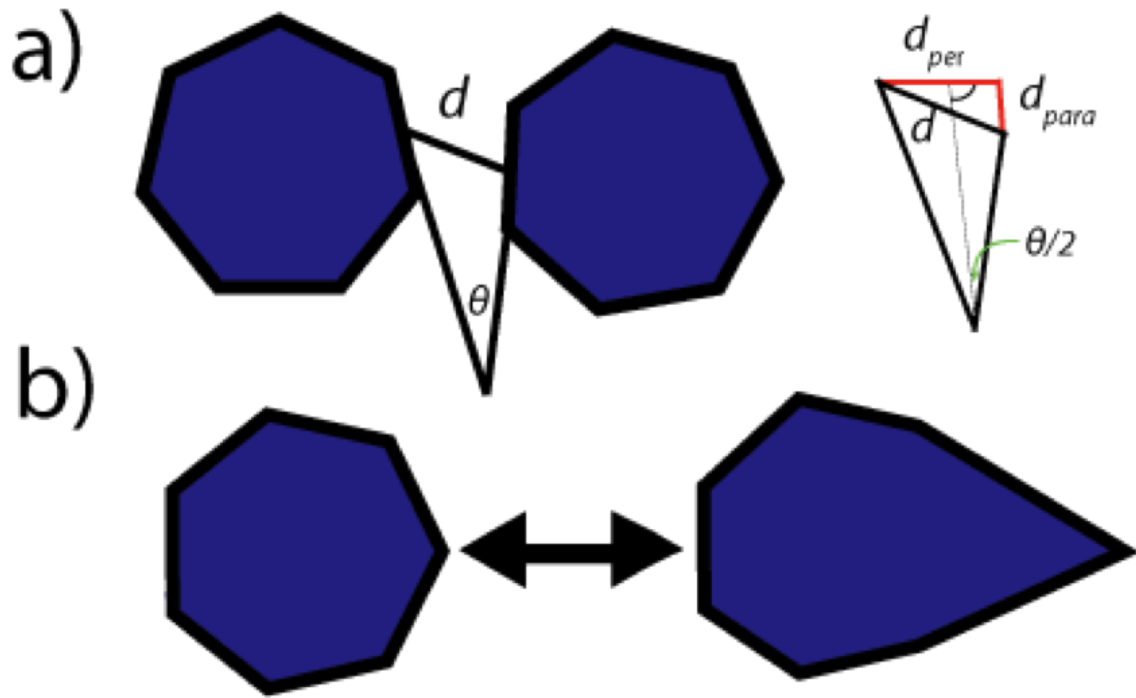


Figure 4.2: (a) The interactions between the nanoplates is edge-to-edge and scales linearly with d_{para} , quadratically with d_{per} and quadratically with orientation angle θ . (b) Pinching alters the shape of the nanoplates continuously by translating inwardly or outwardly a single vertex along the radial direction.

and for $\xi=1.0$ the polygon is strongly pinched (rightmost panel in 4.31a). Under these constraints particle convexity is always preserved and the maximum amount of displacement towards and away to the particle center by a vertex of a regular polygon is the same.

Elongation: This transformation is achieved by simultaneously and continuously rescaling the size of opposite edges by applying the following $l' = l_o$ operation: $l' = 2 * \zeta * l_o$, where l' , l_o and ζ are the final length of the two edges, the initial edge length of the regular polygon and the elongation truncation parameter ranging 0 to 1(See 4.3.b). Left, mid-, right panels in 4.31Ab show the case when $l' = 0(\zeta = 0)$, $l' = l_o$ ($\zeta=0.5$, regular polygon), and $l' = 2 * l_o$ ($\zeta = 1.0$), respectively. We only apply this transformation on polygons with even number of edges.

Truncation: This transformation is applied on all vertices of the polygon and consists in splitting a vertex of a polygon into a new pair of vertices that lay on the neighboring edges of the split vertex (in 4.3c). This transformation doubles the number of edges of polygon. If the initial position of a vertex i is considered as a coordinate reference, and (\hat{a}_1) , (\hat{a}_2) are unitary vectors pointing from vertex i to the two closest vertices $i+1$ and $i-1$ (See leftmost panel in Fig. S1c), then this splitting is accomplished by creating a new pair of vertices represented by vectors (\vec{v}_1) and (\vec{v}_2) that can be define as follows (See mid-panel 4.3c):

$$\vec{v}_1 = \gamma * l'_o * \hat{a}_1 \quad (4.3a)$$

$$\vec{v}_2 = \gamma * l'_o * \hat{a}_2 \quad (4.3b)$$

where l'_o and γ corresponds to the edge length for the special case when all edges share the same length(See right panel in 4.3.c) and the truncation parameter, respectively. l'_o can easily be derived by analyzing the special case when all edges share a similar

length ($\gamma = 1$) which leads to the following set of equations (See lower panel in 4.3.c):

$$l'_o = l_o - |\vec{v}_2| - |\vec{v}_1| \quad (4.4a)$$

and,

$$l'_o = |\vec{v}_2 - \vec{v}_1|, \quad (4.5a)$$

where from which we arrived to:

$$l'_o = \frac{l_o}{|\vec{v}_2 - \vec{v}_1| + 2}, \quad (4.6a)$$

where we have taken into account that $|\vec{v}_1| = |\vec{v}_2| = |\vec{v}'_1| = |\vec{v}'_2|$.

4.5 Results

We present the results by the four shape transformations faceting, pinching, elongation and truncation applied to each member of the n -gon, for $n = 1-12$ at intermediate densities (packing fraction values between 0.5 and 0.7). For the faceting transformation, we also studied the cases $n = 13-16$ to find the limiting n_0 at which particles start behaving like disks. To fully elucidate the phase diagram, we quantify each transformation with geometric factors that range from 0 to 1. To fully elucidate the phase diagram, we explored these ranges by applying 0.1 increments on each characteristic geometric factor. In most cases we obtain ordered crystals after proper annealing. For any particular system, changes in interaction strength (ϵ) led to the same final structure and only affected the thermodynamic properties by rescaling the assembly temperature. Each structure is identified by its crystallographic bond network drawn from the centers of the nanoplates.

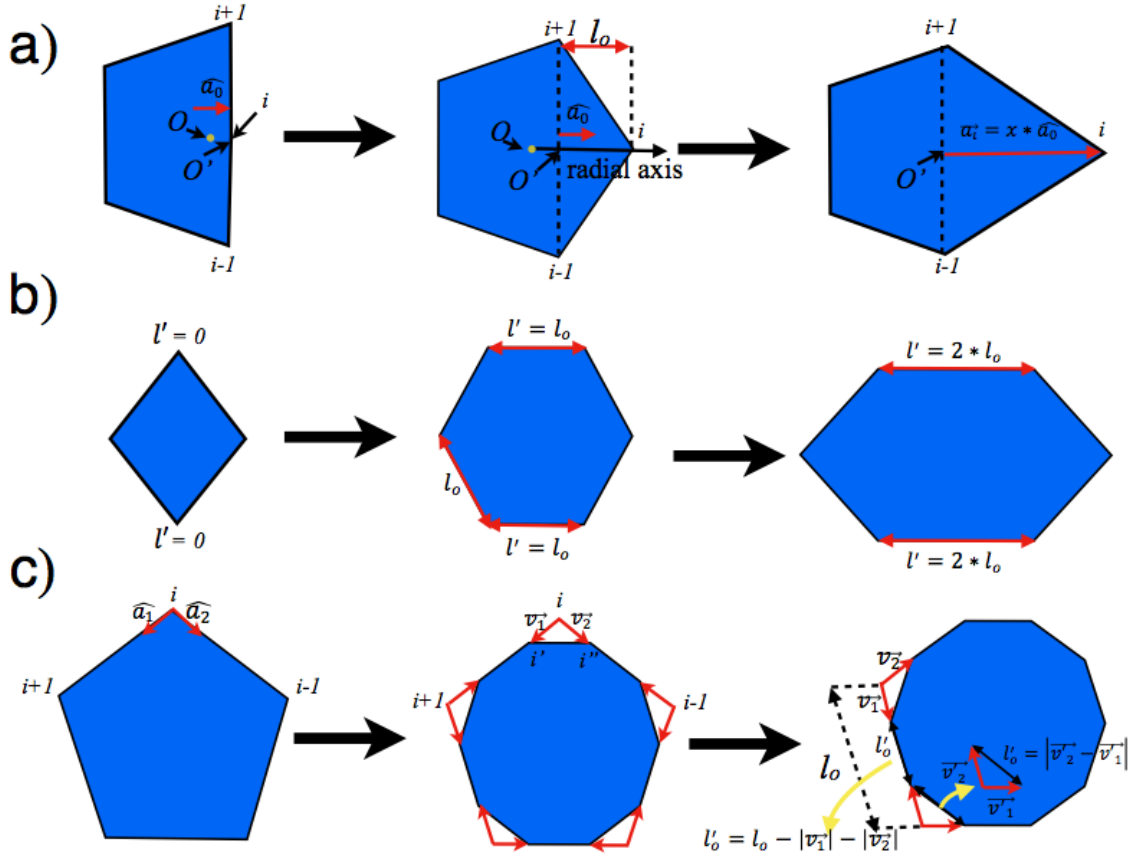


Figure 4.3: Schematics of the pinching, truncation and elongation shape transformation. (a) Pinching modifies the shape of a regular polygon continuously by translating a single vertex inwardly or outwardly along the radial direction (axis connecting vertex i and particle center O). The interception between the line segment connecting vertices $i + 1$ and $i - 1$ corresponds to a reference O' . l_0 (red double head-arrow) and (\vec{a}_0) (red vector) correspond to the distance of vertex i with respect to O' and the unitary vector pointing along the radial axis, and we defined the new position of vertex i as $(\vec{a}_i) = 2 * \xi * l_0 * (a_0)$ (after translating the vertex i), where ξ corresponds to the pinching parameter. Left, Mid- and lower panels correspond to the cases $\xi = 0, 0.5$ and 1 . (b) Elongation is achieved by rescaling the length (l') of a pair of opposite edges (red arrows) with initial length l_0 . Left, mid- and right panels correspond to the cases when ($\zeta = 0, 0.5$) and 1 . (c) Left panel shows vertex i and unitary vectors (\hat{a}_1) and (\hat{a}_2) along which vertex i splits. As shown in the mid-panel, vertex i splits into vertices i' and i'' represented by vectors (\vec{v}_1) and (\vec{v}_2) , and the same operation is applied to each vertex to truncate all vertices of the polygon to obtain the new polygon (solid blue). For the special case ($\gamma = 1$, right panel), subsequent edges share the same length equal to $l'_o = l_o - |\vec{v}_2| - |\vec{v}_1| = |\vec{v}_2 - \vec{v}_1|$ (notice that $|\vec{v}_1| = |\vec{v}_2| = |\vec{v}'_1| = |\vec{v}'_2|$).

4.5.1 Faceting

The faceting transformation alters the number of edges of a regular polygonal nanoplate within a given n -gon family (Figure 4.4a). Overall, we find the effect of faceting on self-assembly can be divided into three cases: (i) Archimedean tilings result for $n = 3, 4, 6, 8$ and 12 . (ii) Frustrated assemblies result at intermediate n for some odd number vertices ($n = 5, 7$ and 9). (iii) Effective rounding of the nanoplates for $n > 9$ produces assemblies expected from attractive, disk-like particles.

Members of the n -gon family self-assemble into ordered structures identical to an Archimedean tiling when polygons and gaps are viewed as independent tiles. For a subset of these polygons, the densest packings are identical to the assembled tilings. It is known that polygons tend to form dense periodic packings with quasi 6-fold symmetry⁸⁶. In those tilings, the packings contact types are either edge-to-edge or a combination of both edge-to-edge and edge-to-vertex for polygons with even or odd numbers of vertices. Regular polygons with assemblies in the Archimedean tiling class include the regular triangle, square, hexagon, octagon, and dodecagon; these self-assemble the (3^6) , (4^4) , (6^3) , (4.8^2) , and (3.12^2) Archimedean tilings, respectively (Fig. 4.4b, c, e, g and k). Our previous work on the self-assembly of the Archimedean tilings shows that the (3^6) , (4^4) , (6^3) , and (3.12^2) tiling can also self-assemble without attraction between the nanoplates and due solely to entropy, whereas the (4.8^2) Archimedean tiling requires enthalpic patches⁸⁷.

The regular pentagon, heptagon, and nonagon (See Figure 4.4d, f and h) do not form ordered assemblies on the time scale of our simulations. These polygons have five-fold, seven-fold, and nine-fold rotational symmetry, respectively, rendering them inconsistent with the standard Bravais lattice coordination. Theoretical work on the five- and seven-fold coordinated nearest-neighbor defects indicate increased frustra-

tion and crystallization inhibition⁸⁸. Experimental work on the assembly of five-fold symmetric hydrocarbons has shown glass formation⁸⁹. Liquid crystals can form five-fold, seven-fold, and nine-fold quasicrystals⁹⁰. This propensity in nature for five-, seven-, and nine-fold symmetric entities to self-assemble disordered and/or quasicrystal structures argues for frustration and competition to be prevalent in the assembly of pentagons, heptagons, and nonagons, and this is indeed what we observed.

The more vertices a polygon has, the more the shape approximates that of a disk. At small $n < 9$, n -gons that do assemble into space filling structures exhibit a density-driven transition upon compression at constant temperature from the previously discussed structures (at intermediate densities) to the densest packing structures. For example, a phase transition between the (4.8^2) Archimedean tiling and the (3^6) packing occurs at high packing fraction for the regular octagon. For $n > 9$, the assemblies resemble the expected assembly for hard disks. The regular decagon assembles the (3^6) tiling at higher density but a rhombic crystal at lower density (see Figure 4.4i and m). The hendecagons, tridecagons and hexadecagons each form a sheared $(3^2.4.3.4)$ Archimedean tiling (Figure 4.4f, k and Figure 4.5b), also known as the snub square (SS) tiling or sigma phase, a periodic approximant of a 12-fold quasicrystal. Tetradecagons form center rectangular lattices and pentadecagons formed a disordered structure with no global order (Figure 4.4a,b). A transformation between the sheared $(3^2.4.3.4)$ Archimedean tiling to the (3^6) Archimedean disk tiling occurs for $n \geq 17$.

4.5.2 Pinching

The pinch transformation alters the geometry of an n -gon by moving a vertex radially from the center (Figure 4.2b). We investigate the pinch transformation while preserving the convexity of the building block. Pinching transforms a regular poly-

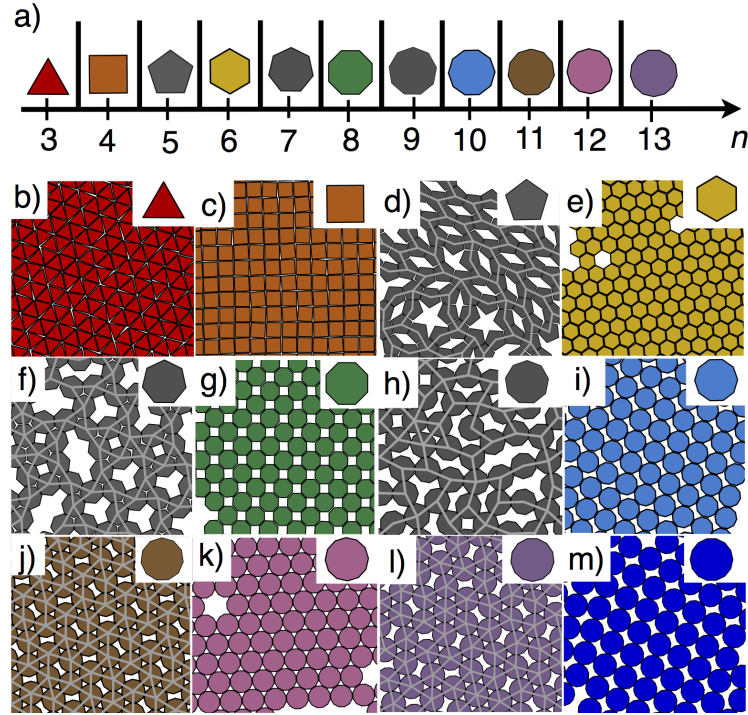


Figure 4.4: Self-assembly of n -gons. (a) The faceting transformation is summarized by a geometric axis showing the regular polygons. Grey n -gons imply a frustrated assembly, while a colored regular n -gon indicates that shape assembles into a crystal. (b-l) Each snapshot shows a portion, cut from a larger sample containing as many as 1000 nanoplates, of a representative assembly of the nanoplates. The assemblies for the regular n -gon family are (b) the (3^6) Archimedean tiling for the regular triangle, (c) the (4^4) Archimedean tiling for the regular square, (d) a frustrated assembly for the regular pentagon, (e) the (6^3) Archimedean tiling for the regular hexagon, (f) a frustrated assembly for the regular heptagon, (g) the (4.8^2) Archimedean tiling for the regular octagon, (h) a frustrated assembly for the regular nonagon, (i) a sheared rhombic tiling for the regular decagon, (j) a sheared $(3^2.3.4.3)$ Archimedean tiling for the regular undecagon, (k) the (3.12^3) Archimedean tiling for the regular dodecagon, and (l) a sheared $(3^2.3.4.3)$ Archimedean tiling for the regular tridecagon and (m) a center rectangular tiling formed for the regular tetradecagon.

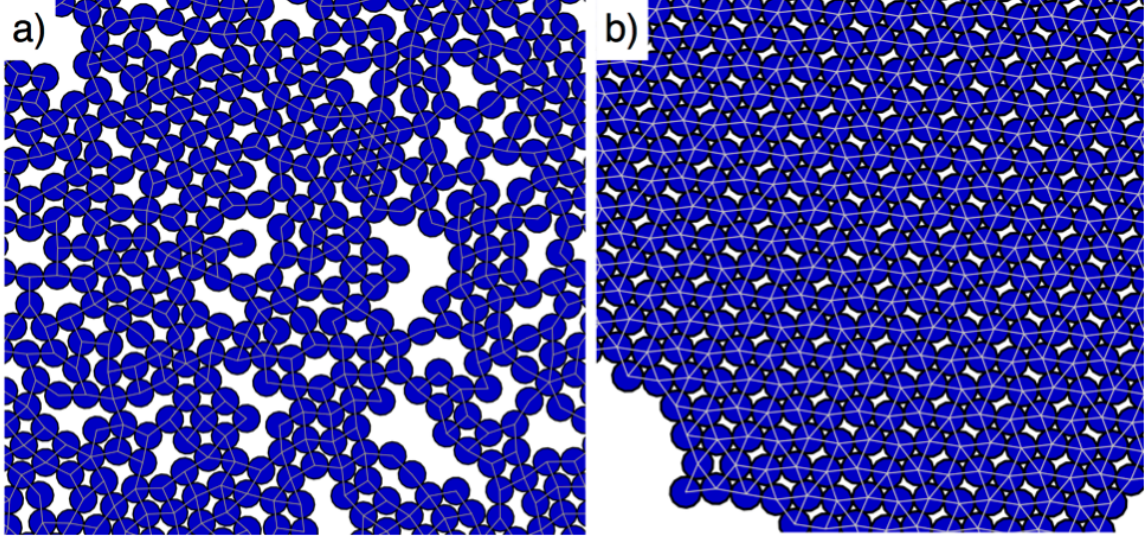


Figure 4.5: Self-assembled structures from sticky pentadecagons and hexadecagons. (a) Pentadecagons show no global order and (b) hexadecagons exhibit a sheared snub square lattice illustrated by the underlying nearest neighbor bond structure. This structure is similar to the structures self-assembled by hendecagons and tridecagons.

gon with n vertices into two limiting shapes: an irregular n -sided polygon with an extended vertex or an irregular $n-1$ sided polygon (see symbols in Figure 4.6a). This shape transformation is analogous to the transformation between a sphere and a cone. Previous work on self-assembly of sticky cones has shown that a precise sequence of convex clusters form at magic numbers determined by the cone shape^{91,92}. To quantify the transformation, we introduce a deformation parameter ξ . This parameter provides a means of geometrically connecting the two limiting cases, which can exhibit very different phase behavior. Figure 4.6a shows the faceting vs. pinching phase behavior of transformed polygons. At $\xi = 0.5$, the regular n -gons are shown and colored based on the crystal structures observed in Fig 4.4. If a pinched n -gon self-assembles structures that are crystallographically distinguishable from that of the regular (unpinched) n -gon, the polygonal symbol in the phase diagram is colored differently from that of the regular polygon at $\xi = 0.5$. We find that at low n , the pinch transformation can have a dramatic effect on assembly leading to degenerate

(low pinching) and aperiodic (pinched heptagons) structures. In contrast, at higher n the assembly is not affected because the convexity of the n -gon constrains the pinch transformation to a small deformation. In contrast, at higher n the assembly is not affected because the n -gon becomes concave for small inward pinching deformation and we only focused on convex shapes (See 4.3), thus the amount of pinching is negligible at high n .

The pinch transformation of the square stabilizes two kite assemblies shown in Figure 4.6b and c. A kite is a specific quadrilateral with two pairs of adjacent equal-length sides; kites are a prototile of the famous Penrose quasicrystal tiling⁹³. We find both a hierarchical and alternating kite crystal structure formed *via* self-assembly. The hierarchical kite tiling occurs at $\xi = 0.25$ and $n = 4$ (Figure 4.6b). The unit cell consists of two kites that combine to roughly form a rhombus. The rhombus tiling is similar to the (4^4) Archimedean tiling except for a shift between each row of rhombi due to the small protrusion of the pinched vertex (Figure 4.6b). Hierarchical crystals of nanoparticles have been shown to have interesting mechanical³⁶ and electronic⁹⁴ properties. Further outward pinching leads to the formation of alternating complex structures whose centers lay on an oblique lattice (Figure 4.6c).

The pinch transformation of the pentagon leads to two distinct crystal structures: the hierarchical rectangular tiling at $\xi = 0.0$ (Figure 4.6d) and a pentagonal Cairo tiling at $\xi = 0.25$ (Figure 4.6e). At lower ξ , a hierarchical rectangular crystal structure forms. Its unit cell consists of two pinched pentagons that collectively form a trapezoid; the rectangular crystal structure is similar to the (4^4) Archimedean tiling except that the tiling is stretched along the apothem of the building block. The pentagonal Cairo tiling is the dual of the $(3^2.4.3.4)$ Archimedean tiling, and is also referred to as the $((5^3)2.5^4.5^3.5^4)$ McMahan net⁹⁵. Fe atoms in $\text{Bi}_2\text{Fe}_4\text{O}_9$ compounds are arranged on a pentagonal Cairo tiling⁹⁶. Also, three- and four-arm DNA junction

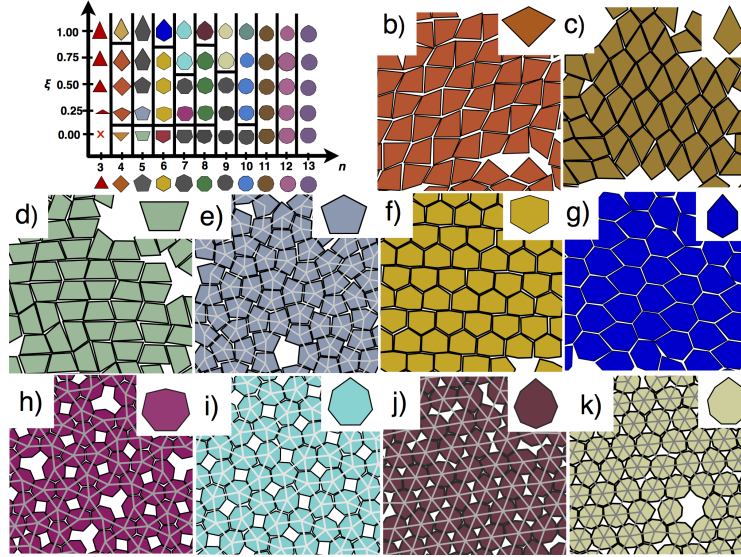


Figure 4.6: Effect of pinch transformation on the self-assembly of polygons. (a) Faceting vs. pinching phase diagram. Grey n -gons imply a frustrated assembly. The regular n -gons at $\xi = 0.5$ are shown with the symbols and crystal structures observed in Fig 2. The building blocks for each geometric phase point are shown in the geometric phase diagram. Representative snapshots of all crystal structures observed by applying the pinch transformation are shown for the regular polygons between the regular triangle and the regular hendecagon (b-k). The assemblies for the pinched n -gon family are: (b) a shortened kite assembly for $\xi = 0.25$ and $n = 4$, (c) a lengthened kite assembly for $\xi = 0.75$ and $n = 4$, (d) a trapezoidal assembly for $\xi = 0.0$ and $n = 6$, (e) a pentagonal Cairo tiling for $\xi = 0.25$ and $n = 5$, (f) a shifted prismatic tiling for $\xi = 0.25$ and $n = 6$, (g) a alternating triangular tiling for $\xi = 1.0$ and $n = 6$, (h) a dodecagonal quasicrystal for $\xi = 0.25$ and $n = 7$, (i) a $(3^2.4.3.4)$ Archimedean tiling for $\xi = 0.75$ and $n = 7$, (j) a triangular tiling for $\xi = 0.75$ and $n = 8$, (k) a triangular tiling for $\xi = 0.75$ and $n = 9$.

tiles have been shown to self-assemble the pentagonal Cairo tiling⁹⁷.

The pinch transformation applied to the hexagon results in the assembly of two different crystal structures: an alternating hexagonal tiling at $\xi = 0.0$ and, at $\xi = 0.1$, a shifted hierarchical tiling closely related to the prismatic pentagonal tiling (Figure 4.6f). The prismatic pentagonal tiling is the dual of the $(3^3.4^2)$ Archimedean tiling. Three- and four-arm DNA junction tiles self-assemble the prismatic pentagonal tiling⁹⁶. At high pinching ($\xi > 1.0$) (Figure 4.6g), the pinched hexagon forms an alternating crystal structure similar to the (6^3) Archimedean tiling⁹⁷.

The pinch transformation applied to the heptagon produces the snub square Archimedean tiling and the dodecagonal shield quasicrystal. At high ξ , the SS Archimedean tiling is stable (Figure 4.6h). At low ξ , the shield dodecagonal quasicrystal is stable (Figure 4.6i). A disordered region exists around the regular heptagon at intermediate ξ . It is interesting to note that the SS tiling, also known as the σ -phase⁹⁸, is a periodic approximant of a dodecagonal quasicrystal. Simple modifications of crystal growth rules have been shown to control the stability region of the σ -phase and the dodecagonal triangle square tiling⁹⁹. Patchy particles with seven patches symmetrically arranged on a disk has been shown to form a dodecagonal quasicrystal¹⁰⁰. It is notable that for patchy heptagons, the quasicrystal is stable for an irregular arrangement of facets on the polygonal nanoplates. The pinch transformation provides a means of transforming the disordered heptagon assembly into the snub square Archimedean tiling and a dodecagonal quasicrystal.

For large n , the pinch deformation is constrained to small changes by convexity and vertex constraints. Highly pinched octagons form only degenerate hexagonal assemblies (Figure 4.6j). Nonagons and decagons at high $\xi > 0.75$ form a triangular crystal (Figure 4.6k). For the undecagon, dodecagon, and tridecagon, pinching has no effect on assembly because the applied pinch is too small given the constraints. Tilings

comprised of nanoplates and polygonal pores (empty tiles) as shown in Figs 4.6b-k have not yet been reported in experiments. Except for the structure shown Fig. 4.6f, these tilings do not correspond to the densest packings and are the equilibrium states because NPT simulations show that at intermediate densities these porous structures are also observed, and upon further compression a transition towards the densest packings are achieved.

4.5.3 Elongation

The elongation transformation alters the shape of the n -gons by lengthening two opposite edges of regular polygons. Note that this transformation can be applied systematically only to polygons with an even number of facets. The elongation transformation is equivalent to the transformation between a sphere and a spherocylinder. The transformation is also closely related to the elongation along an axis of a sphere to form an ellipsoid. Patchy and hard spherocylinders^{34,46} and ellipsoids^{32,101} are the natural systems against which to compare the phase behavior of elongated or compressed polygons. The deformation parameter ζ quantifies the degree of elongation. Except for squares, at $\zeta=0$ two opposite edges of a regular n -gon are fully compressed until they vanish, reducing the number of edges and vertices to $n-2$. As ζ increases, these opposite edges are elongated until regular polygons ($\zeta=0.5$) are recovered, and for values of $\zeta > 0.5$ this shape transformation alters polygons into faceted rods. In Figure 4.7a, the effect of elongation on n -gons ($n=4, 6, 8, 10$ and 12) is displayed in a faceting vs. elongation phase diagram, where colored symbols showed the modified shape of the elongated particles (Figure 4.7a).

Slightly elongated squares self-assemble degenerate rectangular tilings closely related to the (4^4) Archimedean tiling. For $\zeta > 0.25$ self-assembly into structures lacking global order is observed. Elongated hexagons ($n=6$) self-assemble into three

distinct crystal structures: a random tiling for 0.0, a rhombic tiling (Fig. 4.7b), and an elongated (6^3) Archimedean tiling (Fig. 4.7c). At $\zeta = 0.0$ the polygon is a rhombus shape ($n = 4$ with angular openings of 60 degrees at the tips) and forms a random tiling in accordance with previous theoretical and experimental studies⁴⁶.

For the case of octagons ($n = 8$), low and high elongation leads to the formation of triangular and stretched (4.8^2) Archimedean tilings, respectively. At zero elongation ($\zeta = 0.0$), a triangular tiling is formed (Figure 4.7e), whereas at high elongation ($\zeta = 1.0$), the elongated octagons form a stretched (4.8^2) Archimedean tiling (Figure 4.7f).

The elongated decagon ($n = 10$) forms an alternating and a stretched rhombic crystal structure (Figure 4.7f and g). At $\zeta = 0$, the alternating crystal consists of alternating rows of oppositely oriented building blocks. The unit cell of this crystal consists of two decagons with different orientation and tiles space in a rectangular lattice (Figure 4.7g). To our knowledge, the alternating elongated decagon crystal structure has not yet been observed experimentally. At high elongation ($\zeta = 0.8$), irregular decagons assemble a stretched rhombic crystal (Figure 4.7h).

The elongated dodecagon ($n = 12$) forms a triangular tiling and a stretched Archimedean tiling (Figure 4.7i and j). At lower elongation ($\zeta = 0$), the dodecagon forms a triangular lattice that is rotationally degenerate (Figure 4.7i). At $\zeta = 1$, the elongated dodecagon forms a stretched (3.12^2) Archimedean tiling (Figure 4.7j). In a similar way to the elongated hexagon, octagon, and decagon, the elongated dodecagon effectively stretches the crystal structure formed by the regular dodecagon.

The elongation transformation is not symmetric; low and high elongation n -gons do not self-assemble the same crystal structure. In contrast, it is interesting to note that the phase diagram of hard ellipsoids is symmetric¹⁰², which implies that faceting can have an important effect on the assembly of nanorods at low aspect ratio. For

nanoplates, the elongation transformation has been previously studied for lanthanide fluoride (LaF_3) nanoplates both experimentally and with simulations⁷⁶. The experimental results in that work are similar to the tilings shown in Figs 4.7b-d. Simulation results revealed that for systems with symmetric interactions, parallel arrangements were stable regardless of the degree of elongation; entropic interactions favored such arrangements, and the introduction of symmetric forces (comparable to thermal energies) were not expected to disrupt this trend⁷⁶. Also, simulations revealed that high elongation leads to the formation of tetragonal lattices because these arrangements maximize the amount of contact between neighboring particles, thereby minimizing the total free energy⁷⁶. The porous tilings shown in Figs 4.7e-i have not yet been reported in experiments.

4.5.4 Truncation

The truncation transformation of faceted nanoplates alters the geometry of the n -gons by truncating each vertex symmetrically into an edge. The symmetric truncation transformation has no analogue in continuous geometries (disks and ellipses), and is characteristic of faceted nanoparticles. Symmetric truncation transforms a regular polygon with n vertices into another polygon with twice ($2n$) the number of vertices (see symbols in Figure 4.8a). We introduce a deformation parameter to quantify this transformation. We show the phase behavior of each nanoplate in a geometric phase diagram plotting faceting vs. truncation (Figure 4.8a). Regular n -gons are obtained at $\gamma = 0.0$ and $\gamma = 1.0$ and symbols colored according to their corresponding crystal structures are shown as in Fig 2. The truncated n -gons used to obtain the assemblies are shown in the phase diagram panel (Figure 4.8a). Truncation has an effect on self-assembly for small n , but at larger n the particles exhibit phase behavior similar to that of a disk at high density.

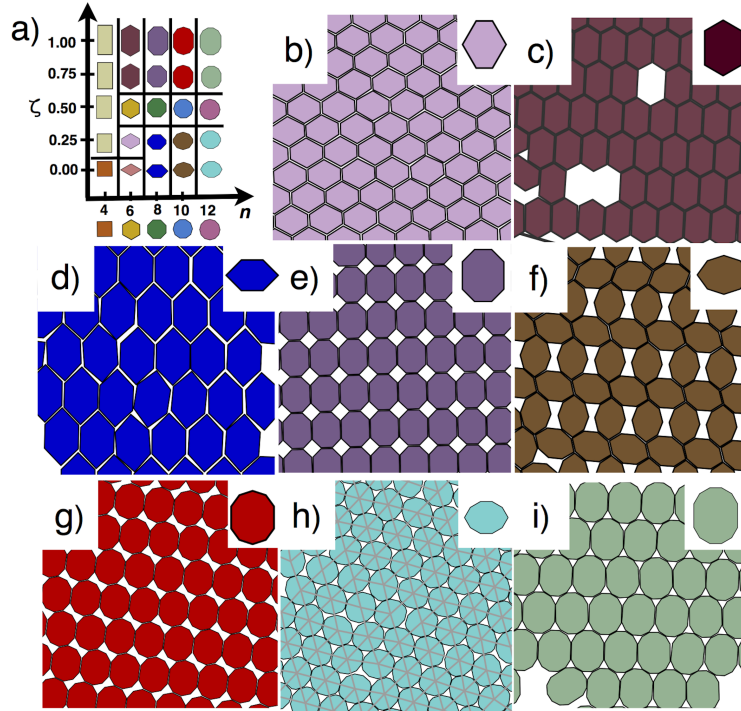


Figure 4.7: Effect of elongation on the self-assembly of polygons. (a) Faceting vs elongation phase diagram. The building blocks for each geometric state point are shown in the geometric phase diagram. Representative snapshots (b-I) of crystal structures self-assembled from elongated polygons that deviate from those formed from regular n -gons ($\zeta = 0.5$) are: (b) a space-filling structure for compressed hexagons ($\zeta = 0.25$) hexagons ($n = 6$), (c) a space-filling structure for elongated ($\zeta = 0.8$) hexagons ($n = 6$), (d) a space-filling tiling formed from fully compressed ($\zeta = 0.0$) octagons ($n = 8$), (e) a stretched (4.8^2) Archimedean tiling for elongated ($\zeta = 0.8$) octagons ($n = 8$), (f) a complex porous structure for fully compressed ($\zeta = 0.75$) decagons ($n = 10$), (g) an oblique porous tiling for elongated ($\zeta = 0.8$) decagons ($n = 10$), (h) a degenerate triangle lattice for compressed odecagons ($\zeta = 0.0$), (i) an Archimedean tiling for elongated ($\zeta = 1.0$) dodecagons ($n = 12$).

Truncation continuously transforms the triangle ($n = 3$) into a hexagon ($n = 6$). Triangles and hexagons form (3^6) and (6^3) and Archimedean tilings, respectively. In 3D, truncation of tetrahedra leads to multiple transitions among quasicrystal, diamond, beta-tin, high pressure lithium and bcc crystal structures³⁴. However, in 2D, we find that the effect of truncation is less profound. The truncated triangle modifies the (3^6) Archimedean tiling by adding hexagonal pores with areas proportional to the degree of truncation while still preserving a nearest-neighbor shell of three particles per polygon (Figure 4.8b). These porous tilings have not yet been reported in experiments. Halfway between triangles and hexagons ($\gamma \sim 0.65$), the irregular polygon, now with six edges, changes coordination number from three to six and can point randomly in six different directions, forming a rotationally degenerate hexagonal lattice. The change in coordination number indicates the onset of a transition towards the (6^3) Archimedean tiling from a honeycomb structure. Indeed, at $\gamma = 1.0$ the polygon becomes a regular hexagon and the (6^3) Archimedean tiling is formed. The transformation between the (3^6) Archimedean tiling to the (6^3) Archimedean tiling shows that shape transformation can have subtle, gradual effects on the assembled structures. The truncated square ($n = 4$) and octagon ($n = 8$) form crystals that are closely related. The truncated square at intermediate truncation $\gamma = 0.25$ forms a Mediterranean tiling (Figure 4.8c). The Mediterranean tiling is similar to the (4.8^2) Archimedean tiling but the square tile is either smaller or truncated. These porous structures have been realized in osmotically concentrated monolayers of microplatelets³².

The truncated heptagon stabilizes a dodecagonal quasicrystal similar to the one observed for this polygon under the pinch transformation (Figure 4.8d). This complex aperiodic structure forms for low and intermediate truncation values ($0.25 \leq \gamma < 0.75$). Such tilings have not yet been reported in experimental self-assembly of nanoplates. At higher truncation $\gamma = 0.75$, the truncated heptagon acts like a

tetradecagon and forms porous center lattices (Figure 4.4m). The proximity in shape space of these two structures motivates the possibility of a switchable structure.

The truncated octagon forms an irregular star polygon tiling. This irregular star polygon tiling is closely related to the $(8.4_{\pi/4}^*.8.4_{\pi/4}^*)$ regular star polygon tiling formed by symmetric truncation¹⁰¹. Oblique closed packed assemblies of PbS nanostars have been achieved by vertical deposition¹⁰³. However, the porous tilings illustrated in Figs 4.8c and e have not yet been reported in experimental (2D) self-assembly of nanoplates. The truncated octagon provides a simple means of obtaining a patterned array of star-shaped pores (Figure 4.8e). The truncation of regular n -gons with a large number of vertices alters the pore structure, but not the coordination of the crystal structure.

4.6 Discussion

The shape optimization of faceted nanoplates for assembly begins with understanding the effect of different shape transformations on the assembly of polygons representing nanoplates. Specific shape transformations provide the material designer with new design axes to synthesize new functional materials (See Appendix Section A). For example, we showed that truncation and elongation allow the synthesis of porous tilings such as porous alternating tilings and porous mediterranean tilings (Fig. 4.6g, 4.7e), pinching allows for the stabilization of the pentagonal Cairo tiling or the prismatic pentagonal tiling (Fig. 4.4e, f), and poor assemblers in the regular n -gon family, such as the nonagon, heptagon, and pentagon, can be self-assembled into crystals by judicious use of one of the shape transformations discussed.

Our results can be summarized into three classes of tilings: space-filling, porous, and complex (Fig. 6 4.9a,b and c). Colored arrows indicate which of the four transfor-

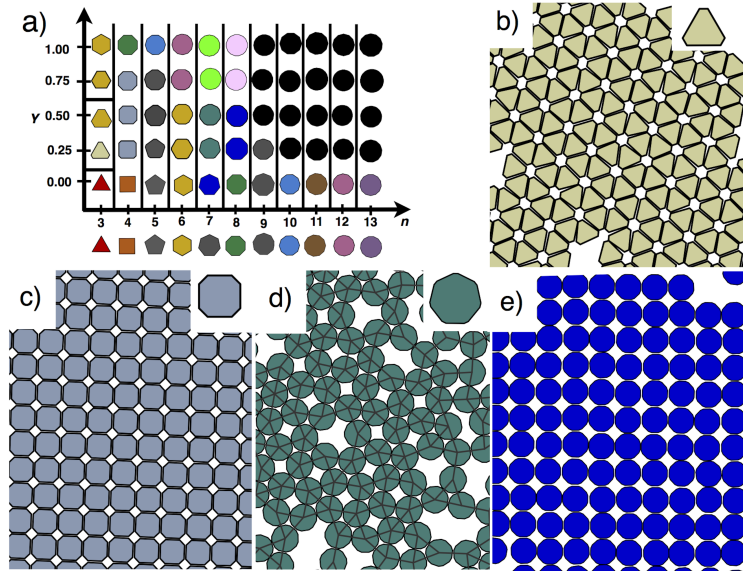


Figure 4.8: Effect of truncation on the assembly of polygons. (a) A geometric diagram for the faceting and truncation anisotropy dimensions shows the crystal phases observed. Grey n -gons imply a frustrated assembly. The building blocks for each geometric state point are shown on the phase diagram. Representative snapshots of crystal structures (b-e) observed for truncated polygons that deviate from those structures observed for regular n -gons ($\gamma = 0$). (b) A porous (3^6) Archimedean tiling for slightly truncated ($\gamma = 0.25$) triangles ($n = 3$), (c) Mediterranean tiling for truncated ($\gamma = 0.5$) squares ($n = 4$), (d) dodecagonal quasicrystal at $\gamma = 0.38$ and $n = 7$, and (e) a regular star polygon tiling for truncated ($\gamma = 0.5$) octagons ($n = 8$).

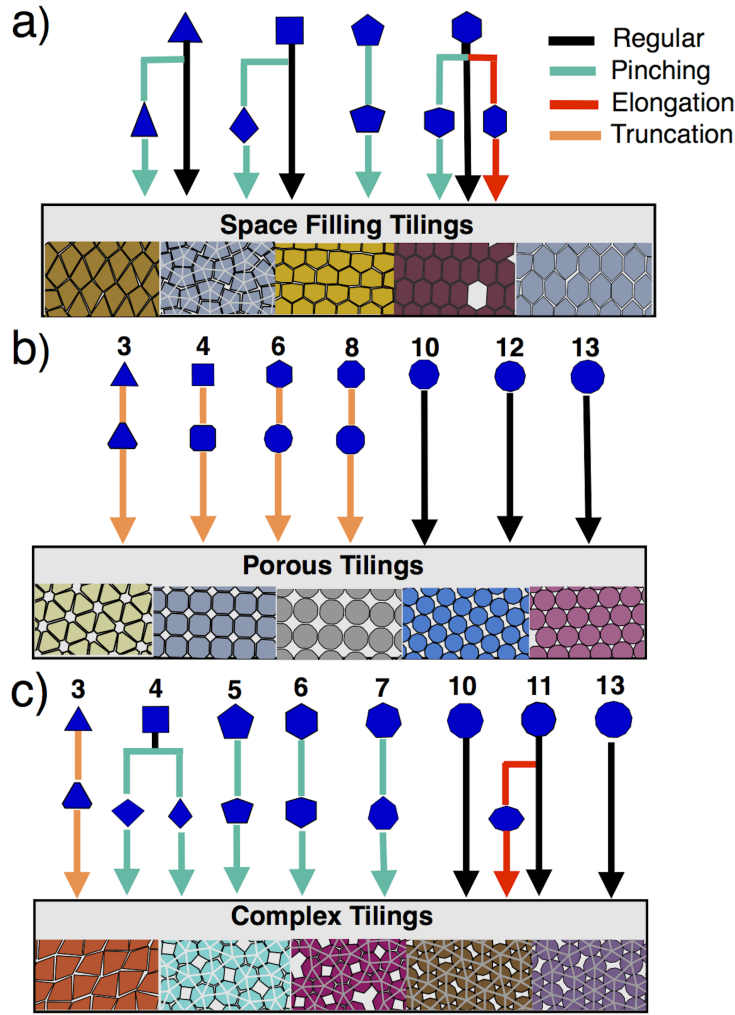


Figure 4.9: A classification of the different tilings observed as a function of shape transformation. (a) A summary of all the transformed polygons (nanoplates) that formed space-filling tilings. Judiciously pinched and non-pinched triangles, squares and hexagons assemble into space-filling tilings. Elongated hexagons formed structures that completely tile the two-dimensional plane. (b) Degenerate and regular porous structures form from truncated triangles, squares, hexagons, heptagons, octagons, nonagons, decagons, hendecagons, dodecagons and tridecagons. Regular octagons, decagons, hendecagons, dodecagons and tridecagons also form long-range ordered porous structures. (c) Complex structures can be assembled from pinched squares, pentagons, hexagons, heptagons, regular decagons, (elongated) hendecagons and tridecagons.

mations, when applied on a given shape, results in one of the three classes mentioned above. Some structures can be simultaneously in two of these categories. Also, degenerate crystal structures appear after applying small transformations. Space-filling tilings form from regular triangles, squares and hexagons (Fig. 4.9a). This is expected since these polygons constitute the tiles that form regular Archimedean tilings. Also, moderate pinching of these regular polygons and elongation exclusively applied to hexagons leads to space-filling assemblies. Porous tilings (Fig. 4.9b) are formed by regular octagons, decagons, undecagons, dodecagons and tridecagons. Truncated triangles, squares, hexagons, heptagons, octagons and undecagons also form porous tilings. The benefit of using irregular faceted polygonal nanoplates is that the pore size can be dynamically tuned in experiments *via* truncation using photodecomposition¹⁰⁴. Complex tilings with multiple nanoplates in a unit cell (Fig. 6 4.9c) is observed for irregular triangles, square pentagons, hexagons, heptagons and decagons. The majority of the complex tilings occur due to the pinch transformation and at low n (Fig. 6 4.9c). Other interesting complex tilings we observe include the pentagonal Cairo tiling (Fig. 4.6e). The location of these interesting structures in the geometric phase diagram (pinched, small n polygonal nanoplates) should motivate experimental studies on monodisperse irregular nanoplates. The rotationally degenerate complex tilings are found in pinched nonagons, decagons and elongated dodecagons. A degenerate structure from irregular dodecagons is expected because elongated pear-like colloidal dimers also form disordered rotator crystals¹⁰⁵. On the other hand, the degenerate crystal structure of asymmetric pinched nonagons and decagons is analogous to the assembly of hard asymmetric dimers¹⁰⁵.

Looking beyond the present study, highly symmetric faceted nanoparticles such as the Johnson and Archimedean polyhedra have been predicted to form crystals ranging from quasicrystals to diamond to Frank-Kasper crystals with large unit cells. The shape transformations studied here can increase or decrease the symmetry of

effectively two-dimensional versions of faceted nanoparticles such as those. The elongation and pinch transformations decrease the symmetry of the building block but these building blocks stabilize complex and porous tilings (Figs. 4.9, 4.7 and 4.9). In contrast, the truncation transformation increases the symmetry of the building block and stabilizes porous and lattice tilings (Figs. 4.8 and 4.9). These two results highlight, again, that the symmetry of the building block may not be a sufficient indicator to predict the self-assembly prospects of a material. Experimental work to synthesize irregular nanoplates could lead to significant progress in understanding the effect of symmetry and shape on self-assembly.

From the perspective of material optimization, the improved assembly properties of the regular heptagon highlight the power of shape transformations. The frustrated (non)-assembly of the regular heptagon has two local motifs at low densities: the snub square ($3^2.4.3.4$) Archimedean tiling and the shield-triangle tiling. Both motifs are observed in the shield dodecagonal quasicrystal. The pinch transformation allows for the self-assembly of the snub square and the dodecagonal quasicrystal structures by relaxing geometric constraints (overlapping) between heptagons when attempting to locally form triangular arrangements. Similarly, truncation applied to heptagons relaxes local geometric constraints, allowing for the formation of dodecagonal quasicrystals. These shape transformations provide a means of toggling among different structures in the case of active (in-situ) shape change^{73,85,106–108}. The judicious use of geometric transformations could lead to the self-assembly of new exotic structures as shown in Figs 4.10- 4.19.

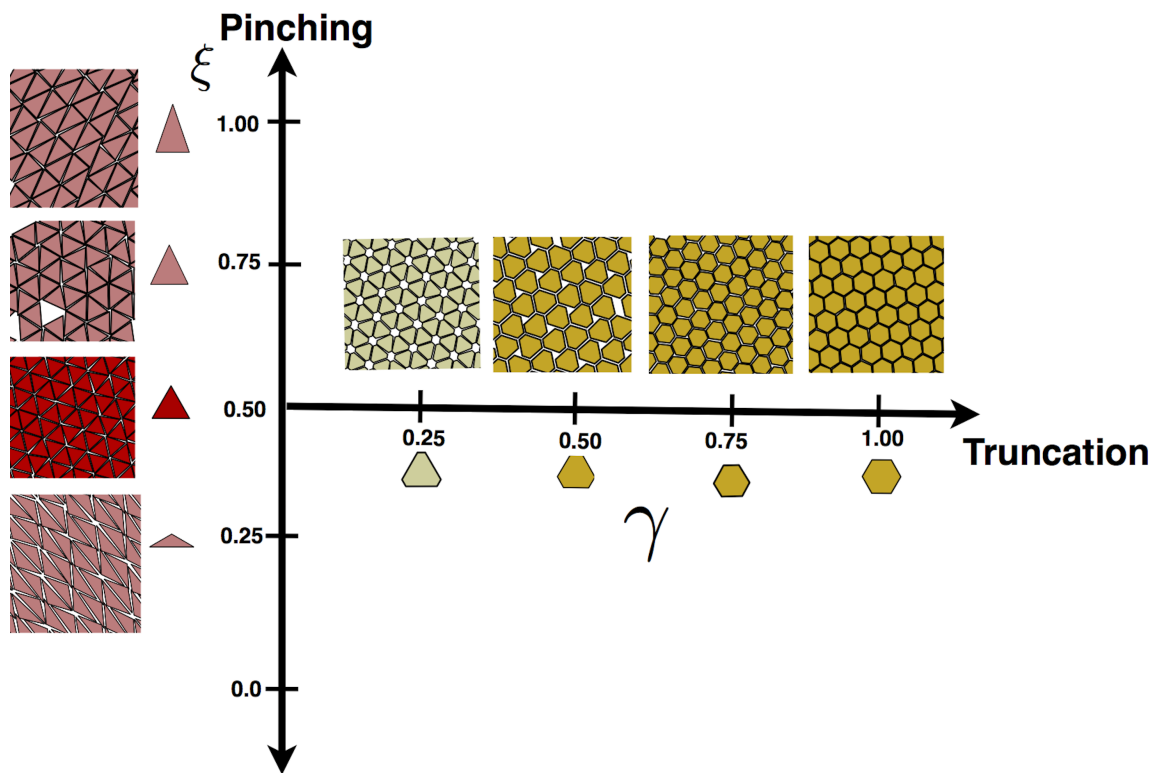


Figure 4.10: Phase behavior of triangles along the shape transformations pinching (ξ) and truncation (γ). Pinching a regular triangle leads towards a transformation from (3^3) Archimedean tilings ($\xi = 0.25$) to oblique lattices ($\xi = 0.50, 0.75$ and 1.0). Slight truncations of triangles nanoplates forms porous triangular tilings. As truncation increases, triangles transform into hexagon, and a transition from triangular tilings towards hexagonal (6^6) Archimedean tilings are observed. At intermediate and higher values values of γ , degenerate (6^6) Archimedean tilings are self-assembled.

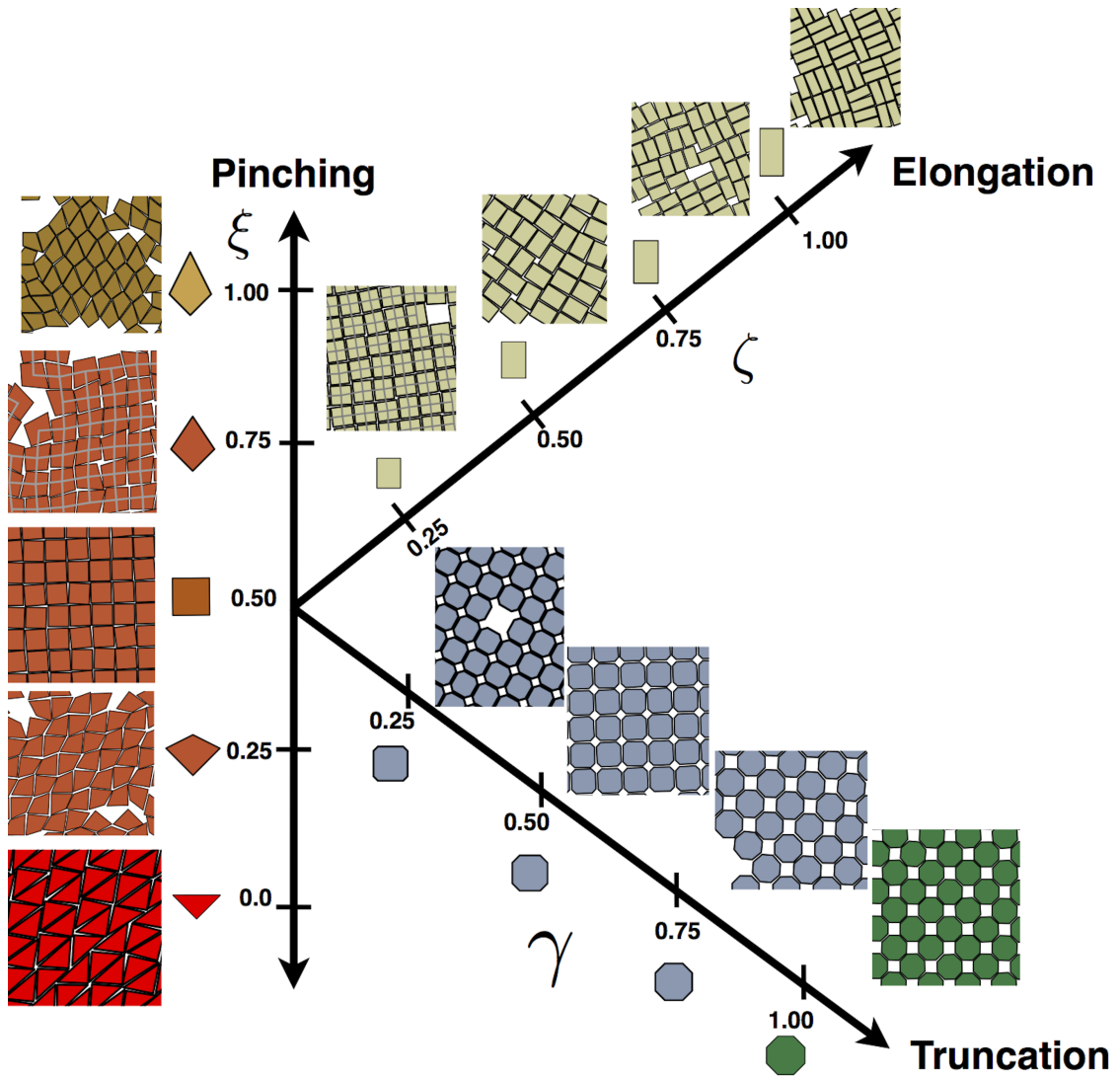


Figure 4.11: Phase behavior of squares along the shape transformations: pinching (ξ), truncation (γ) and elongation (ζ). Pinching transforms a squares into a kite leading to the formation of hierarchical kite crystal ($\xi = 0.25$), square (degenerate) Archimedean tilings ($\xi = 0.5$ and 0.5) and alternating hierarchical tilings ($\xi = 0.75$ and 1). Truncation of regular squares leads to the formation of squares lattices ($\gamma=0.25, 0.5$ and 0.75) and $(4^2.8^2)$ Archimedean tilings ($\gamma=1.0$). Slight elongation of regular squares leads to the formation of degenerate squares ($\zeta=0.25$) and of disorder lattices for $\zeta > 0.25$.

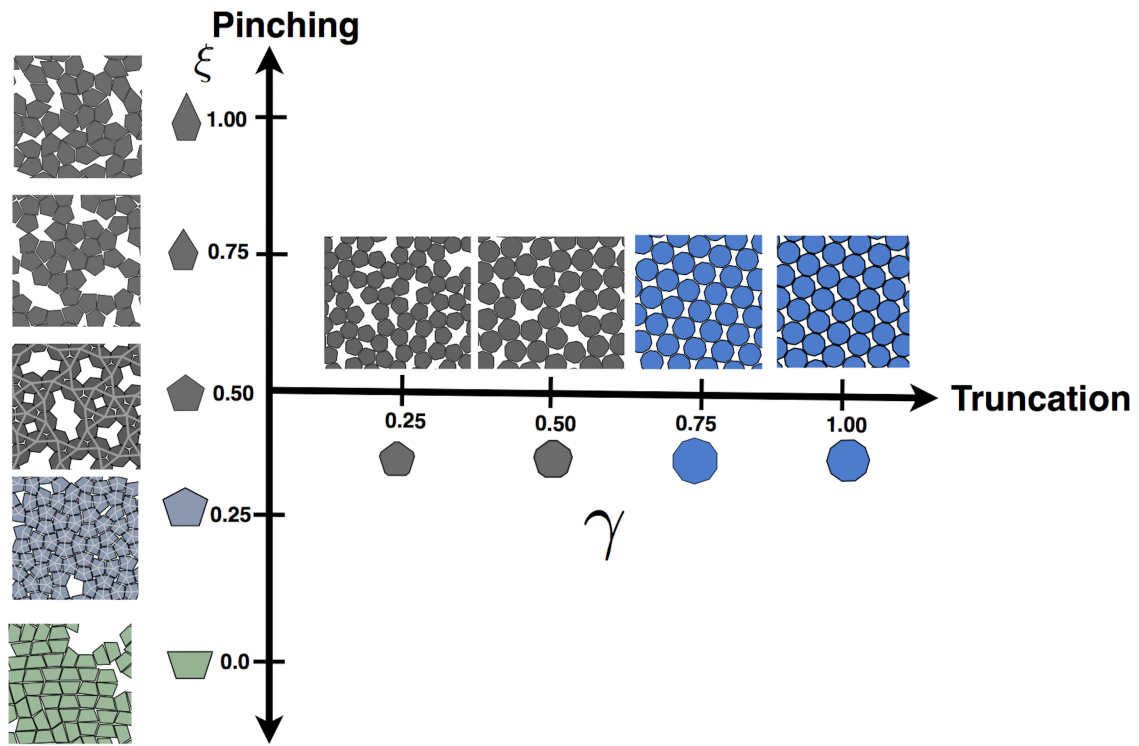


Figure 4.12: Phase behavior of pentagons along the shape transformations pinching (ξ) and truncation (γ). Pinching leads to the formation of trapezoidal tilings ($\xi = 0.00$), Cairo tilings ($\xi = 0.25$), frustrated ($\xi = 0.50$) and disorder assemblies ($\xi = 0.75$ and 1.00). Slight truncation of pentagons leads to disorder phases. For higher truncation values, the shape of the truncated pentagons resemble ($\gamma = 0.75$) and become that of decagons ($\gamma = 1.00$), leading to the formation of oblique structures reminiscent of those formed from regular decagons.

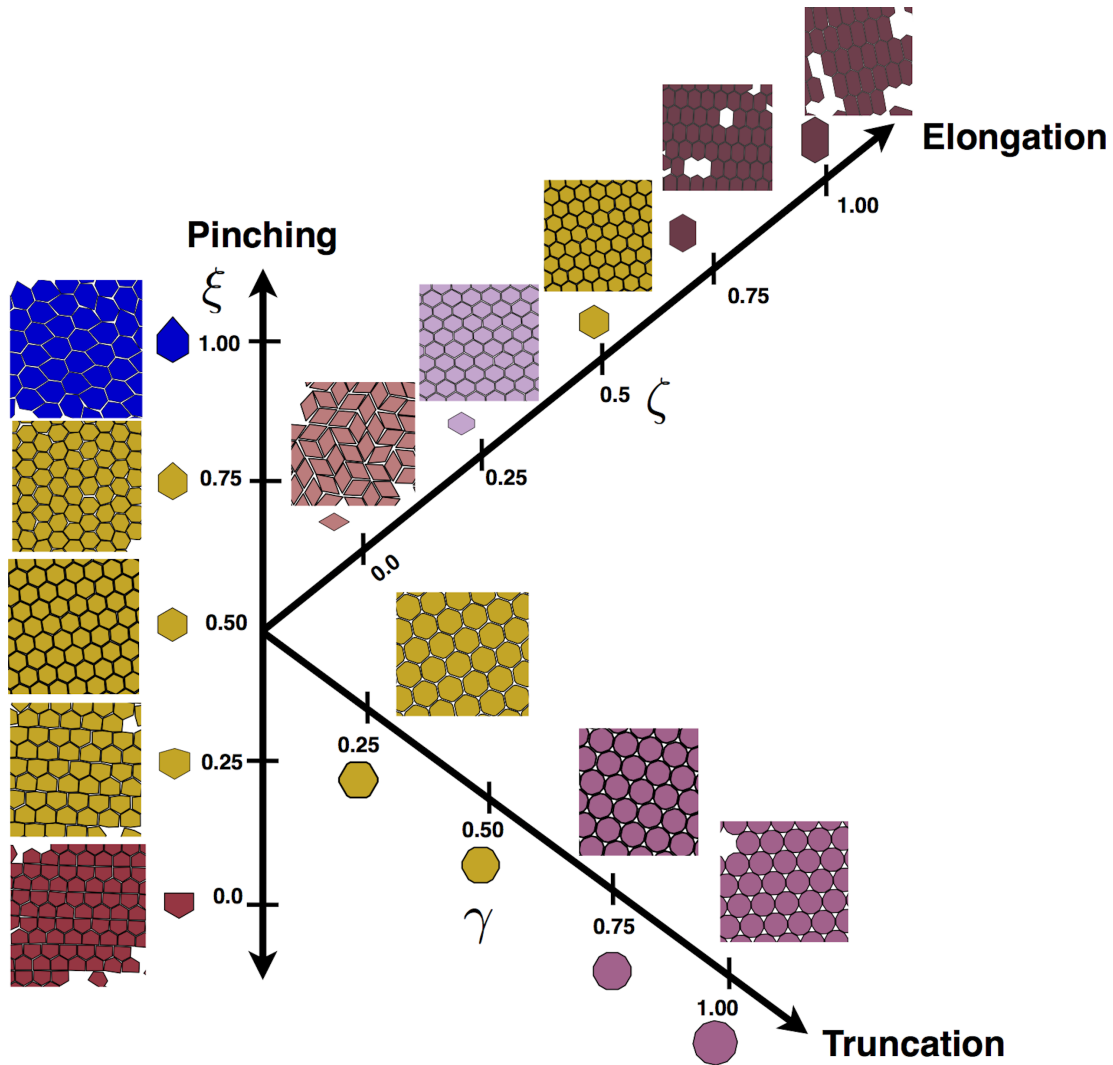


Figure 4.13: Phase behavior of hexagons along the shape following transformations: pinching (ξ), truncation (γ) and elongation (ζ). Pinching transforms an irregular pentagon ($\xi = 0.00$) into a pinched hexagon ($\xi = 1.0$). The following structures are observed for the pinching transformation: a prismatic structure ($\xi = 0.00$ and $\xi = 0.25$), a hexagonal (6^6) Archimedean Tilings ($0.25 < \xi = 0.75$) and alternating triangular tilings. Truncation of regular hexagons does not alter the hexagonal tiling but it introduces pores or empty tilings to the self-assembled structure. Elongation transforms rhombs with 60 degrees openings at opposite sides into regular and irregular hexagons. For the (compressed hexagon) rhombs, random tilings are observed and as the elongation transformation modifies rhombs into hexagons, shortened hexagonal (6^6) Archimedean tilings that elongate with the increase of ζ are observed.

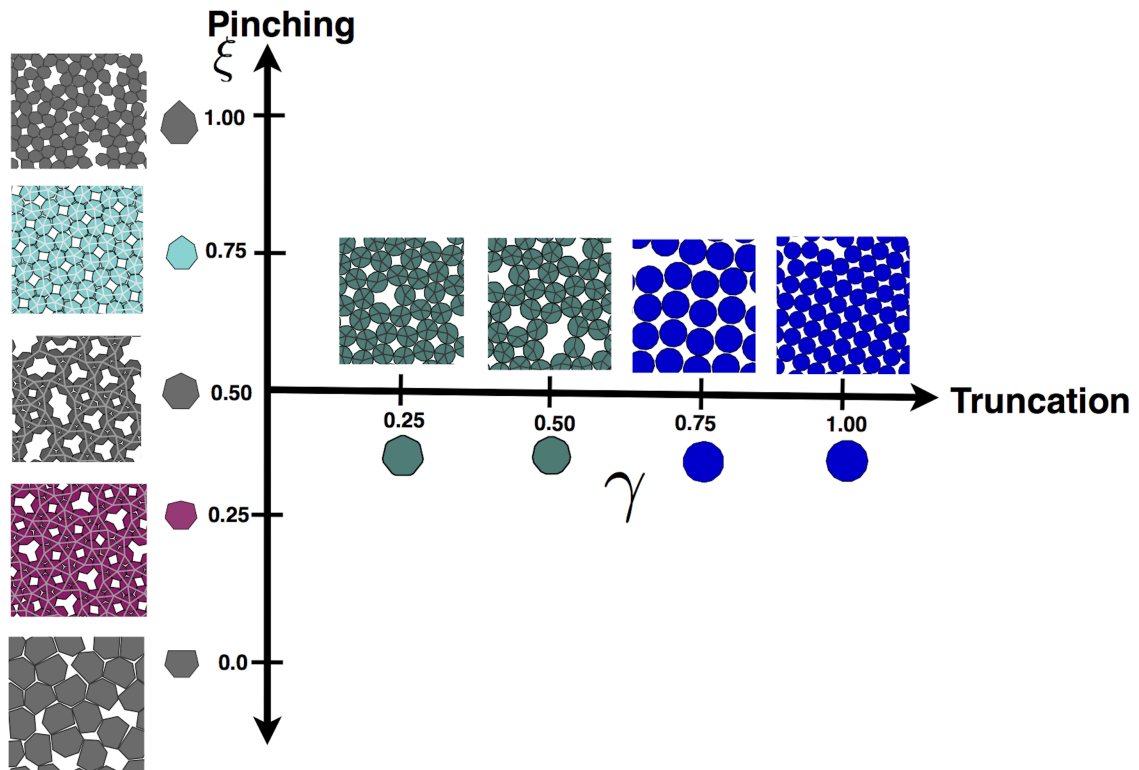


Figure 4.14: Phase behavior of heptagons along the shape pinching (ξ) and truncation (γ) shape transformations. Pinching leads to the formation of disorder tilings ($\xi = 0.00$), dodecagonal quasicrystals ($\xi = 0.25$), frustrated ($\xi = 0.5$) structures, sigma phase ($\xi = 0.75$) and frustrated structures ($\xi=1.0$). Slight truncation of heptagons leads to dodecagonal quasicrystal ($\xi = 0.25$ and 0.5) formation values. The shape highly truncated pentagons starts to resemble ($\gamma = 0.75$) and become that of tetradecagon ($\gamma = 1.0$), leading to the formation of oblique structures reminiscent of those formed from regular decagons.

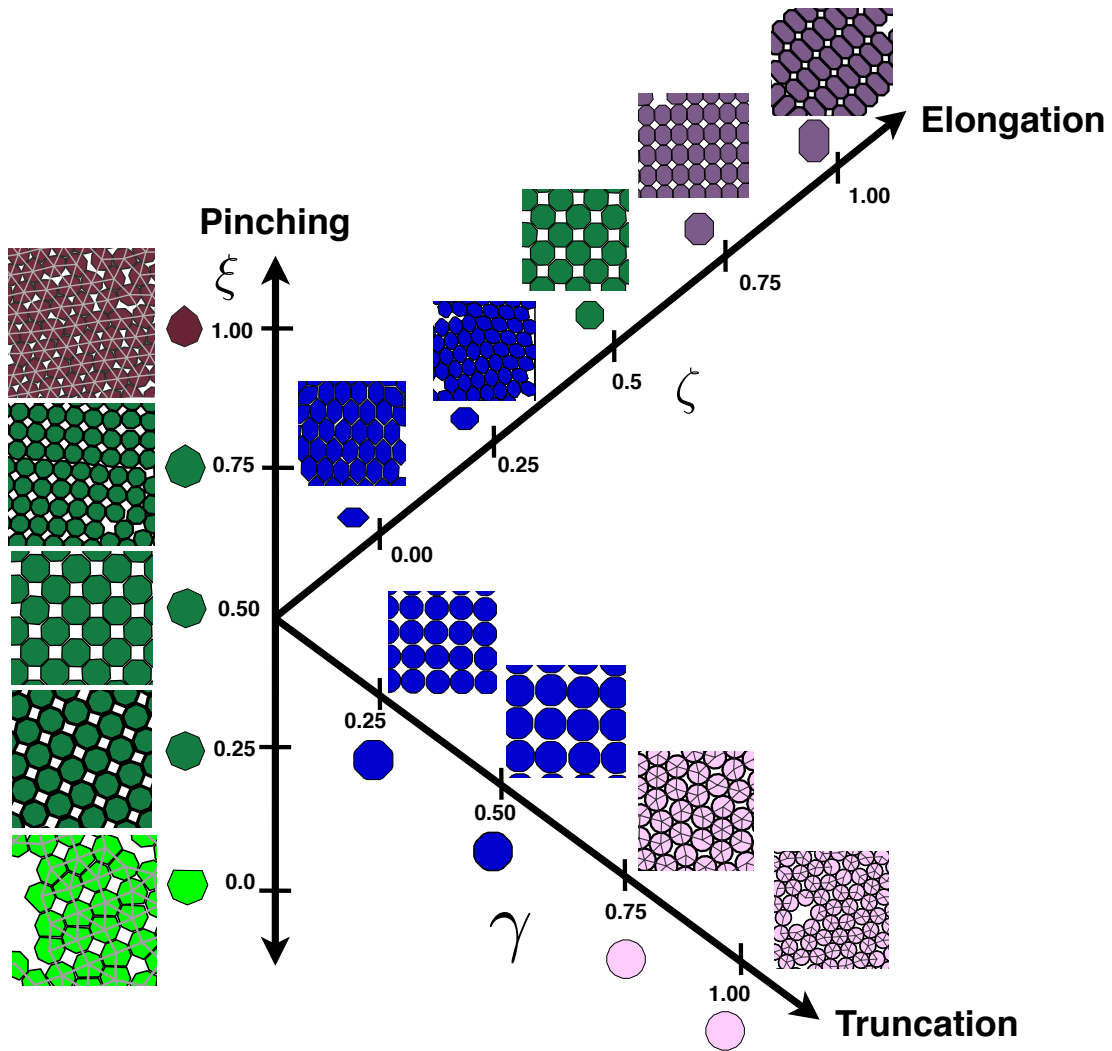


Figure 4.15: Phase behavior of octagons along the pinching (ξ), truncation (γ) and elongation (ζ) shape transforms. The following structures are observed for the pinching transformation: an $(3^3.4^2)$ Archimedean Tiling ($\xi = 0.00$), a (4.8^2) Archimedean tiling ($\xi = 0.25, 0.5$) which is degenerate for $\xi = 0.75$, and a degenerate structure with an underlying triangular tiling ($\xi = 1.00$) and an alternating triangular tilings. Truncation of regular octagons transform Archimedean tilings into star polygon tilings for $\gamma = 0.25$ and 0.5 . Further truncations lead to disk behavior. Elongation leads to parallel arrangements (ζ) and elongated $(8^2.4)$ Archimedean tiling ($\zeta = 0.50, 0.75$ and 1.00).

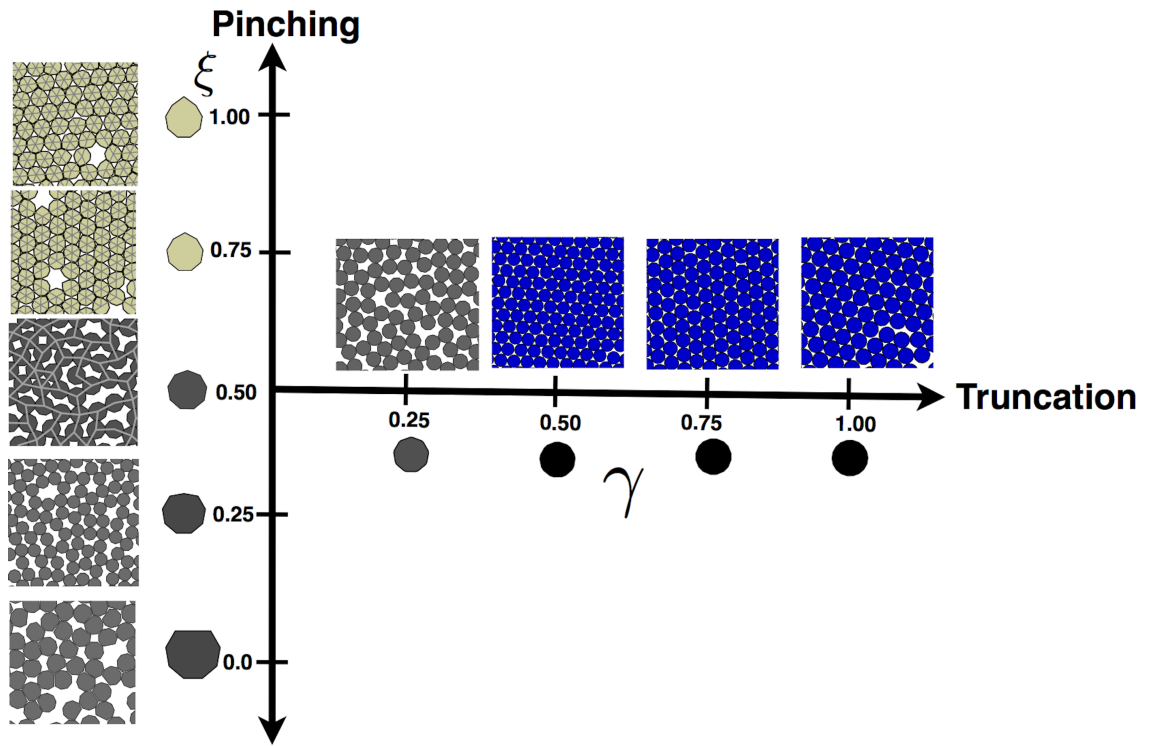


Figure 4.16: Phase behavior of nonagons along the shape pinching (ξ) and truncation (γ) shape transformations. Pinching leads to the formation of disorder tilings ($\xi = 0.00, 0.25$ and 0.5), and degenerate triangular lattice ($\xi = 0.75$). Slightly truncated nonagons form disorder structures, and further truncations leads to disk behavior were nonagons form hexagonal degenerate tilings ($\xi = 0.25$ and 0.5). The shape highly truncated pentagons starts to resemble ($\gamma = 0.5$) and become that of tetradecagons ($\gamma = 0.5, 0.75$ and 1.0).

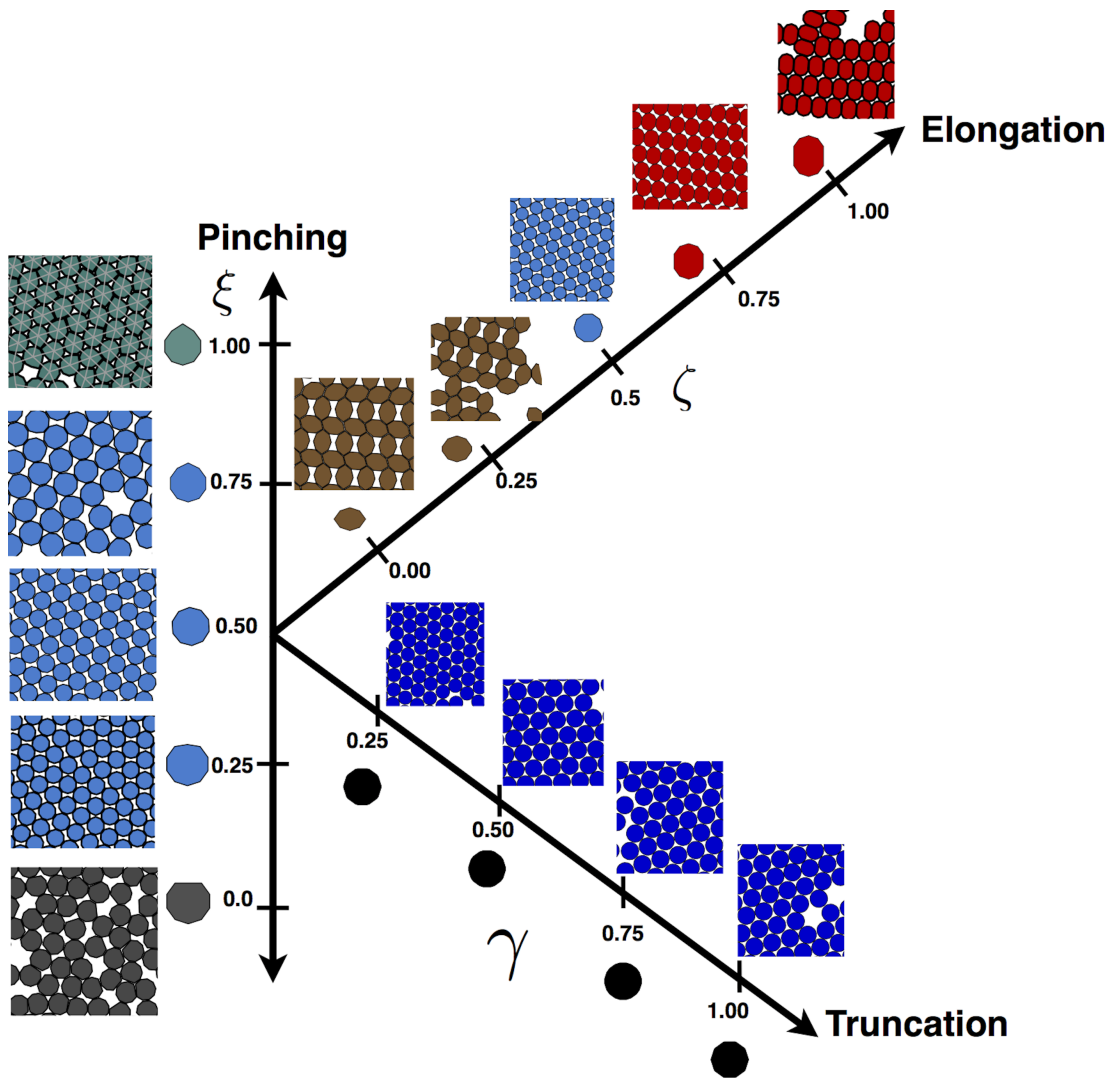


Figure 4.17: Phase behavior of decagons for the pinching (ξ), truncation (γ) and elongation (ζ) shape transformations. The following structures are for the observed for the pinching transformation: a disorder tilings ($\xi = 0.00$), and parallel lattices ($\xi = 0.25, 0.50, 0.75$) and triangular tilings ($\xi = 1.00$) Truncation (γ) leads to disk behavior. Elongation leads complex porous structures ($\zeta=0.25$ and 0.5), further truncations leads to (elongated) parallel lattices that resemble structures self-assembled from sticky decagons for $\zeta= 0.50, 0.75$ and 1.00 .

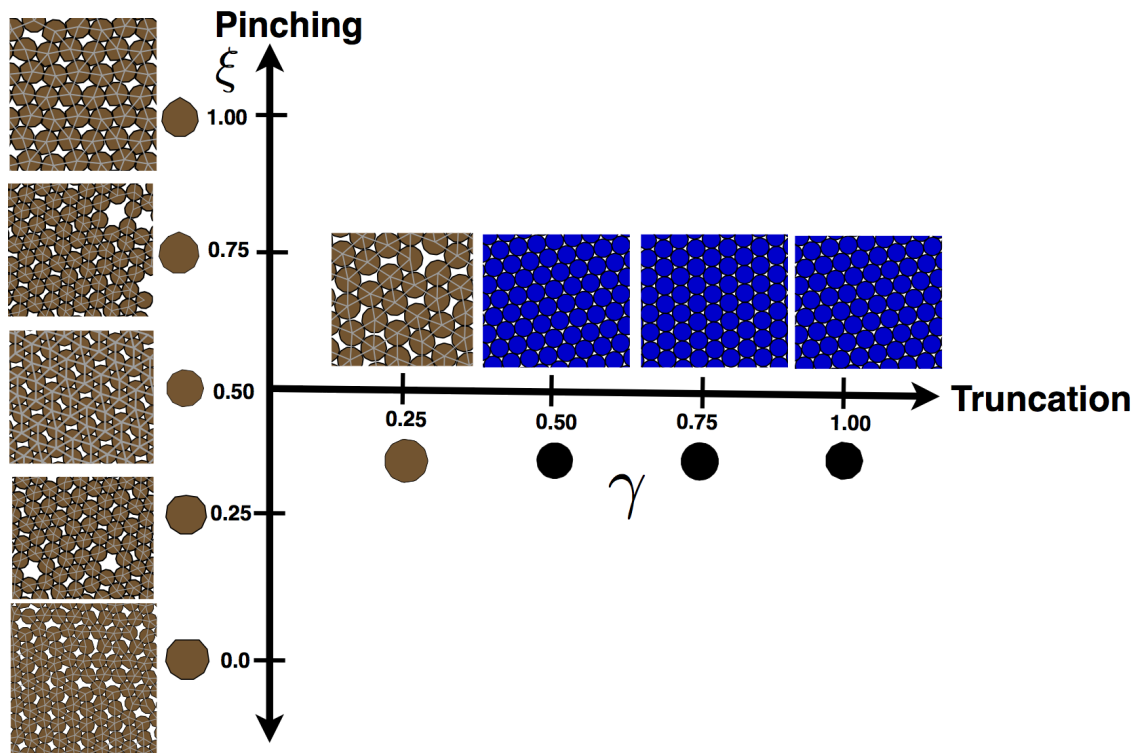


Figure 4.18: Phase behavior of hendecagons for the pinching (ξ) and truncation (γ) shape transformations. Regarding of the amount of pinching applied on the nonagons; a sheared $(3^2.3.4.3)$ Archimedean tiling is observed. Slightly truncated nonagons form $(3^2.3.4.3)$ Archimedean tiling, and further truncations leads to disk behavior were nonagons form hexagonal degenerate tilings ($\xi = 0.25$ and $0.5, 0.75$ and 1.0).

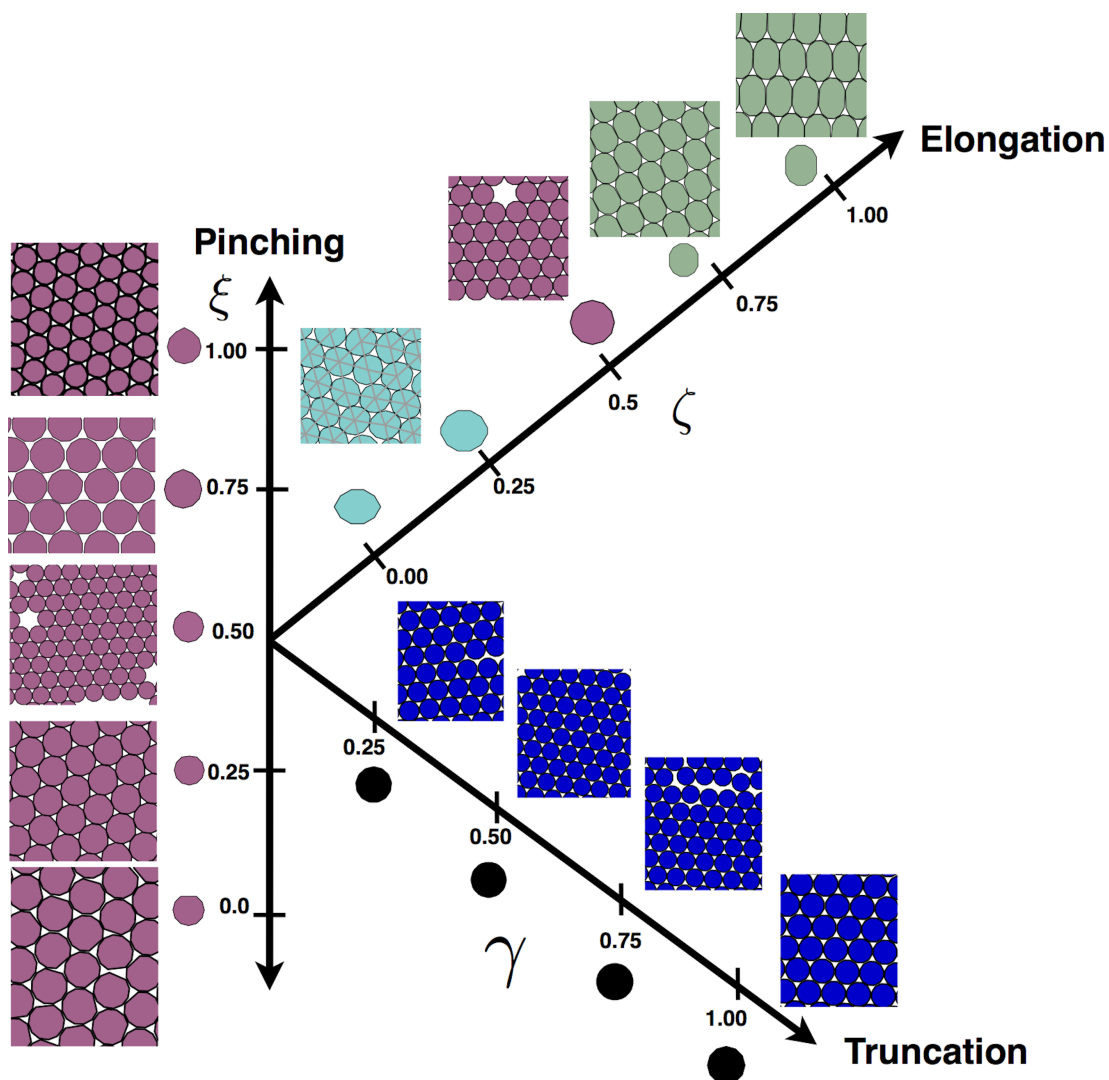


Figure 4.19: Phase behavior of dodecagons for the pinching (ξ), truncation (γ) and elongation (ζ) shape transformations. Regardless of pinching applied on the dodecagons, hexagonal center-to-center tilings are observed. ($\xi = 0.25, 0.50, 0.75$ and 1.00). For intermediate and high pinching (3.12^3) Archimedean tiling are self-assembled. Truncation (γ) leads to disk behavior. Elongation leads to degenerate triangular lattices for compressed dodecagons ($\zeta = 0.00$ and 0.25), further truncations leads to (elongated) 3.12^3 Archimedean tiling for $\zeta = 0.50, 0.75$ and 1.00 .

4.7 Conclusion

Building an experimental toolbox for self-assembly as a systematic design framework could transform the field of self-assembly from a basic scientific discipline to an engineering discipline. We showed that continuous shape transformation in the presence of short-ranged attractive forces stabilizes space-filling, porous and complex tilings at intermediate densities. The proposed design rules constitute a first step towards the understanding of shape optimization and highlight a deeper study of its effect on self-assembly. The development of heuristic rules for shape optimization would allow experimentalists to tune the shapes of anisotropic building blocks to select and improve the crystal properties of target assemblies. Furthermore, an understanding of the mechanisms to improve the assembly propensity of certain structures could allow for a priori screening of materials. Previous work shows that the fabrication of high performance nanocrystal-based devices^{42,109–111} with tunable interparticle spacing and electronic coupling¹¹¹, enhanced thermopower⁴² electrical and optical properties¹¹². Porous ZnO nanoplate structures are strong candidates for low-cost dye-sensitized solar cells¹¹³. These novel properties have applications to such diverse as solar energy, military and cosmetics, among others. We look forward for further experimental developments to validate the material design principles provided in this contribution.

CHAPTER V

Self-assembly of Archimedean tilings with enthalpically and entropically patchy polygons

The results of this chapter were published in:

J. A. Millan, D. Ortiz, S.C.G. Glotzer, Self-Assembly of Archimedean Tilings with Enthalpically and Entropically Patchy Polygons, ACS Nano, 8(3), 2918-2928, February 2014

5.1 Abstract

Considerable progress in the synthesis of anisotropic patchy nanoplates (nanoplatelets) promises a rich variety of highly ordered two-dimensional superlattices. Recent experiments of superlattices assembled from nanoplates confirm the accessibility of exotic phases and motivate the need for a better understanding of the underlying self-assembly mechanisms. Here, we present experimentally accessible, rational design rules for the self-assembly of the Archimedean tilings from polygonal nanoplates. The Archimedean tilings represent a model set of target patterns that (i) contain both simple and complex patterns; (ii) are comprised of simple regular shapes; and

(iii) contain patterns with potentially interesting materials properties. *Via* Monte Carlo simulations, we propose a set of design rules with general applicability to one- and two-component systems of polygons. These design rules, specified by increasing levels of patchiness, correspond to a reduced set of anisotropy dimensions for robust self-assembly of the Archimedean tilings. We show for which tilings entropic patches alone is sufficient for assembly, and when short-range enthalpic interactions are required. For the latter, we show how patchy these interactions should be for optimal yield. This study provides a minimal set of guidelines for the design of anisotropic patchy particles that can self-assemble all 11 Archimedean tilings.

5.2 Introduction

Tessellations comprised of regular polygons that completely tile the two-dimensional Euclidean plane have been studied since ancient times due to their mathematics and visually attractive symmetries¹⁰¹. Johannes Kepler identified 11 plane-filling tilings known as the Archimedean tilings (ATs)¹¹⁴, which can be divided into two groups, namely regular (Figure 5.1 a,d,g) and semi-regular tilings (Figure 5.1j-q) made from regular polygons. The regular tilings are characterized by the ability to map flags (tuples of mutually incident vertices, edges and tiles) *via* tiling-related group symmetry actions (flag-transitivity), while the remaining semi-regular tilings are expanded with a more relaxed symmetry in mapping vertex pairs to each other by an acting group symmetry pertaining to the tiling (vertex-transitivity)¹¹⁴. Various materials on multiple length-scales are known to form the ATs, which exhibit striking photonic¹¹⁵ and diffusive properties⁹⁵. The (4.6.12) and (3².4.3.4) ATs possess complete photonic band gaps.³ Regular and semi-regular tilings are commonly observed in bulk solids, polymeric assemblies, and nanomaterials. Archimedean crystalline nets such as Al₂O₃ (6₃) and CuAl₂ (3².4.3.4) describe the coordination polyhedra in various crys-

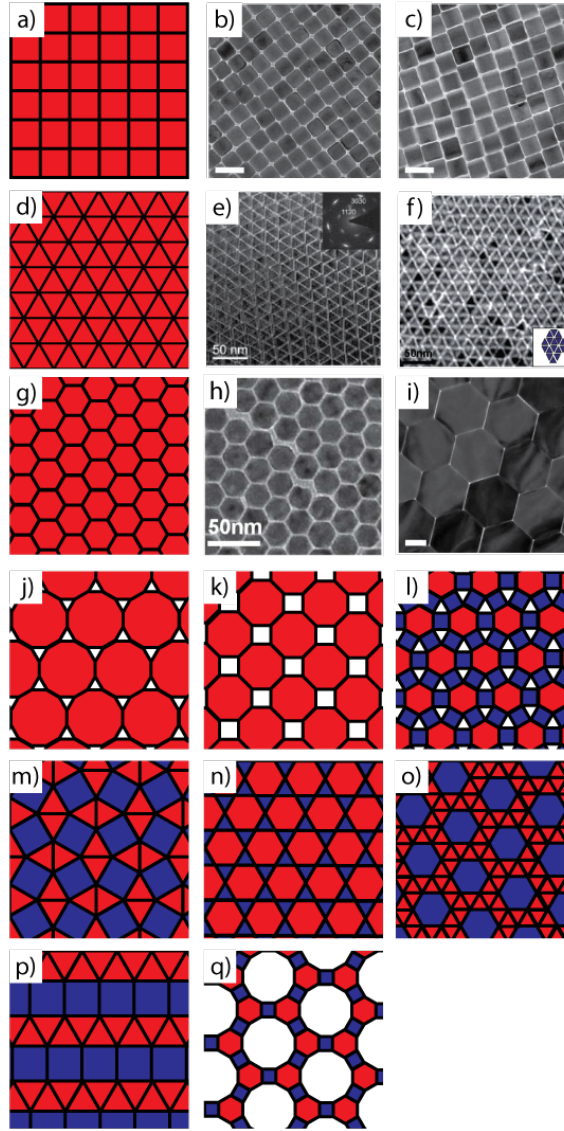


Figure 5.1: The 11 space-filling Archimedean tilings and published images of representative assemblies of the triangular (3^6), square (4^4), and hexagonal (6^3) AT tilings. Regular tilings: (a) square (4^4), (d) triangular (3^6) and (g) hexagonal (6^3). The experimental images of the regular tilings are (b) (4^4) β -NaYF₄ AT *Ye et al. (2010)*⁵, (c) NaYF₄: Yb/Er (4^4) AT *Ye et al. (2010)*⁵, (e) LaF₃ (3^6) AT *Zhang et al. (2005)*⁶, (f) Cu_{2-x}Se (3^6) AT *Shen et al. (2012)*⁷, (h) Cu_{2-x}Se (6^3) AT *Shen2012*, and (i) β -NaYF₄ (6^3) AT⁵. Semi-regular tilings: (j) truncated hexagonal (3.12^2), (k) truncated square (4.8^2), (l) rhombitrihexagonal ($3.4.6.4$), (m) snub square ($3^2.4.3.4$), (n) trihexagonal (or kagome) ($3.6.3.6$), (o) snub hexagonal tiling ($3^4.6$), (p) elongated triangular ($3^3.4^2$), and (q) truncated trihexagonal ($4.6.12$) tilings, which comprise the entire family of Archimedean tilings. In our simulations we consider colored and white polygons as hard nanoplatelets and pores, respectively.

tals of complex alloys⁹⁵. The more complex semi-regular tilings have been observed in the bulk structure of metallic alloys¹¹⁶ and supramolecular interfacial tessellations^{117,118}. Manifestations of regular and semi-regular tilings have been observed in liquid crystal¹¹⁹ (T-shaped molecules) and polymer systems¹²⁰ (ABC star branched polymers), and in systems of patchy nanocrystals. The self-assembly of polystyrene spheres in the presence of a decagonal quasicrystalline substrate has been shown to self-assemble the $(3^3.4^2)$ and (3^6) ATs¹²¹. Patchy triblock Janus colloids self-assemble the $(3.6.3.6)$ AT²⁹. Most of those results represent the ATs in a vertex-to-vertex representation where particle centers are placed at the vertices of the polygons in the tiling. The diversity of nanoscopic and microscopic components that assemble ATs motivates a need to understand the minimal design rules needed for the assembly of these tilings, in particular from readily accessible 2D nanoplates.

Anisotropic 2D nanoplates are known to have interesting electronic¹²², catalytic⁶⁴, and optical⁶⁵ properties, and have been shown to successfully form exotic superlattices *via* a subtle balance between shape-induced entropic patchiness¹²³ and ligand-induced enthalpic patchiness^{76,124}. 2D assemblies of nanoplates could be used in thin film electronics¹²⁵. Also, 2D assemblies of perovskites nanoparticles, such as Pb-TiO₃ nanoplates¹²⁶, have interesting ferroelectric and storage properties⁶⁷. Given their polygonal shape, faceted nanoplates could potentially self-assemble the ATs. Although assemblies of ATs from polygonal nanoplates have been reported in experiments^{1,5-7,23,48,55,127-130}, they are restricted to the regular ATs (those comprised of triangular, square, hexagonal nanoplates). Because faceted nanoplates can exploit both entropic and enthalpic patchy interactions, they represent a viable approach that could reduce the complexity of the design rules for self-assembly of elusive irregular and porous tilings, when compared to the vertex-to-vertex approach.

Numerical simulations have also predicted the self-assembly of the Archimedean

tilings. For spherical particles, simulations of patchy particles^{131,132} reported the self-assembly of all ATs except for the (3.6.3.6) AT. Di-tethered nanospheres³⁶ formed the (4.8²) and (6³) ATs. Lock and key colloids¹³³ and hard polyhedra^{15,33} formed the (3².4.3.4) and (6³) ATs, respectively. Despite these studies, numerical simulations have neglected the commonly synthesized polygonal nanoplates as a means of AT self-assembly.

Here, we report the minimal set of interactions needed to self-assemble experimentally accessible ATs from regular polygons, mimicking nanoplates assembled into crystalline monolayers (Figure 5.1). We show through Monte Carlo simulations the self-assembly of these tilings by exploiting entropic and enthalpic interactions encoded in the shape of the polygons. We arrive at a design strategy for patchy polygon particles that is accessible to current experimental techniques, and present the minimal set of design rules for each AT. We report that four ATs, namely the (6³), (3⁶), (4⁴), and (3.12²) tilings, can be assembled solely with hard interactions, highlighting the role of directional entropic forces^{39,40} that arise from the particle shape. We quantify the strength of these entropic patches⁷⁵ by calculating the potential of mean force and torque using free energy calculations¹²³. Symmetric enthalpic patches ((4.8²)), shape specific patches ((3².4.3.4), (3.4.6.4), (3.6.3.6)), and edge specific patches ((3³.4²), (3⁴.6), (4.6.12)) are needed to self-assemble the remaining crystalline structures. Beyond the ATs, the design rules presented provide general insight into the design of complex crystal structures using anisotropic building blocks.

5.3 Model and approach

Each nanoplate is modeled as a hard convex regular polygon with a finite number of edges $N = 3, 4, 6, 8$ and 12. In the first model -that of least complexity- no additional

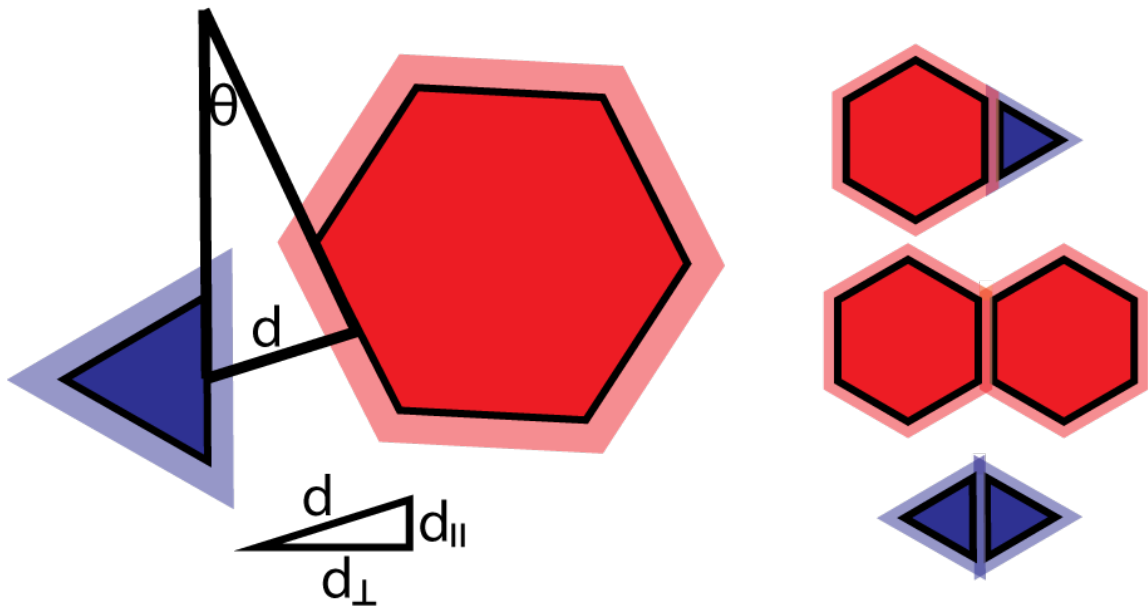


Figure 5.2: Schematic indicating the shape-specific interactions between nanoplates used for the shape-selective interaction case. (Left) Each shape is surrounded by a soft shell, which represents the range of the enthalpically patchy interaction. The interaction between the nanoplates is edge-to-edge and short-ranged, and depends on the distance shift d_{\parallel} , the normal distance d_{\perp} and angle (θ) between the edges. (Right) Schematic for hexagon-hexagon, hexagon-triangle, and triangle-triangle interaction shows the selectivity of the patchy interaction.

interactions are included. Initially, we find those ATs ((3^3) , (4^4) , (6^3) , (3.12^2)) that can be assembled by entropic forces alone. In all cases, shape anisotropy gives rise to entropic patchiness that emerges upon crowding and is density dependent⁷⁵.

For the remaining ATs, we introduce a short-range attractive edge-to-edge interaction potential. The interaction potential is divided into parallel, perpendicular and angular components (Figure 5.2). The parallel component represents the amount of parallel contact between interacting edges. The perpendicular component models the commonly observed attractive van der Waals force between ligand-capped nanocrystals¹³⁴, depends on the distance between centers of edges, and is approximated by a parabolic well. The angular component penalizes any misalignment between neighbor-

ing nanoplates representing steric forces between ligand shells. A halo drawn around the building block represents the interaction range of the edge-edge pair potential (Figure 5.2). Different colors represent different interaction strengths between edges. These enthalpic patches act as reversible, directional, sticky bonds that compete or combine with entropic patches. The justification of such a short-range potential in a nanoplate system is based on the presence of adsorbed ligands (e.g. oleic acid molecules)^{76,135}.

The complexity of the edge-to-edge interactions is determined by the targeted AT. We use three enthalpic models of increasing complexity for the assembly of the remaining ATs: symmetric, shape-specific and edge-specific. The first enthalpic model treats the pairwise interaction between polygons as patches of equal strength distributed over all edges. The second enthalpic model (shape-specific), which is a modification of the previous model, tunes the interaction strength between patches of dissimilar polygons for those ATs comprised of binary tile mixtures. The third enthalpic model (edge-specific) further increases the interaction complexity and determines the interaction strength based on the type of edges even for similarly shaped particles. To quantify the interaction asymmetry between different edges, we introduce the parameter α . The values reported are the minimum asymmetry needed to assemble the target ATs. For each AT tiling, we find a favorable thermodynamic state point for self-assembly of the building block.

5.4 Results

We present our findings in four categories based on the four types of interaction sets needed to assemble the Archimedean tilings: (i) entropic, (ii) symmetric, (iii) shape-specific and (iv) edge specific enthalpic interactions. All ATs can be self-assembled

with these four interaction approaches. The results are summarized in Figures 5.5 and 5.9.

5.4.1 Entropic interactions

Directional entropic forces arising from shape entropy, or a drive to local dense packing, are an entropic strategy to self-assemble the Archimedean tilings^{75,133,134,136}. In our studies, by changing the number of vertices of the building block, regular polygons are shown to self-assemble four of the ATs.

Regular triangles and squares form the (3^6) and (4^4) ATs, respectively (Figure 5.3 a, b). Insets show the regular polygon building block and a close-up of the assembly. The accompanying diffraction patterns show sharp peaks in hexagonal and square reciprocal lattices for triangles and squares, respectively, as a manifestation of long-range order. The small number of defects highlights the robustness of the assembly of both regular triangular and square tilings. However, there exists a collection of crystalline structures that differ from the triangle and square ATs solely by a shift vector along the lattice axes. Although at infinite pressure all of these tilings belong to a thermodynamically stable degenerate set with equal probability for self-assembly, we observe that at finite pressures the (3^6) and (4^4) ATs are the equilibrium configurations. Previous work has also shown that the equilibrium structures of hard triangles and squares at high packing fractions are the (3^6) and (4^4) ATs, respectively^{32,86,137}. Hard hexagons readily form the (6^3) AT (Figure 5.3c) at finite pressures. This is the unique infinite pressure (maximum density) crystal structure for the regular hexagon due to shape constraints.

All of the ATs are, by definition, space filling. However, by treating some tile types as pores, it is possible to assemble some multi-tile ATs with a single nanoplate

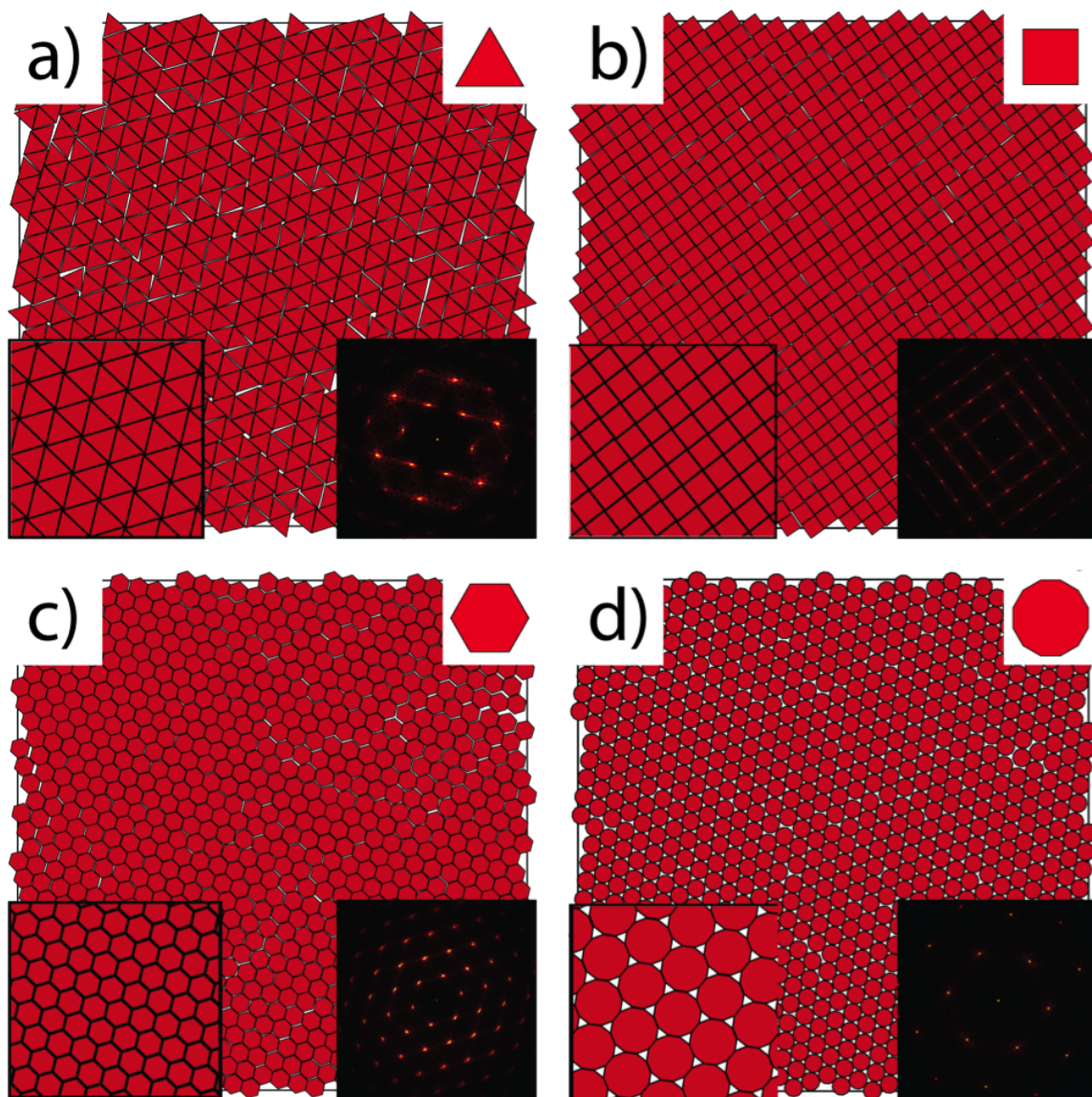


Figure 5.3: Representative snapshots of sections of larger simulations for the (3^6) , (4^4) , (6^3) , and (3.12^2) ATs self-assembled with excluded volume interactions only. Insets show the nanoplate, a diffraction pattern of the snapshots, and a compressed close-up. (a) Triangles self-assemble the (3^6) tiling at a packing fraction of 0.90, (b) squares self-assemble the (4^4) tiling at a packing fraction of 0.94, (c) hexagons self-assemble the (6^3) tiling at a packing fraction of 0.93, and (d) dodecagons self-assemble the (3.12^2) tiling at a packing fraction of 0.85.

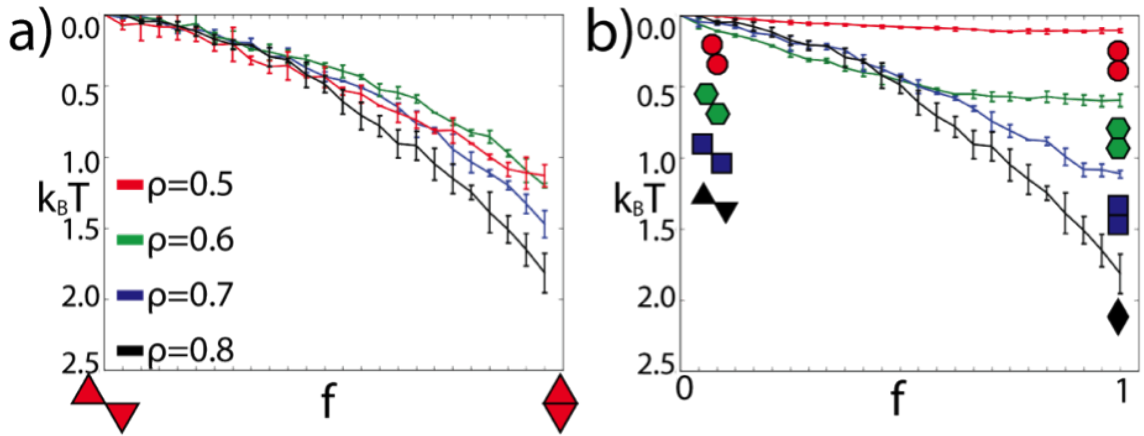


Figure 5.4: (a) Effective free energy difference between different configurations of hard triangles as a function of density. (b) The effect of shape on the effective free energy difference at fixed density. The free energy difference is shown as a function of misalignment factor f , which quantifies the edge-edge coverage between two pairs of anisotropic particles. In (a), the free energy gain for edge-edge alignment in triangles is $1.2k_B T$, $1.2k_B T$, $1.5k_B T$, and $1.8k_B T$ at densities fractions 0.5, 0.6, 0.7 and 0.8, respectively. In (b), the free energy gain for edge-edge alignment at packing fraction 0.8 is $2.k_B T$ for triangles, $1.1k_B T$ for square, $0.6k_B T$ for hexagons, and $0.2k_B T$ for dodecagons (b).

shape. An example of this is the (3.12^2) AT, which is comprised of dodecagons and triangles. We find that regular dodecagons easily self assemble into the truncated hexagonal Archimedean tiling at finite pressures without explicit triangle tiles; that is, treating the triangles as pores in the tiling (5.3d). Notably, this assembly is also the infinite pressure crystal for hard dodecagons⁸⁶.

To summarize the results thus far, for each of the four (regular) ATs just discussed, entropy alone is sufficient to obtain the tiling *via* thermodynamic self-assembly. This can be understood as follows. The triangular and square lattice tilings require that its constituents be edge-to-edge. From an entropic standpoint, there are an infinite number of tilings by arbitrarily translating rows or columns of triangles and squares. The self-assembly of edge-edge ATs at finite density implies that there is a free energy difference between aligned and misaligned states. Free energy calculations were performed to quantify the effect of alignment on the free energy. The effect of density and shape were explored (Figures 5.4a,b). For dense fluids of hard triangles (Figure 5.5a,b), there is a free energy difference between the aligned and misaligned state of $1.2k_B T$. Above and near the crystallization packing fraction ($\rho = 0.75$) the free energy difference increases to $2.5k_B T$. The increase in free energy at high packing fraction penalizes misalignments and drives the system to the (3^6) AT. On the other hand, the degree of faceting has an inverse effect on the free energy. As the number of facets increases, a polygon behaves more like a disk. Indeed we observe that the directional entropic forces lose directionality for increased faceting. Directional entropic forces weaken considerably with the number of facets since they arise from a drive toward dense local packing, and the local packing becomes less dense as the number of facets increases⁷⁵. For example, the hard triangle has an entropic penalty of $2.5k_B T$ for misalignment, whereas at the same density the dodecagon has an entropic penalty of only $0.3k_B T$. For the ATs with degenerate ground states, such as the (3^6) and (4^4) ATs, directional entropic forces explain the preferential edge-edge alignment

of the assemblies. They also explain the thermodynamic stability of the (3.12^3) and (6^3) Archimedean tiling at finite packing fractions. As a final note, we observed that the inclusion of attractive patchy interactions does not inhibit the formation of any of these four ATs.

5.4.2 Symmetric Enthalpic interactions

We find that entropy alone is insufficient to assemble the remaining ATs, and enthalpic interactions must be included. In these cases, enthalpy biases the free energy to promote edge-edge binding, and can stabilize open structures that would not be possible with purely entropic forces.

Like the (3.12^3) AT, the (4.8^2) AT can be most easily assembled using only octagons, and treating the square tiles as pores. However, because hard octagons favor a hexagonal crystal structure (5.6a), attraction between nanoplate edges is required to stabilize the AT. The hexagonal crystal structure has misaligned edge-edge bonds with an entropic penalty of $0.5k_B T$ per edge at $\rho \geq 0.8$. The two barriers to entropic self-assembly of the (4.8^2) AT with hard octagons are packing constraints and the coordination of this semi-regular tiling. At $\rho \geq 0.8284$, the (4.8^2) AT cannot self-assemble due to particle overlaps. At lower packing fractions, the free energy penalty for misalignment is $0.2k_B T$. Two-thirds of the edge-edge octagons are 50 misaligned, while the remaining bonds are aligned in the hexagonal crystal structure. The hexagonal crystal structure exhibits a higher coordination (6 nearest neighbor bonds) as compared to the truncated square AT (4 nearest neighbor bonds), which compensates for the entropic penalty due to misalignments. The partial misalignments of the hexagonal crystal structure are entropically favored to the aligned edge-edge bonds of the (4.8^2) Archimedean tiling due to the effect of coordination and packing constraints. In simple terms, the ideal (4.8^2) Archimedean crystalline structure with

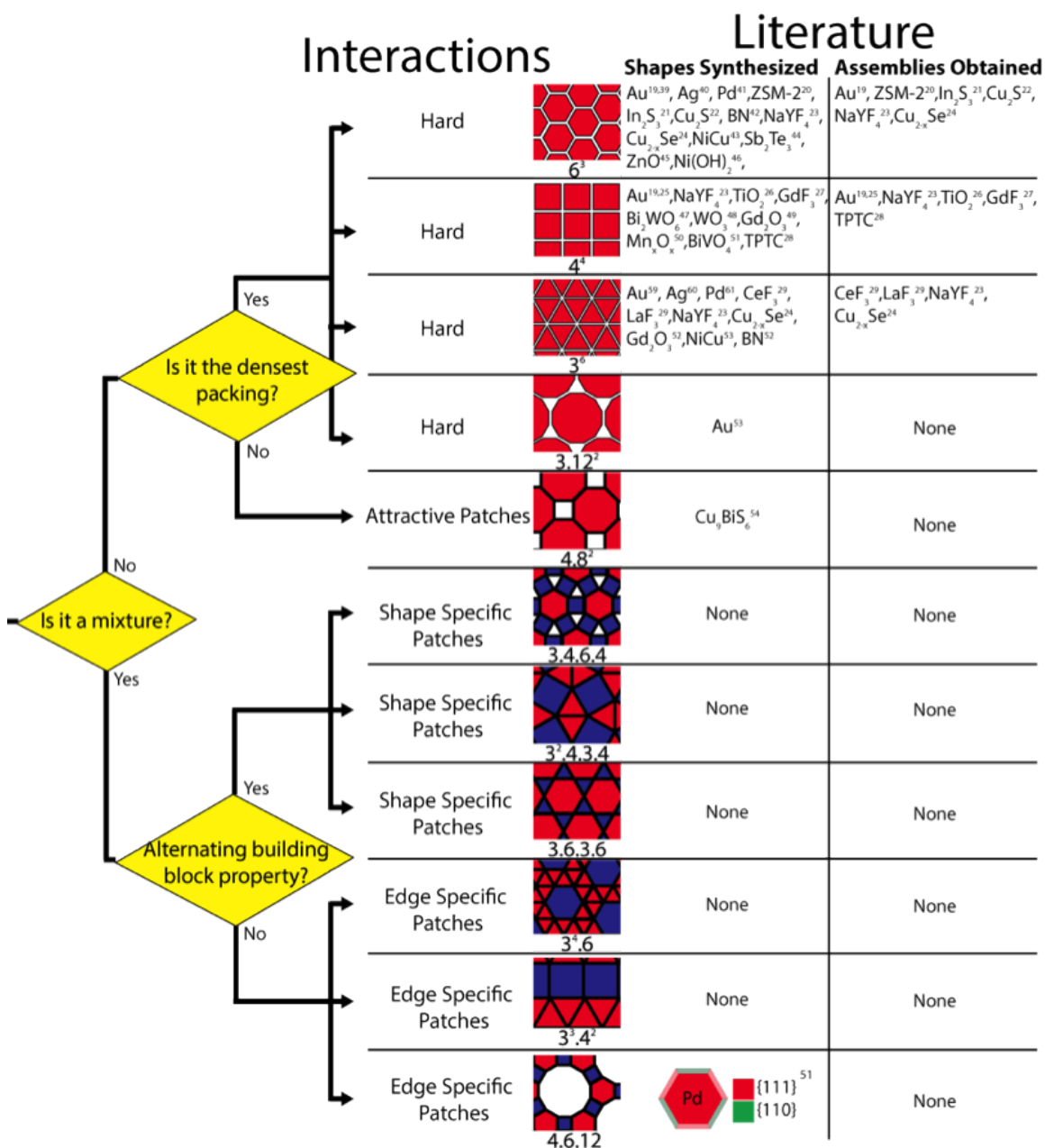


Figure 5.5: Flow diagram representing the design process for the ATs. The paths show how to self-assemble the ATs. Hard interactions are for assemblies that coincide with their densest packings in single component systems. Shape specific patches are for mixtures with lines of alternating building blocks. Mixtures with complex bond networks need edge specific patches. The two rightmost columns show the state-of-the-art in particle synthesis and self-assembly for each corresponding AT.

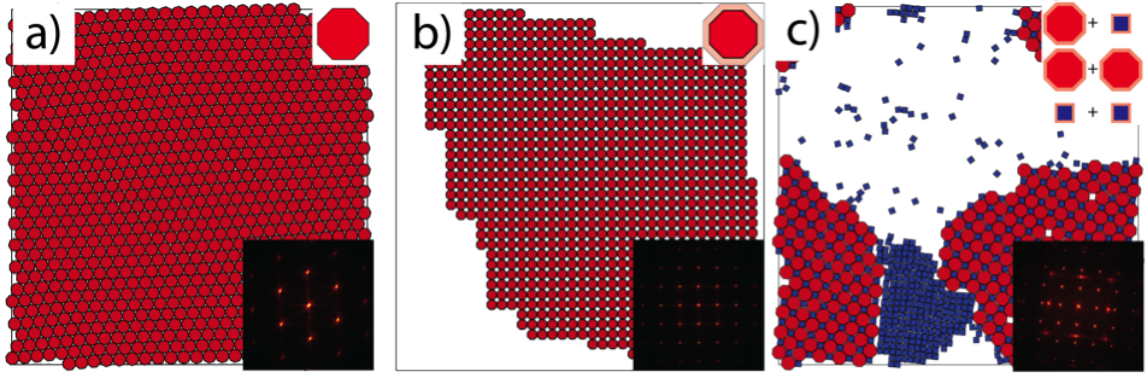


Figure 5.6: Hard *vs.* symmetrically attractive octagons. (a) Hard octagons (upper-right inset) assemble into a hexagonal crystal structure. (b) Symmetrically attractive octagons (upper-right inset) form the defect-free (4.8^2) AT where the squares are treated as pores. Both snapshots are accompanied by a diffraction pattern showing long-range order. (c) Truncated square tiling formed from octagons and squares with symmetric attractive interactions in a 1:2 mixture ratio. Excess squares formed the (4^4) square tiling upon further annealing.

regular octagons has a packing fraction of 0.8284. This value is below the maximum packing fraction of hard regular octagons, which tend to form the hexagonal structure. Consequently, we anticipate attractive interactions are needed to stabilize the (4.8^2) AT. Indeed, by adding short-ranged attractive patches of strength ϵ to each edge of the octagon, we find the (4.8^2) AT robustly self-assembles (Figure 5.6b). Binary mixtures of octagons and squares with attractive patches also form this semi-regular AT (Figure 6c). It is interesting to note that the AT forms without the perfect stoichiometric ratio of tiles. The excess squares form the (4^4) AT. This result is important because experiments will not be constrained by stoichiometry in seeking the (4.8^2) AT (Figure 5.6c).

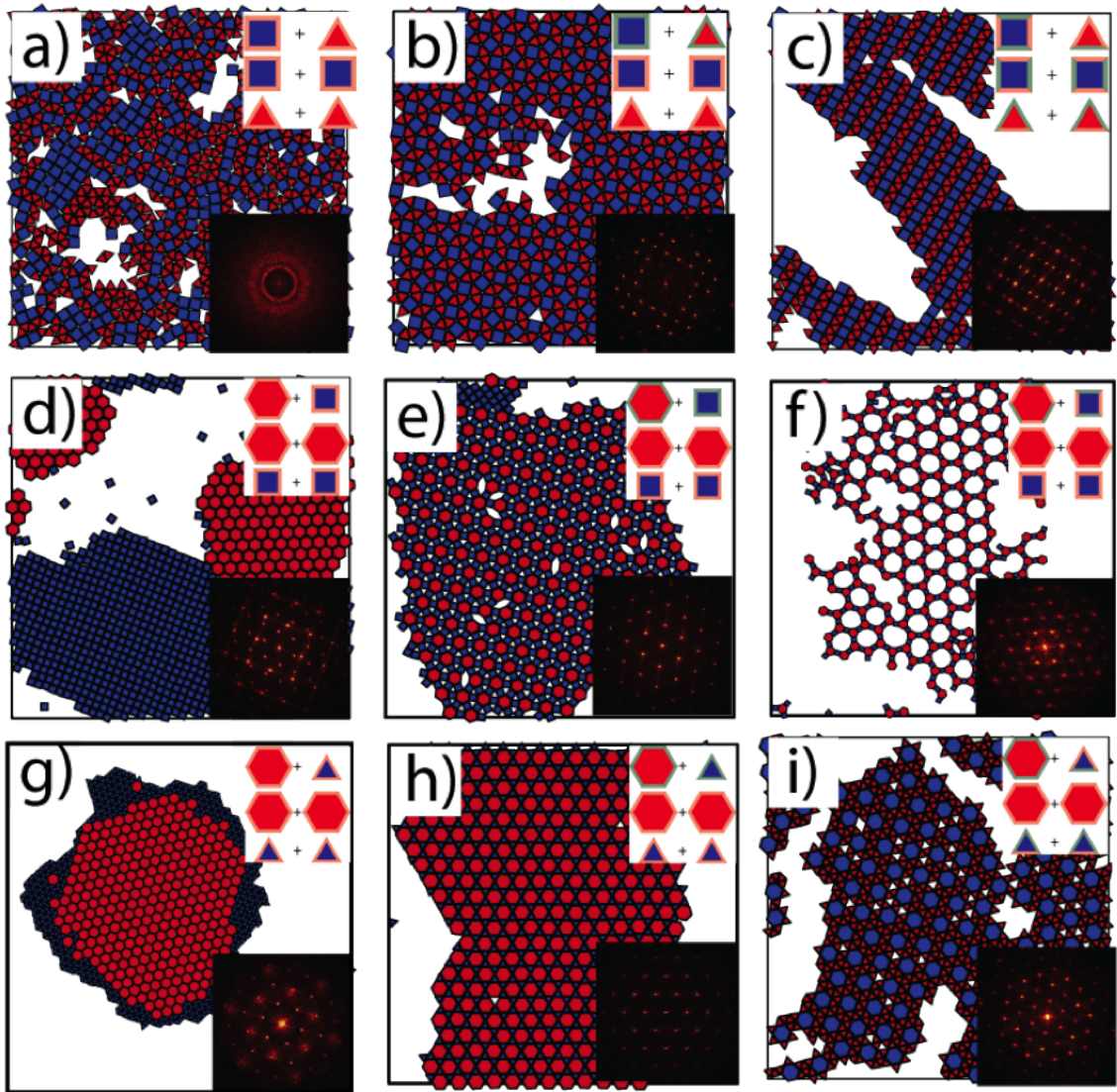


Figure 5.7: Representative snapshots of the design process for the $(3^2.4.3.4)$, $(3.4.6.4)$, $(3.6.3.6)$, $(3^3.4^2)$, $(3^4.6)$, and $(4.6.12)$ ATs. Insets show the design rules and a diffraction pattern. A red halo implies a weakly attractive interaction, while a green halo implies a strong attractive interaction. Left column panels shows symmetrically attractive mixtures of (a) square-triangle, (d) square-hexagon and (g) triangle-hexagon mixtures. Center column panels correspond to the mixtures in the left column with shape-specific patches that readily self-assembles (b) the $(3^2.4.3.4)$, (e) $(3.4.6.4)$, and (h) $(3.6.3.6)$ ATs. Right column panels show shape-specific attractive square-triangle, hexagon-square and hexagon-triangle mixtures that self-assemble the (c) $(3^3.4^2)$ tiling, (f) $(4.6.12)$ and (i) $(3^4.6)$ ATs, respectively.

5.4.3 Shape-Specific Enthalpic interactions

The five ATs studied thus far were each assembled using a single tile shape, even when multiple tiles technically comprise the tiling and one of the tile shapes is considered a pore. The remaining six ATs all require a minimum of two tile shapes. Of these, three - $(3^2.4.3.4)$, $(3.4.6.4)$ and $(3.6.3.6)$ - require shape-specific interactions (Figure 5.7b,e, and h, respectively). As defined previously, shape specificity implies that the interaction between dissimilar rather than similar - species is favored, an asymmetry recently observed in rod-sphere shape alloys¹³⁵.

The two insets of each panel in Figure 5.7 highlight the matching rules between polygons and the corresponding diffraction pattern of the assembly. The matching rules show all combinations of building blocks and the strength of each edge-edge interaction for all interaction pairs. The interaction strength (ϵ) is visualized by the color of the halo around the building block, where red is weak and green is strong. The strength of the strong interaction depends on the targeted AT, as discussed below.

Binary mixtures of symmetric attractive polygons demix or form disordered aggregates. Square-triangle mixtures with symmetric interactions tend to be disordered at intermediate densities because the difference in the free energies of the demixed (pure square and pure triangle) phase *vs.* the mixed phase is small (Figure 5.7a). In contrast, hexagon-square and hexagon-triangle mixtures with symmetric interactions demix at intermediate densities (Figs. 5.7d, g and 5.8). Symmetrically attractive mixtures of regular hexagons and triangles using the stoichiometry of the $(3.6.3.6)$ AT demix and form, as coexisting phases, the (3^6) and (6^3) ATs. Similarly, symmetrically attractive mixtures of the rhombitrihexagonal $(3.4.6.4)$ AT demix into pure hexagonal and square ATs (Figure 5.7c and e). This natural trend to demixing is also observed in mixtures of hard polygons of the same shapes. In the presence of

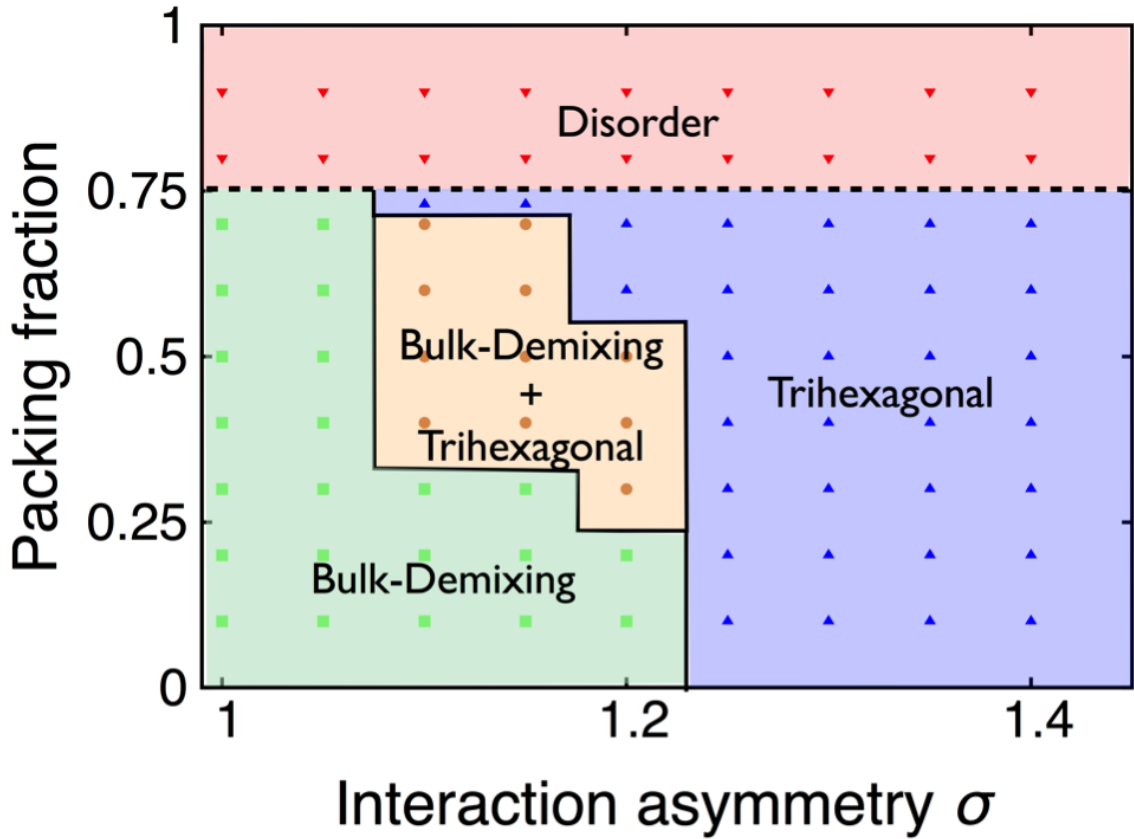


Figure 5.8: Phase diagram of packing fraction *vs.* interaction asymmetry σ for hexagon-triangle mixtures. Symbols represent simulation data points for different asymmetry interaction (shape-specific attraction) and packing fraction values. Each data point represents either the predominantly or always observed phase upon slow annealing (10^7 timesteps) in multiple parallel (five or more) simulations for a given density and interaction asymmetry with systems of 1000 particles.

symmetric attractions, we observe a hierarchy of freezing temperatures. Below but close to the first freezing temperature, the polygons with the most edges crystallize first since these polygons possess more enthalpic bonds (higher crystal coordination), while the less faceted polygons remain in a liquid phase. Further cooling to the second freezing temperature leads to the crystallization of the smaller polygons. As the difference in the number of enthalpic edges of both particles increases, so does the separation between these two freezing temperatures. Thus for square-triangle mixtures the difference is small leading to disorder. For hexagon-triangle and hexagon-square mixtures the difference between melting temperatures increases ($(T_1 - T_2)/T_1 = 2$, where T_1 and T_2 are the first and second freezing temperatures), leading to complete bulk demixing. By biasing the opposite shape interaction (hexagon-triangle, square-triangle, hexagon-square) using shape-specific interactions, the (3².4.3.4), (3.6.3.6), and (3.4.6.4) ATs will self-assemble (Figs. 5.7b,e, and h). The (3.4.6.4) tiling was self-assembled as a binary mixture because the ternary mixture matching rules are more complex. Thus, a pore acts as the triangle tile in this patchy polygon design. The minimum asymmetry σ in the interaction strength to self-assemble the (3².4.3.4), (3.6.3.6), (3.4.6.4) ATs is 1.3ϵ , 1.3ϵ and 1.5ϵ , respectively.

Changing σ affects the phase behavior as shown in Figure 5.8, where we present the phase diagram of hexagon-triangle systems based on ϕ and density. This mixture shows rich phase behavior characterized by the formation of a (bulk) demixed phase, the targeted trihexagonal AT and a coexistence region between these two phases. As previously discussed, symmetric mixtures ($\sigma = 1\epsilon$) demix fully. Small perturbations from symmetric yield the same results. However, for a particular range of interaction asymmetry ($1.1\epsilon < \sigma < 1.25\epsilon$), coexistence between the targeted trihexagonal AT and the completely demixed phase appears for certain densities, indicating the possibility that the trihexagonal AT could be observed at slightly higher densities. Indeed, we observe the trihexagonal AT at packing fractions 0.725. The coexistence



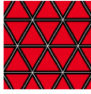

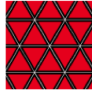

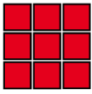
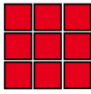

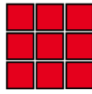


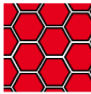

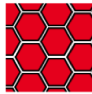




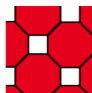




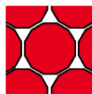












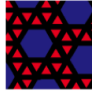
	Hard	Attraction	Shape Specific Patches	Edge Specific Patches
				
				
				
				
				
	Disordered	Disordered		
	Disordered	Demixing  + 		
	Disordered	Demixing  + 		

Figure 5.9: [Simulation results summary. The first column shows the polygons necessary for the assembly of ATs under the design rules proposed. The remaining columns indicate the configurations observed with the different interaction sets.

region is characterized by three successive melting stages upon slow cooling. At high temperature, shapes with more edges (hexagons) crystallize while shapes with lower edges (triangles) form a wetting liquid. Further annealing to lower T leads to the formation of the ATs because they are the ground state at low temperature. Finally, excess triangles excluded from the AT crystallize into the (3^6) AT. Further increase in interaction asymmetry ($\sigma \geq 1.25 \epsilon$) stabilizes the targeted AT at low and high density, implying that shape-specific interactions can overcome the trend towards demixing at intermediate and lower densities (Figure 5.8). At packing fractions ≥ 0.8 , disordered arrangements are formed regardless of interaction asymmetry. Hexagon-square and square-triangle mixtures exhibit a similar rich phase behavior, with the exception that square-triangle mixtures form a single disordered phase instead of (bulk) demixed phases (Figs. 5.7a and 5.9).

5.4.4 Edge-Specific Enthalpic interactions

In the previous section, shape-specific interaction of triangle-square, hexagon-square, and hexagon-triangle shape alloys were shown to self-assemble the $(3^2.4.3.4)$, $(3.4.6.4)$, $(3.6.3.6)$ ATs. The mixtures that self-assemble the $(3^2.4.3.4)$, $(3.4.6.4)$, $(3.6.3.6)$ ATs have similar mixing ratio as the $(3^3.4^2)$, $(3^4.6)$, $(4.6.12)$ ATs. The mixing ratio for the $(3^4.6)$ AT (triangle-to-hexagon 8:1) is greater than that of the $(3.6.3.6)$ tiling. For a triangle-to-hexagon 8:1 mixture ratio, we observe coexistence between the $(3.6.3.6)$ tiling and a triangular tiling formed by excess triangles (Figure 5.9). The demixing observed between excess triangles and the self-assembled $(3.6.3.6)$ AT is similar to that observed between excess squares and the (4.8^2) AT. As shown before, shape-specific interactions for these mixtures self-assemble the $(3^2.4.3.4)$, $(3.4.6.4)$ and $(3.6.3.6)$ ATs (Figure 5.7 b,e and h).

The minimal designs of the $(3.3.4^2)$, $(4.6.12)$ and $(3^4.6)$ AT are shown in Fig-

ure 5.7.c,f and i. In the case of the elongated triangular AT, self-assembly requires strong attraction between opposite edges of the square and one edge of the triangle, and a stronger attraction between the edges that do not attract triangles. The edge pair of the triangles that do not attach preferentially to squares interact strongly. The assembly in Figure 5.7c requires a strong interaction asymmetry of $\sigma = 1.2\epsilon$ (green edges). The design biases energetically the unit cells of the (3^3) AT. The minimal design for the (4.6.12) Archimedean tiling requires strong attraction ($\sigma = 1.25\epsilon$) between alternating edges of hexagon and squares. The remaining edges of both shapes are weakly attractive (inset in Figure 5.7f). Hexagons and squares form rings, which is consistent with the truncated hexagonal AT. The assembly is not free of defects, and in some cases single or multiple polygons are encircled by these rings (Figure 5.7f). In the minimal design for the ($3^4.6$) Archimedean tiling, all edges of the hexagon preferentially attach to one specific edge on the triangles, the hexagon-to-hexagon edge attraction is weak ($\sigma = 1\epsilon$), and triangles preferentially attach to each other on edges that do not preferentially attract hexagon edges (Figure 5.7i). By making the hexagon preferentially attractive to one side of the triangle, all edges of the hexagon become saturated and the triangle-triangle interaction completes the tiling. For the assembly in Figure 5.7f, the interaction asymmetry σ is 3ϵ . Due to the complexity of this set of design rules, multiple point defects are observed. This AT is chiral, however no bias towards either handedness was observed. Thus, to form the snub hexagonal AT with a targeted chirality, further complexity in polygon patchiness is needed.

5.5 Discussion

We approached the design of nanoplates to assemble the Archimedean tilings by ascertaining the simplest set of interactions yielding the desired tiling. The multistep design process summarized on the left-hand side in Figure 4 uses information about

the target tiling and building block. We first minimize the number of building blocks to self-assemble the targeted tiling. For the (3.12^2) , (4.8^2) , $(3.4.6.4)$ and $(4.6.12)$ AT, one of the polygonal tiles is replaced by a pore, and the resulting tiling no longer fills space, but is instead open and porous.

After selecting the building blocks, the design process examined the constituent polygonal building blocks, and alters the interaction complexity by changing the specificity of interactions. The four models ranked in terms of specificity are hard, symmetric patches, shape-specific patches and edge-specific patches. Our design process reveals why for each AT a certain degree of specificity is needed for self-assembly. Initially, we test if entropic interactions are sufficient to self-assemble each crystalline structure. If the infinite pressure ground state is not the candidate crystal structure, we find attractive interactions are needed to self-assemble the crystalline structure (Figure 5.5). Due to the highly symmetric polygons used to self-assemble the ATs, we argue that an effective entropic edge-edge interaction will stabilize these highly symmetric ground states. For crystal structures with one building block that are not the infinite pressure ground state, symmetric attractive patches are sufficient for assembly (Figure 5.5). For mixtures of building blocks, the complexity of the crystal structure determines the complexity of the interaction potential. Hard (entropic) mixtures show a natural trend to partial demixing and do not form crystalline monolayers with discrete symmetries. Symmetric attractive mixtures also demix, with no indicative behavior towards the formation of binary ATs at intermediate densities. We posit that the hard mixtures segregate due to a depletion effect¹³⁸. Since hard and symmetrically attractive building blocks demix, selective patchiness must be used to overcome this natural trend (Figure 5.7). The local environment for each polygonal tile in the target AT determines the arrangement of patches. If an alternating building block crystal structure is present, shape specific patches are sufficient to design the crystalline structure (Figure 5.7). An alternate building block structure is a binary mixture

in which the large polygonal tile is surrounded by the small tile, and the small tile has at most one bond with another small tile. If the crystalline structure for a mixture of building blocks does not contain the alternating building block property, it is necessary to use edge specific interactions. The assembly complexity of the building block and crystal structure provides the necessary information to self-assemble the AT.

The description of minimal design rules for self-assembly is related to tiling models in computer science and mathematical descriptions of graph connectivity. The general complexity of edge connectivity problems is known to be NP hard¹³⁹, which weakens the attractiveness of an algorithmic approach to the development of design rules for crystal structures. Mathematical work on the edge coloring of Archimedean graphs¹⁴⁰ does not provide sufficient information to develop design rules for self-assembly. In effect, an iterative, heuristic approach as described in this paper is the best one can do to develop design rules for self-assembly of tilings such as these.

5.6 Conclusion

Ascertaining assembly complexity is an essential feature of our design strategy for mixtures of anisotropic patchy particles. We ranked each AT from (3⁶) to the (4.6.12) in order of assembly complexity. Self-assembly complexity is the complexity of the simplest set of interactions and building blocks that self-assemble the candidate crystal structure with a minimal number of crystallographic defects (Figure 5.6). We described the design strategy in a flow diagram shown in Figure 5.5. The flow diagram describes the steps used to design the interactions of the building blocks. To the right of the design flow diagram, we overview material systems^{49,62,78,79,141–152} that can form the anisotropic nanoplates consistent with the ATs, and material systems that

self-assemble^{1,5-7,23,40,48,55,127-129} ATs with nanoplates (Figure 5.1). The entropically stabilized (3^6) , (4^4) , (6^3) ATs have been observed experimentally with polygonal tiles, but the other Archimedean tilings remain elusive (Figures 5.1 and 5.5). To assemble these elusive ATs, nanoplates can be covered with DNA^{30,153}. DNA functionalized tiles provide a means of achieving the necessary interaction specificity to assemble ATs. Also, we note that nanoplates with different crystallographic edges can act as effective patchy particles⁷⁶. We propose that edge-specific nanoparticle patches can be synthesized by exploiting the different attractive energies of the crystallographic facets⁷⁶.

The building block design process offers insight into the necessary conditions to self-assemble crystals with regular polygons (nanoplates). The design process has led to important conclusions about shape and self-assembly, summarized in Figure 5.9. With only entropy, certain Archimedean tilings can self-assemble their infinite pressure packings at intermediate packing fractions. This finding reinforces the perspective on an entropic patch as a driver for self-assembly⁷⁵. On the other hand, for low density packings symmetric enthalpic patches are required. Binary mixtures of regular shapes have a rich behavior that depends on the type of interactions and geometry. We observe that hard binary mixtures tend to be disordered when mixed. By adding enthalpic patches, demixing occurs if the difference between the coordination of the polygons is large. This is confirmed by the observed demixing of hexagon-square and hexagon-triangle assemblies, whereas square-triangle mixtures are disordered. Shape-specific and edge-specific patches stabilize the remaining semi-regular tilings. Although nanoplate patterning inspires the designs developed in this work, these enthalpic design rules can also be expanded to supramolecular systems, where particle interactions are programmable and system dynamics are faster.

CHAPTER VI

Shape alloys of nanorods and nanospheres from self-assembly

The results of this chapter were published in:

X. Ye, J.A. Millan, M. Engel, J. Chen, B. Diroll, S.C.G. Glotzer, C.B. Murray, Shape alloys of nanorods and nanospheres from self-assembly, Nano Letters, 13 (10), pp 4980-4988, September 2013

6.1 Abstract

Mixtures of anisotropic nanocrystals promise a great diversity of superlattices and phase behaviors beyond those of single-component systems. However, obtaining a colloidal shape alloy in which two different shapes are thermodynamically co-assembled into a crystalline superlattice has remained a challenge. Here we present a joint experimental-computational investigation of two geometrically ubiquitous nanocrystalline building blocks—nanorods and nanospheres—that overcome their natural entropic tendency towards macroscopic phase separation and co-assemble into three intriguing phases over centimeter scales, including an AB_2 -type binary superlattice. Monte

Carlo simulations reveal that although this shape alloy is entropically stable at high packing fraction, demixing is favored at experimental densities. Simulations with short-ranged attractive interactions demonstrate that the alloy is stabilized by interactions induced by ligand stabilizers and/or depletion effects. An asymmetry in the relative interaction strength between rods and spheres improves the robustness of the self-assembly process.

6.2 Introduction

Colloidal mixtures of differently sized and shaped nanocrystals (NCs) not only serve as model systems for studying a variety of processes in condensed matter, but also provide a bottom-up approach for the chemical design of NC-based metamaterials with emergent properties. The majority of existing works on self-assembly of colloidal NCs into ordered superlattices focuses on single- and multi-component spherical NCs (nanospheres, NSs)^{23,26,38,39,154} as well as single-component nonspherical NCs^{5,10,15,36,37,68,76,155}. In contrast, assemblies of mixtures of distinct shapes has remained largely unexplored and are only beginning to be investigated^{26,156–159}. A simple deviation from the spherical shape is found in cylindrical nanorods (NRs), for which an extensive library of compositions exists through recent advances in NC synthesis^{103,155,160–162}. NRs have been co-assembled together with NSs into planar structures. Sanchez-Iglesias and coworkers¹⁴ used Au nanowires as colloidal templates for the oriented assembly of Au NSs as well as short Au NRs. Nagaoka et al.¹⁶ also explored the binary assembly of CdSe/CdS NRs and Au NSs. However, the spatial extent of ordering has been limited to submicron-sized areas, and to two dimensions. The mixture of rods and spheres is a well-studied model system for colloidal matter exhibiting rich and complex phase behaviors^{14,163–167,167–171}. In most of these works, rods are used to model rigid polymers. As a result, rods have often

been approximated to be thin^{14,163–165,167,171}, non-interacting^{166,168,169,171}, and parallel^{164,166}. In a seminal report of binary mixtures of rod-like fd viruses (6.6 nm diameter, 880 nm contour length) and polystyrene latex spheres (diameter ranging from 22 nm to 1 μm), Adam et al.^{14,165} demonstrated that depending on the experimental conditions, both macroscopic (bulk) demixing and microscopic phase separation can occur. The authors observed several intriguing micro-segregated structures including the columnar and lamellar phases, which they conclude were entropically stabilized. First reported in a theoretical study of hard particles¹⁶⁴, the lamellar phase consists of smectic layers of parallel rods alternating with thin layers of spheres. It is also known from simulation studies that assembly of the lamellar phase can be difficult because it competes with bulk demixing¹⁶⁷. In colloidal systems, excluded-volume effects are often accompanied by enthalpic interactions that can introduce further complexity into the phase diagram. For example, simulations of hard Gaussian overlap rods and hard spheres result in macrophase separation¹⁶⁹, but Gay-Berne rods and Lennard-Jones spheres can exhibit a lamellar (smectic) phase for strong rod-sphere interaction at a high 70:30 rod-sphere number ratio¹⁷⁰. Diversity in phase behavior resulting from the interplay between shape and interaction anisotropy has also been observed at the nanoscale, where certain exotic phases are not accessible by excluded-volume effects alone^{36,37,68,76,172}. In real NC systems, it is usually nontrivial to quantify the strength and distance dependence of nanoscale forces, most of which cannot be measured directly. Moreover, various interactions can compete, including van der Waals, electrostatic, magnetic, molecular surface, and depletion effects³¹. However, in the absence of electrostatic (including electric dipole interactions) and magnetic forces, the particle geometry often dominates³² and self-assembly of binary superlattices is challenging¹⁷³. Interactions can then be considered as a perturbation^{10,36,37,76,174}.

In the present work, we report the self-assembly of colloidal NRs and NSs into highly ordered three-dimensional (3D) binary nanocrystal superlattices. Using a wide

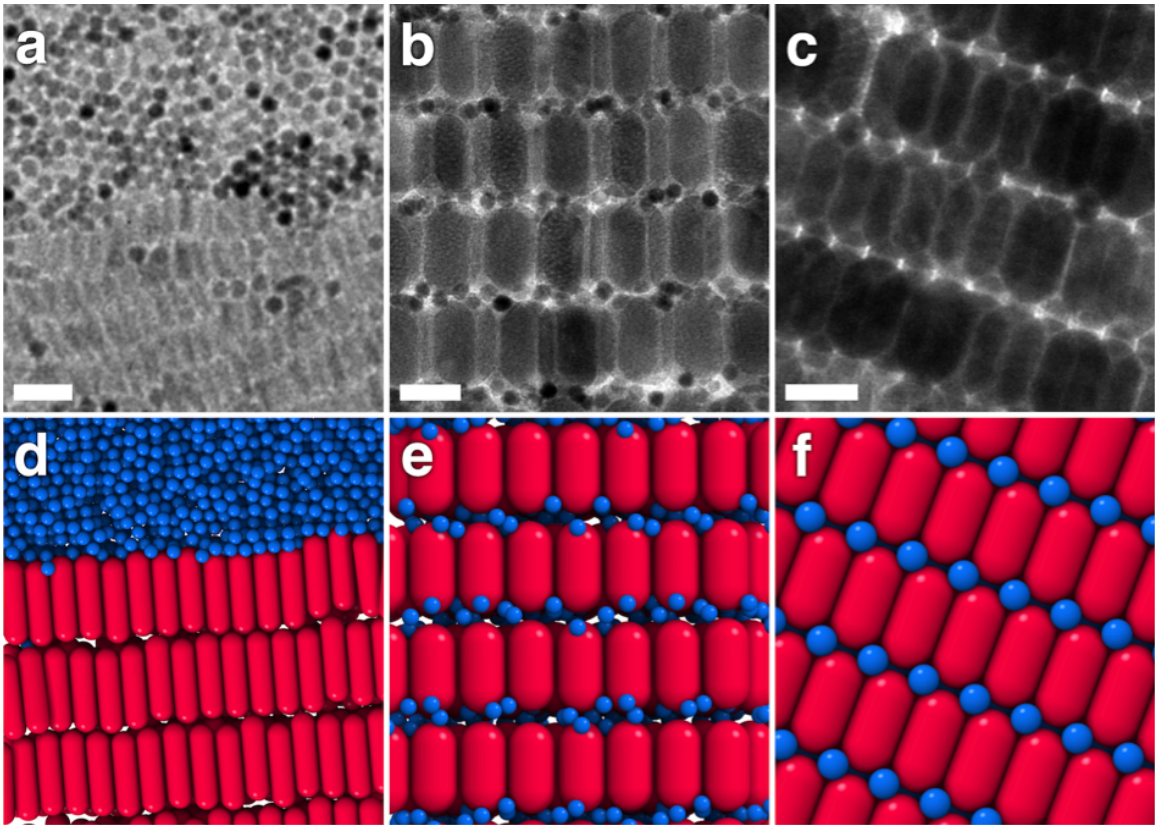


Figure 6.1: Self-assembled superlattices of NSs and NRs. Depending on the aspect ratio of the rods and the size ratio of the rods to the spheres, we observe three different phases: (a,d) bulk demixing, (b,e) the lamellar phase with disordered (mobile) spheres, and (c,f) the AB_2 BNSA with full positional order. TEM images (a-c) are accompanied by theoretical reconstructions (d-f). Scale bars: (a) 25 nm, (b,c) 50 nm.

range of rod-sphere combinations, we demonstrate that both macro- and micro-phase-separated binary phases can be formed over extended areas (centimeter scale) with individual grains approaching 100 m². Electron microscopy observations and analyses allow the identification of bulk demixing (Fig. Fig. 6.1a,d) and two binary nanocrystal shape alloys (BNSAs), the lamellar phase (Fig. 6.1b,e) and the AB₂ BNSA (Fig. 6.1c,f). We further reproduce and analyze the assembly of rod-sphere binary systems in Monte Carlo (MC) simulations by extensively exploring the parameter space spanning particle shape and strength of interparticle interactions. Our simulations show that short-ranged attractions play a key role in helping the shapes to overcome their entropic tendency towards demixing by facilitating and stabilizing the AB₂ BNSA.

6.3 Numerical and analytical approach

6.3.1 Determination of densest spherocylinder-sphere packings

We construct the ideal unit cells for binary crystals and demixed phases. Lattice distortions are considered for the AB₂ unit cell to maximize packing fraction. The packing fraction of a demixed phase is calculated as :

$$\phi_D = (V_R + 2V_S)/(V_R\phi_R^{-1} + 2V_S\phi_S^{-1})$$

Here, V_R , V_S , ϕ_R , ϕ_S correspond to the volume and maximum packing fraction of rods (stretched FCC) and spheres (FCC), respectively.

6.3.2 Numerical method

Particles are represented as cylindrical rods with spherical caps, with and without an added short-range interaction. Overlap checks are performed as in Ref. (15) generalized to caps with arbitrary curvature. Particles interact *via* a tabulated attractive force (see below) in addition to hard-core repulsion. In self-assembly runs, pressure is slowly reduced until crystallization occurs. Isotensile melting simulations are performed at constant density starting from a constructed crystal. In the presence of interactions, pressure and temperature are kept fixed until ordering occurs. System sizes range from 576 to 4032 particles. Simulation times are several tens of millions of Monte Carlo cycles using established simulation codes.^{8,9} Free energy calculations employ thermodynamic integration from an Einstein crystal as described in Ref. (76).

6.3.3 Interaction model

We define the potential energy between two particles P_1 and P_2 in the form of a contact interaction as the four-dimensional integral over the surface areas Ω_1 and Ω_2 of the particles:

$$E_{P_1, P_2} = \iint_D U(|r_1 - r_2|) dA_1 dA_2.$$

Here, $U(r)$ is the free energy contribution of two surface area elements dA_1 and dA_2 at the positions r_1 and r_2 . As a short-range, isotropic interaction of the surface-elements (interaction kernel) we use a square well potential with interaction cut-off distance 0.2σ , comparable to the size of the oleic acid molecule ligands:

$$U(r) = \begin{cases} 1, & \text{for } r \leq 0.2\sigma. \\ 0, & \text{for } r > 0.2\sigma. \end{cases} \quad (6.1)$$

This is a simple Ansatz, but it is sufficient to quantify the amount of pairwise contact. We solve the surface integral using numerical Monte Carlo integration and tabulate the potential using a 1D, 2D, and 4D parameterization for the three cases sphere-sphere (E_{SS}), rod-sphere (E_{RS}), and rod-rod (E_{RR}), respectively, to obtain $E_{SS}(d)$ (d), $E_{RS}(d, h_1)$, and $E_{RR}(d, h_1, h_2, \theta)$. As energy unit we use $E_{SS} = E_{SS}(0)$. 100,000 points on the surface of each particle are enough to obtain smoothly varying potentials with the numerical integration. For further details see Figure 6.2; the potentials are shown in Figure 6.3.

6.4 Results

The self-assembly process and the relative phase stability are analyzed in four steps by gradually increasing the sophistication of the theoretical model. First, we approximate the NCs as hard (athermal) shapes and search for their densest packings following the procedure described previously³⁴. The results obtained from this calculation are relevant at high NC concentration as present during the final stages of the experiment. Next, we perform MC simulations with hard particles to resolve the phase behavior at lower density¹⁵. These simulations converge to the state with highest entropy. In a third step, we introduce short-range interactions between the NCs. We assume interactions proportional to the surface areas in contact. Finally, we consider an asymmetry in the relative interaction strengths between rods and spheres, as expected for chemically distinct NCs or crystallographically distinct NC facets^{76,158}. The rod shape is chosen as a cylinder with two spherical caps. The cir-

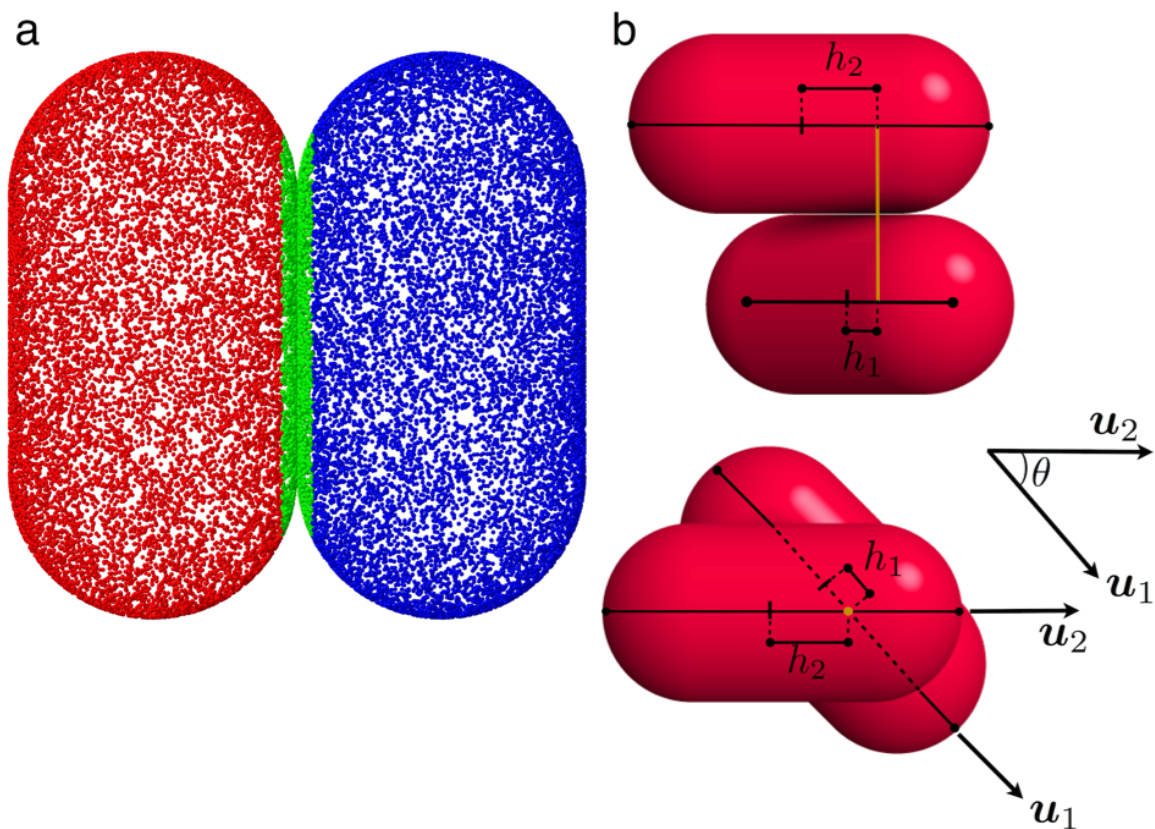


Figure 6.2: Geometric parameters for the interaction model. (a) We calculate the interaction of two NCs by MC integration over the surface areas. Here, two spherocylinders ($AR = 1.97$) are arranged parallel side-by-side. Randomly distributed points on the surface of both spherocylinders (blue and red points) represent the surface elements of the spherocylinders. Points close enough to interact are colored green. (b) We parameterize the relative arrangement of two spherocylinders by the surface-to-surface distance of closest approach, d , (not shown), the projections of the closest points onto the long axis, h_1 and h_2 , and the angle θ between the particle directors u_1 and u_2 .

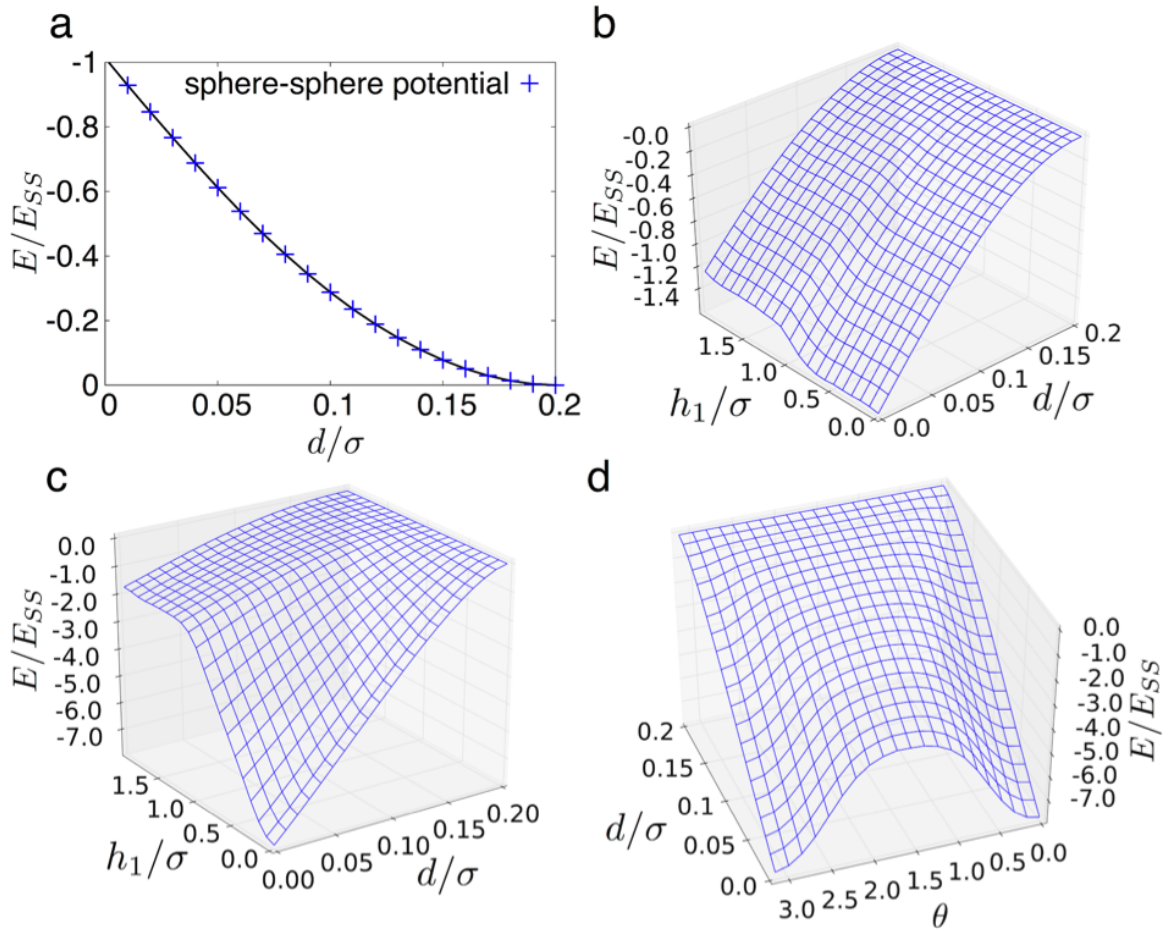


Figure 6.3: Plots of the tabulated interaction potentials for spherocylinders with aspect ratio $AR=1.97$ and using the interaction kernel described in Methods. (a) Sphere-sphere potential. (b) Spherocylinder-sphere potential. (c,d) Spherocylinder-spherocylinder potential. For the spherocylinder-spherocylinder potential, we show as examples of two different cuts through the 4D parameter space. In (c), spherocylinders are kept parallel, $\theta = 0$, and we set $h_1 = h_2$. In (d), we keep the spherocylinder in contact at their midpoints ($h_1 = h_2 = 0$) and vary their separation and relative orientation. We use the parameterization for the relative arrangement of two spherocylinders specified in Figure 6.2. The relative arrangement of a sphere relative to a spherocylinder is described by a restriction of this parameterization.

cular cross-section of the cylinder approximates the cross-section of the NRs, which is a valid approximation because the NR edges are effectively rounded (softened) by the presence of the ligand shell. Furthermore, the cylinder cross-section does not influence the relative phase stability significantly, because the contact between neighboring rods is identical for all configurations competing for stability. We characterize the rod shape by three dimensionless parameters: the aspect ratio $AR=L/2\sigma$, the rod-sphere size ratio $\gamma= D/2\sigma$, and the curvature of the caps $\kappa = \sigma/R$. Here, L is the tip-to-tip length, σ the cylinder radius, κ the radius of curvature of the rod cap, and D the sphere diameter. The spherocylinder shape is obtained for $\gamma = 1$. In the following, we choose a 2:1 mixture of spheres and rods.

6.5 Densest rod-sphere packings

In the limit of high density, NCs adopt configurations that maximize packing fraction. Starting from the known densest binary sphere packings¹⁷⁵, we construct analogue binary spherocylinder-sphere packings by elongating the bigger sphere. Finding the densest packing is simple when the big spheres form hexagonal layers and are in contact. In this case, provided phase separation does not occur, the optimality of a packing in the binary sphere system guarantees the optimality of an analogue packing in the spherocylinder-sphere system. For $AR = 1.97$ (NaYF₄ NRs) and size ratios close to $\gamma = 0.55$, we find the densest packing is indeed realized in the AB₂ BNSA (Fig. 6.4a). As the size ratio decreases (Fig. 6.4b), spherocylinder caps in neighboring layers touch for $\gamma \leq 0.528$, limiting the packing efficiency. In contrast, towards higher size ratio, $0.577 \approx 1/\sqrt{3} \leq \gamma \leq 0.6247$, neighboring spheres touch, forcing the lattice to expand laterally in-plane, until for $\gamma > 0.6247$ a buckled honeycomb lattice with spherocylinders in contact packs more efficiently ?? (Fig. 6.5). In both cases, the packing density is lowered, crossing the value for demixing. Strikingly, the ex-

perimental size ratio $\gamma = 0.57$ for the AB_2 BNSA falls within in the region where bulk demixing is disfavored. In agreement with experiment demixing becomes more favorable with decreasing curvature of the caps (Fig. 6.6a,b). Lattice shear, which is sometimes observed as an intermediate state during assembly simulations in the presence of interactions (see later in Fig. 6.10d), also does not increase the packing fraction (Fig. 6.6c,d). For the remainder of the paper we fix $\kappa = 1$ and $\gamma = 0.57$.

6.6 Monte Carlo simulations of the hard spherocylinder-sphere system

We investigate the entropic stabilization of the AB_2 BNSA with isobaric (NPT) MC simulations. Simulations are initialized from a disordered fluid in an attempt to spontaneously crystallize the system. Pressure is gradually increased following a protocol that was successful for many systems of hard particles³⁴. Yet, co-assembly is never observed with the experimental $AR = 1.97$ (Fig. 6.7a). To enhance the entropic interactions between the spherocylinders at the same pressure, we increase the aspect ratio to $AR=2.97$. Although spherocylinders now show a stronger preference for local alignment (Fig. 6.7b), global order is still not observed on the time scale of our simulations. This inability to assemble the experimentally-observed structure indicates that either the nucleation times are longer than those accessed on (long) simulation, or that additional interactions must be included. To distinguish between those two possibilities, we examine the thermodynamic stability of the AB_2 BNSA by performing isochoric (NVT) melting simulations ($AR = 1.97$) starting from the densest packing structure. We observe melting in two steps. At packing fraction 68, the separation of spherocylinder layers increases abruptly. Spheres diffuse almost freely between adjacent layers as found in the lamellar phase (Fig. 6.4c). Finally, at packing fraction

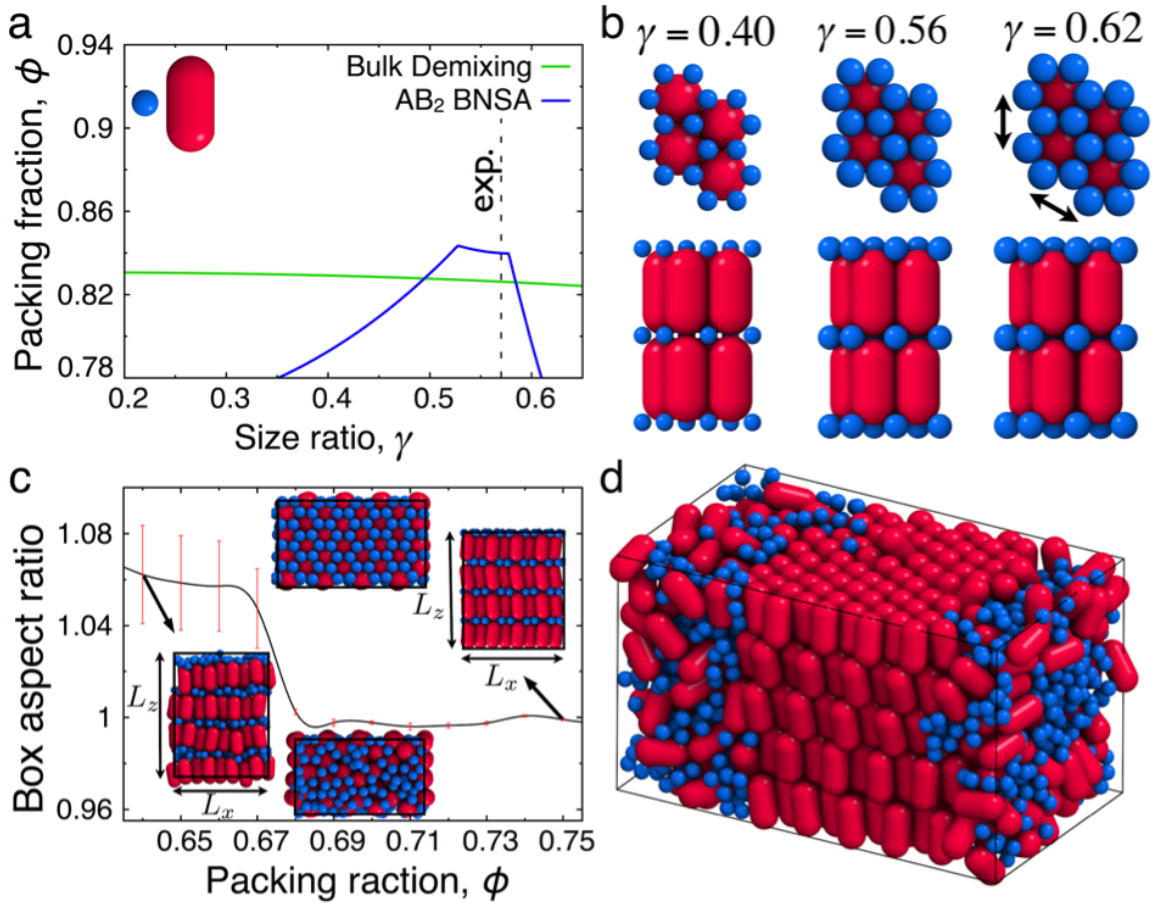


Figure 6.4: Densities and MC simulations of hard spheres and hard spherocylinders (AR=1.97). (a) Comparison of the packing fractions for the AB₂ BNSA and for bulk demixing. The AB₂ BNSA is the densest packing close to size ratio $\gamma = 0.56$. (b) Towards lower ($\gamma = 0.40$) and higher ($\gamma = 0.62$) size ratios, the spherocylinders caps or the spheres, respectively, touch. This introduces additional packing constraints and reduces the packing efficiency. (c) Isotensile MC simulations started from the AB₂ BNSA show a rapid change in the box aspect ratio L_z/L_x indicative of a transition to the lamellar phase at packing fraction $\phi = 0.68$. (d) At $\phi = 0.618$, the lamellar phase separates into the rod crystal and a mixed fluid.

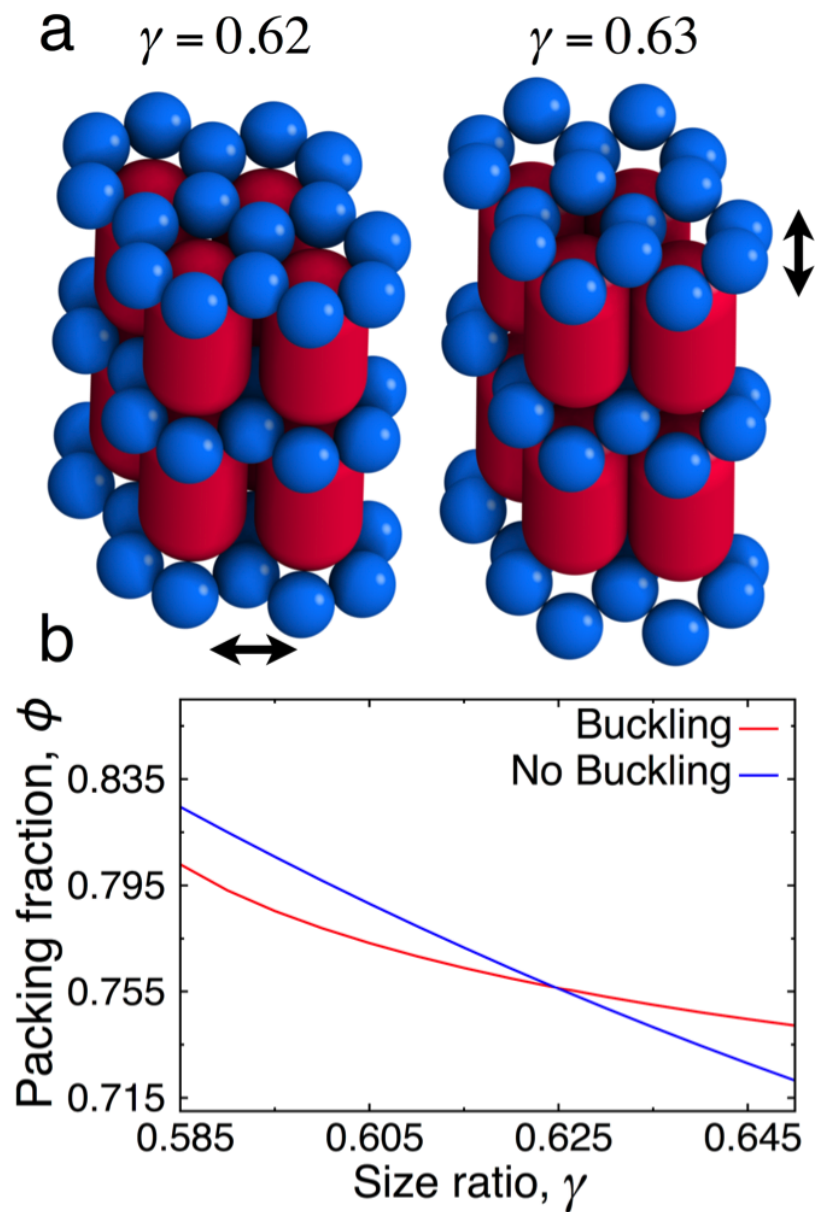


Figure 6.5: Densest packings with buckled interlayers. (a) Unit cells of the AB_2 BNSA with flat (non-buckled) sphere interlayers at size ratio $\gamma = 0.62$ and with buckled sphere interlayers at $\gamma = 0.63$. (b) Comparison of the packing fractions with and without buckling showing a crossover at $\gamma = 0.6247$. However, for the γ -range shown in the figure, neither arrangement packs as densely as the completely demixed bulk phase.

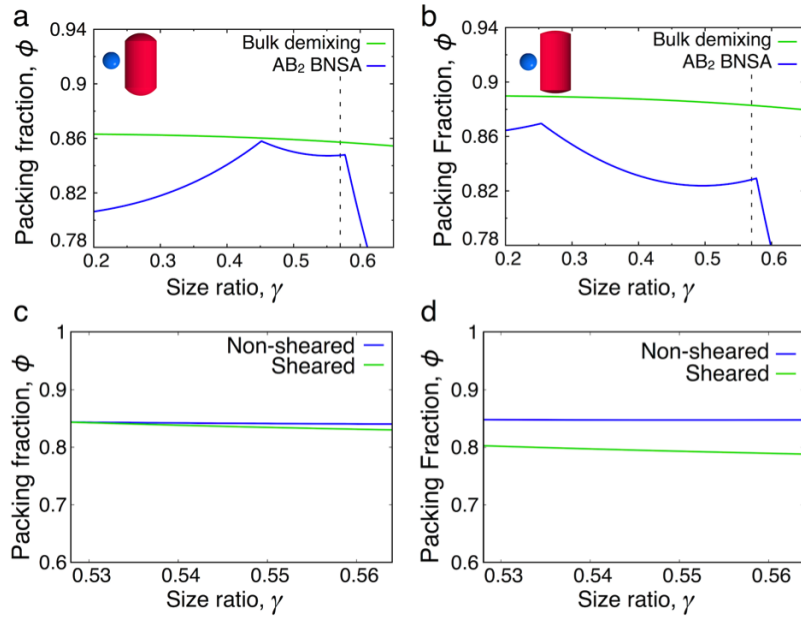


Figure 6.6: Densest packing fractions for spheres and rods with curvatures of the caps $\kappa=0.8$. (a), and $\kappa=0.4$ (b). As the curvature is reduced, the packing fraction of the demixed phase increases faster than that of the AB₂ BNSA. (c,d) Comparison between sheared and non-sheared AB₂ BNSA for $\kappa=1.0$ (c) and $\kappa=0.8$ (d). We shear in direction [100] until the rod caps of contiguous rod-stacks touch.

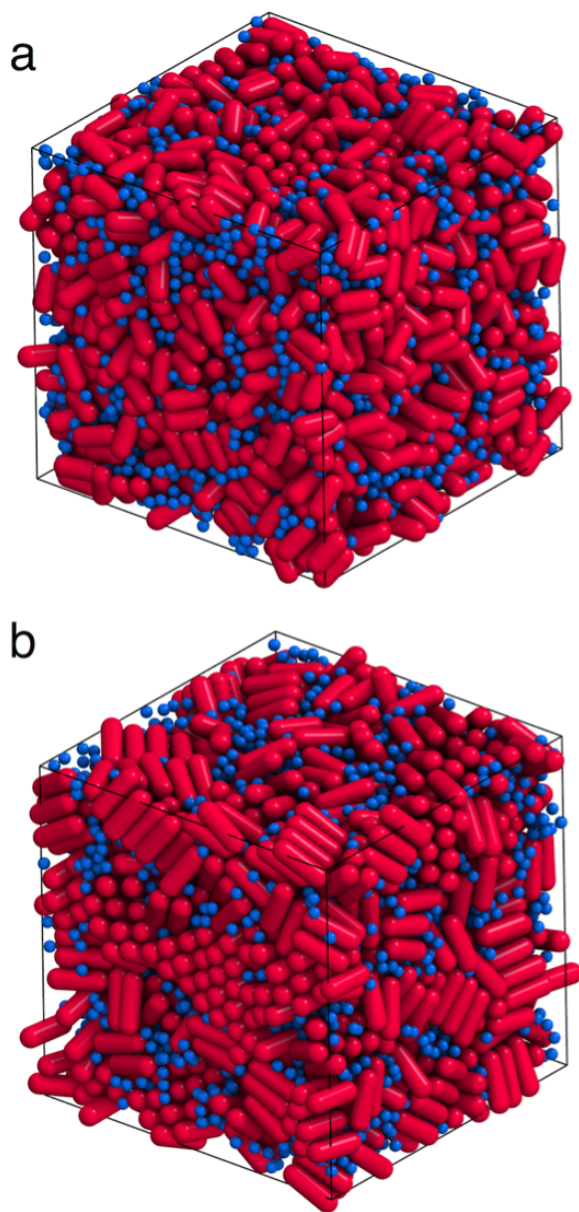


Figure 6.7: Simulation snapshots of hard spherocylinder-hard sphere mixtures for aspect ratios equal to 1.97 (a) and 2.97 (b). In (a), no global order is observed (nor expected) due to the low aspect ratio. In (b), spherocylinders with higher aspect ratio form monolayers and (smectic) multi-layers, but the order is highly defective. The spheres are mostly separated and demonstrate no clear intention to form sphere-populated interlayers.

$= 0.63$, spheres completely abandon the interstitial sites. Phase separation into a fluid sphere phase and a smectic spherocylinder phase occurs (Fig. 6.4d). Two-step melting is also observed for spherocylinders of $AR = 2.97$. Free energy calculations confirm the stability of the AB_2 BNSA at high packing fractions. We conclude that the co-assembly of rods and spheres into AB_2 BNSA is difficult if not impossible with entropic interactions alone; it is kinetically inhibited and competes with macroscopic phase separation.

6.6.1 Short-range attractive interactions

A close inspection of the TEM images reveals configurations that are not possible with entropic interactions alone. These configurations are evidence for the presence of additional enthalpic, attractive interactions during assembly. The following observations cannot be explained with hard particles: (i) Assembly of monodisperse NRs with a short aspect ratio. Entropic interactions typically require a higher aspect ratio⁴⁶. (ii) Alignment of NRs at low packing fraction. (iii) Single layers of NRs that are only loosely coupled to one another. (iv) Stripes or filament-like assemblies (Fig. 6.8). The formation of single layers and stripes suggests an anisotropic crystal growth with a higher growth speed within the layers. Since the $NaYF_4$ NRs and the NSs employed in this work do not have appreciable electrostatic charges or dipole moments^{76,154}, interparticle interactions are expected to be short-ranged. Candidates are van der Waals interactions of ligand shells or depletion effects. We do not make an attempt to derive an interaction potential rigorously, but merely derive it based on two simple assumptions: the force is proportional to the contact area and the interaction is short ranged. We thus hypothesize that the interaction can be modeled by a contact force. These are reasonable assumptions both for depletion and for NCs uniformly covered with ligands (Fig. 6.9a)

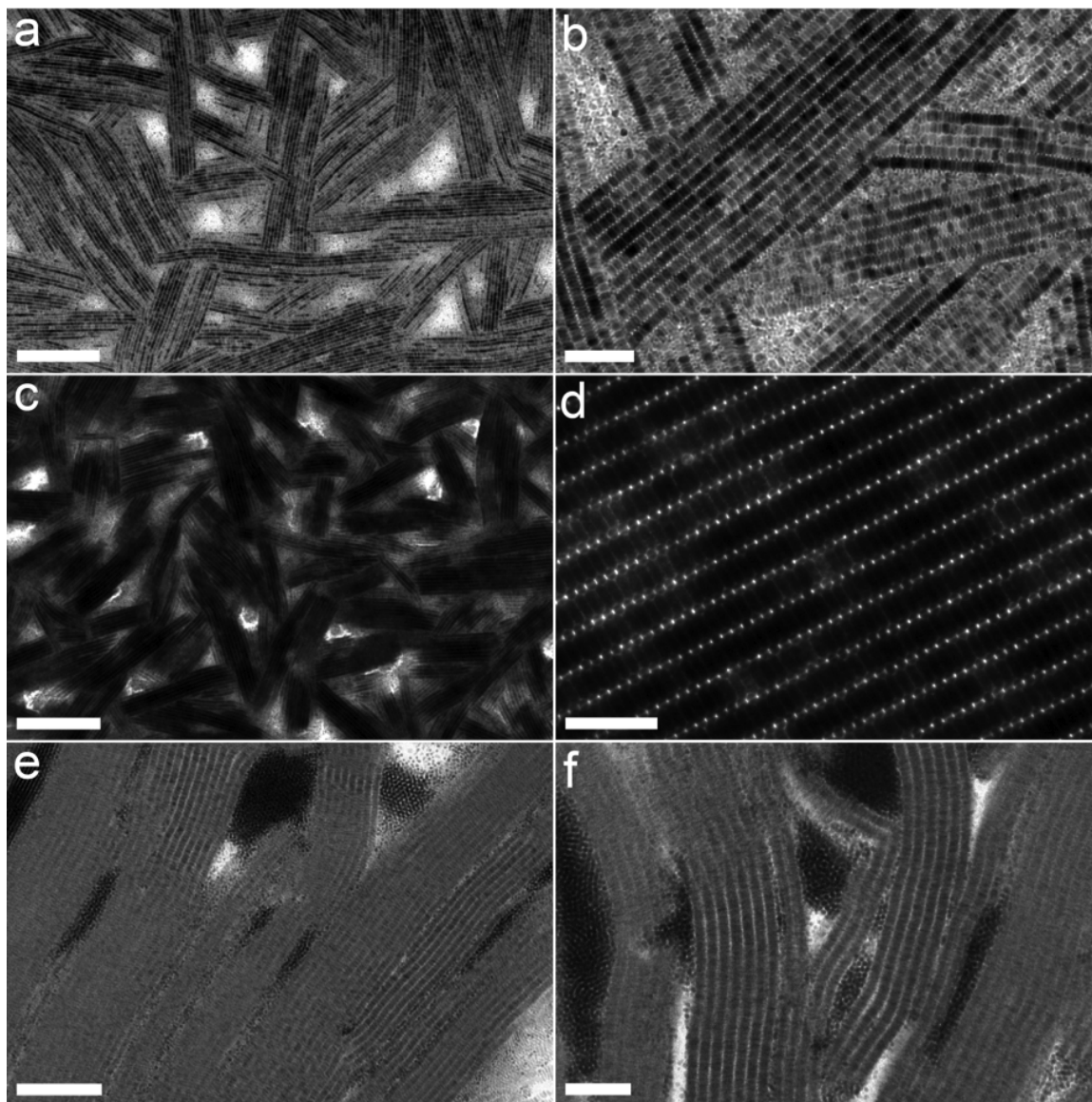


Figure 6.8: (a-d) TEM images of rod-sphere BNSAs self-assembled from NaYF₄ NRs and 11.0 nm Fe₃O₄ NSs. The samples shown in (a) and (b) are formed with a higher total NC concentration in the spreading solution compared to those shown in (c) and (d). (e,f) TEM images of structures self-assembled from CdSe NRs and 5.5 nm Au NSs. The system shows bulk phase separation instead of rod-sphere BNSA formation. Scale bars: (a) 1 μm , (b) 200 nm, (c) 1 μm , (d) 100 nm, (e) 200 nm, (f) 100 nm.

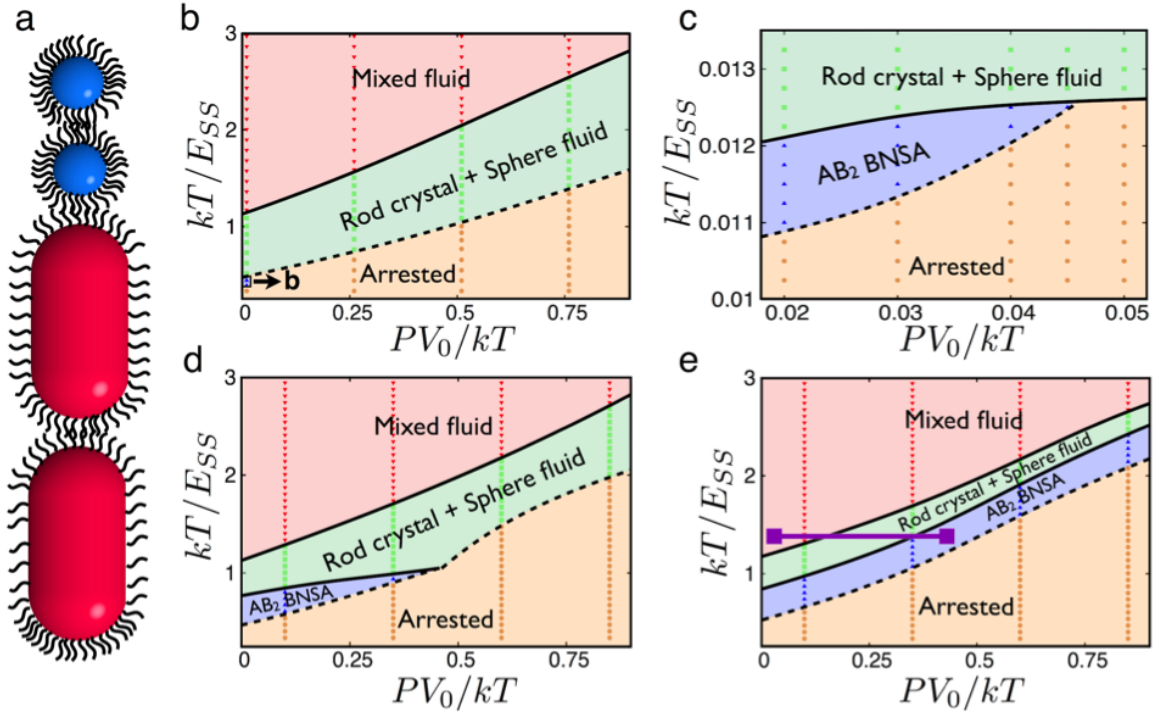


Figure 6.9: Phase behavior of the spherocylinder-sphere system from MC simulations. (a) Schematic representation of NSs and NRs with molecular ligands. NC interaction is dominated by the attraction of the ligands. Ligand lengths are exaggerated by a factor of about 3 for visualization purposes. (b-e) Reduced pressure PV_0/kT vs. reduced temperature kT/E_{SS} phase diagrams are shown for different values of the rod-sphere attraction asymmetry kT/E_{SS} (see text) at (a,b) $\xi_{RS} = 1.0$, (c) $\xi_{RS} = 1.4$, and (d) $\xi_{RS} = 1.6$. The symbols represent simulation data points. The small region of stability for the AB₂ BNSA in (a) is magnified and shown in (b). The purple line in (d) represents a possible self-assembly pathway for the assembly of the AB₂ BNSA from the fluid phase observed in experiment.

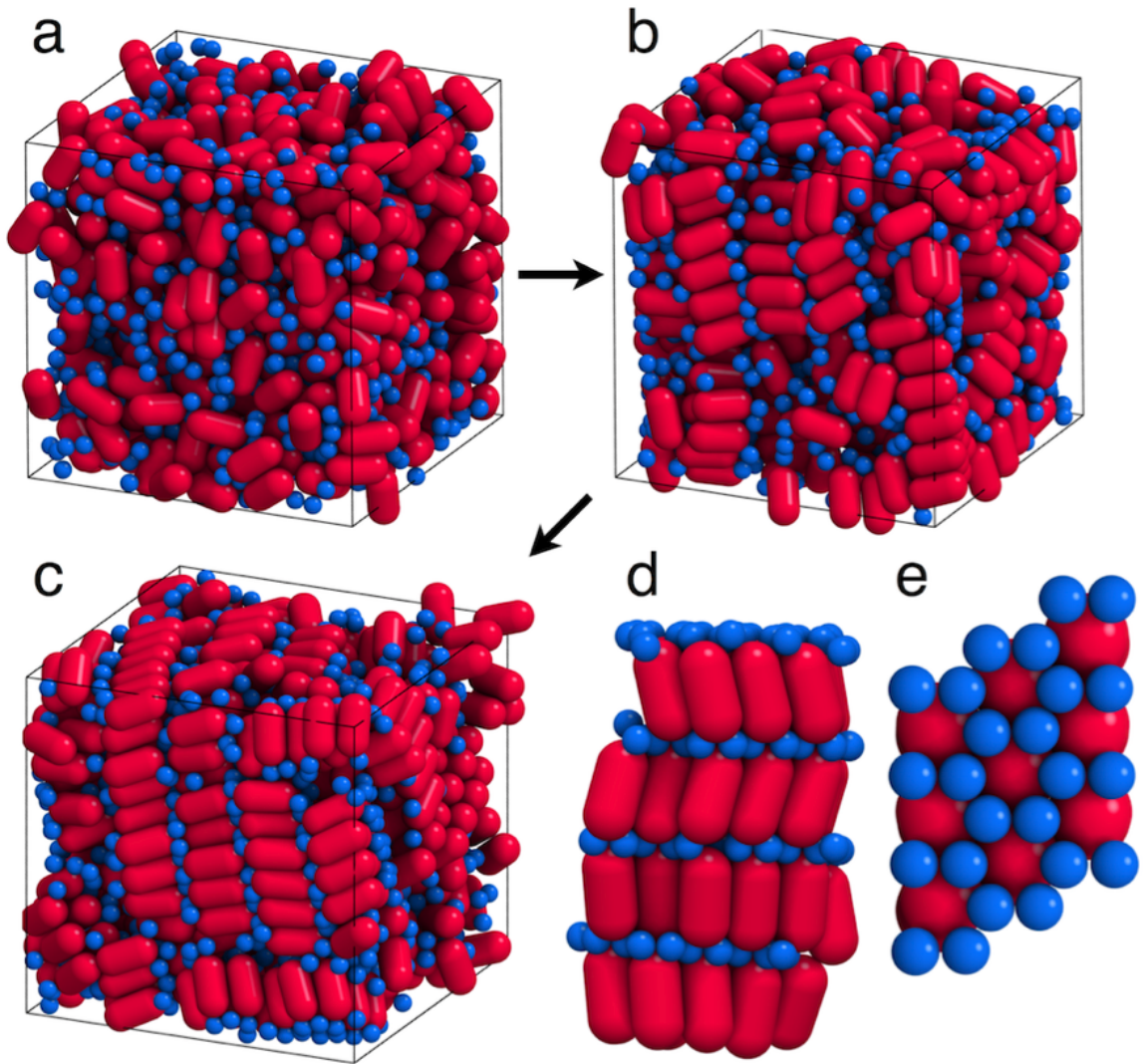


Figure 6.10: Self-assembly simulation of the AB_2 binary spherocylinder-sphere crystal. (a-c) Time evolution of a simulation of 1536 particles (512 spherocylinders and 1024 spheres) at packing fraction $\phi = 0.58$ and temperature $T = 0.519$ using $\xi_{RS}=1.5$. Snapshots are taken during crystallization after (a) 0.5×10^6 , (b) 1.35×10^6 , and (c) 3.3×10^6 MC sweeps. (d,e) A small part of the system cut out from the simulation demonstrates the local order corresponding to the AB_2 BNSA. Hexagonal layers of spherocylinders are separated by honeycomb layers of spheres as visible from the side (d) and from the top (e).

A standard way to treat such a situation theoretically is the simple Derjaguin approximation^{176,177}. However, due to the anisotropy of the NRs, the curvature on the surface is highly non-uniform and the Derjaguin approximation is not applicable. Instead, we resort to the determination of contact forces without approximation and tabulate pair interactions as a function of NC separation and orientation using MC integration over the NC surfaces (Fig. 6.2). We assume a homogeneous distribution of ligands on the NRs and the NSs. Since spheres have the highest curvature, the sphere-sphere interaction is weaker than the rod-sphere interaction, which in turn is weaker than the rod-rod interaction. In addition, the rod attracts a sphere (a rod) maximally if the sphere attaches to the side of the rod (the rods are parallel side-by-side) as shown in Fig. 6.3.

We perform NPT MC simulations from a disordered (fluid) starting configuration using the pre-calculated interaction tables. The short-range attractions significantly speed up the kinetics of the assembly process compared to the hard particle case, which permits a summary of the findings of the simulations in a P-T phase diagram (Fig. 6.9b). The phase behavior is relatively simple. Independent of the choice of temperature, increasing pressure always triggers phase separation into an ordered rod phase and a fluid sphere phase. The crystallization of spheres is observed only at substantially lower temperature. We can understand the difference in melting temperatures of the rod crystal and the sphere crystal by comparing the ground state energies per NC. The energy of the sphere crystal, E_{SS} , is significantly lower than the energy of the rod crystal, $E_{RR} = 4.7E_{SS}$, which in turn is slightly higher than the energy of the binary AB_2 BNSA, $E_{RS} = 3.6E_{SS}$. While the AB_2 BNSA is also observed in the phase diagram, it occurs only in a narrow parameter range at low temperature and very low pressure (Fig. 6.10d). The stability window is too small and inaccessible to experiments, which are performed at constant temperature.

6.6.2 Role of relative interaction strength

The MC integration that was used to calculate the interaction tables introduces a natural hierarchy of attraction strengths between different NC species, $|E_{RR}| > |E_{RS}| > |E_{SS}|$. Such a hierarchy aids the formation of the lamellar phase (and possibly the AB₂ BNSA) by disfavoring bulk demixing¹⁷⁰. However, while the sequence of interaction strengths is fixed by the particle geometry, their precise value is highly sensitive to the precise experimental conditions and is not known to us. For example, variations in the NC curvature, chemical composition and the crystallographic termination of NC facets can influence the relative strength of attractions between species^{31,43,156}. We consider these effects by enhancing the rod-sphere interaction energy by a factor $\xi_{RS} > 1$ relative to the other interactions to the other interactions $\xi_{RS}E_{RS}$, which disfavors demixing. A factor $\xi_{RS} < 1$ or any other variation of the relative interaction strengths does not improve the stability of BNSAs.

The P-T phase diagram (Fig. 6.9d) shows a significant improvement of the stability of the AB₂ BNSA already for $\xi_{RS} = 1.4$, broadening the temperature and pressure regime where it is found in simulation. This behavior is expected because an increase of ξ_{RS} raises the melting temperature of the AB₂ BNSA. For $\xi_{RS} = 1.6$ (Fig. 6.9e), not only is the AB₂ BNSA stabilized further, but also the boundaries of its stability range in the phase diagram are altered. Isothermic compression (depicted by a dotted line in Fig. 6.9d), which resembles the conditions present in experiments most closely, can now successfully transform the fluid to the AB₂ BNSA. Only a narrow regime where macro-phase separation dominates has to be traversed. In this way, an adjustment of the relative interaction strengths can open a kinetic pathway for the formation of the AB₂ BNSA. We show the different stages of the assembly process of the AB₂ BNSA in Fig. 6.10. The less diffusive spherocylinders initiate the assembly process by aligning parallel to another. The spheres, which have high mobility, surround

the spherocylinders and fit into the gaps between the spherocylinder caps. Once the spheres adopt their native open honeycomb arrangement, they act as a template for the next layer of spherocylinders. Note that multiple grain boundaries are present in our simulation. This limitation of the crystal size is caused by periodic boundary conditions as well as the total simulation time. Assembly experiments can access significantly longer equilibration times as evidenced by the high quality of the AB₂ BNSAs.

6.7 Conclusions

We have demonstrated binary assemblies of colloidal NRs and NSs into several unprecedented phases including the 3D long-range ordered AB₂ BNSAs. On the basis of experimental observations and simulation results, we have identified the key elements necessary for successful assembly of the AB₂ rod-sphere BNSAs: (i) favorable particle geometry a size ratio close to $\gamma = 0.55$ and rods with spherical caps allow dense packing and maximize entropic forces, (ii) attractive contact interactions they help to initiate the assembly process, (iii) optimal interaction strengths varying the relative strength of interactions between NCs of different compositions can minimize the width of the demixing zone in the phase diagram. Given the ubiquity of rods and spheres among NC building blocks and the added advantage of shape-dependent properties often associated with NRs, we believe that the lamellar phase and the AB₂ BNSAs can be formed with many rod-sphere combinations. Co-assembly of NRs and NSs into ordered arrays opens up new horizons for the chemical design of NC-based mesoscale metamaterials exhibiting intriguing physical properties.

CHAPTER VII

Conclusion and outlook

7.1 Conclusions and outlook

In this dissertation we used Monte Carlo simulations to study the self-assembled patterns of two- and -three dimensional anisotropic particles guided by current advances in synthesis and assembly results. In particular we focused on the study of:

- the effect of entropy that arises solely from hard interactions induced by the particles shape,
- the interplay between entropic forces and short-ranged enthalpic forces, namely van der Waals interactions, with the purpose of reproducing experimental assemblies results,
- phase behavior of a family of numerous particle shapes in the presence of entropic and enthalpic forces,
- and the identification of underlying design rules of two-dimensional systems that can be generalized to different type of systems that are under current rigorous studying.

All of these conclusions were derived from simulations guided and inspired by experimental progress. The results presented in Chapter 3 are the product of a joint experimental and numerical work were it was reported the synthesis of a family of

highly faceted planar platelets, that exhibited rich and subtle self-assembly behavior, it was demonstrated that a combination of particle shape and directional attractions resulting from the heterogeneous coverage of ligands around the nanoplate edges is responsible for the self-assembly of nanocrystal superlattices that structurally deviate from those resulting from entropic forces alone. From this work it was concluded that precise controlled in synthesis of shaped and faceted nanoplates not only enables the study of interplay between energy and entropy during self-assembly, but also provides a means opportunity to enhanced the interaction asymmetry through edge- and facet-selective chemical modification.

In chapter 4 it was shown that continuous shape transformation in the presence of short-ranged attractive forces stabilizes space-filling, porous and complex tilings at intermediate densities. The proposed design rules constitute a first step towards the understanding of shape optimization and provided a deeper understanding of its effect on self-assembly. The presented heuristic rules for shape optimization would allow experimentalists to tune the shapes and surface decoration of anisotropic building blocks to realize the crystal properties of target structures. These results stands as a guiding outline for experimentalists.

In chapter 5 the necessary entropic force and enthalpic forces - motivated by current advancements particle synthesis and thus accessible in in experiments - for self-assembling the eleven Archimedean tilings were presented. The premise of interplay between entropic and "sticky" forces was again exploded. In this chapter it was shown that with entropy alone, the regular Archimedean tilings can be self-assemble in the limit of infinite pressure because they constitute the stable densest packings of its regular tiles. These findings are reduced to single component systems only, and reinforces the concept of an entropic patch as a governing forces for self-assembly. The introduction of sticky forces in these systems did not alter the results. In contrast,

for low density packings, symmetric enthalpic patches are required. For the case of binary mixtures of regular shapes it was observed a rich behavior that directly depends on the complexity of interactions and particle geometry. We observe that hard binary mixtures tend to be disordered when mixed and that there is no trend to form the target structures, at least for simulation timescales. In the presence of enthalpic patches, complete demixing occurs with a multi-stage melting scenario if the difference between the coordination, directly dependent on the number of facets of the polygons, is sufficiently large. This trend is observed in the demixing of hexagon-square and hexagon-triangle assemblies, whereas square-triangle mixtures remain disordered. Shape-specific and edge-specific patches stabilize the remaining semi-regular tilings. Although nanoplate patterning inspires the designs developed in this work, these enthalpic design rules need not to be restricted to nanoscale systems and can also be imported to supramolecular systems, where particle interactions are programmable and particle self-diffusivity are faster.

Finally in Chapter 6 studies on three dimensional systems were presented. The binary assemblies of colloidal nanorods and nanosphers into several unprecedented phases including the 3D long-range ordered AB_2 BNSAs (Binary Nanoparticle Shape Alloy) were experimentally and numerically accomplished. On the basis of experimental observations and simulation results, we identified the key elements necessary for successfully assembling the AB_2 rod-sphere BNSAs: (i) favorable particle geometry a size ratio close to $\gamma = 0.55$ and rods with spherical caps allow dense packing and maximization of entropic forces, (ii) the introduction of attractive contact interactions that overcome the natural trend to completely demix and initiate the assembly process towards the BNSA, (iii) tuning of selective interaction strength that favors the attraction between nanorods and nanospheres and that expands the width of stability of BNSSA in the phase diagram.

7.1.1 Outlook

7.1.2 Towards complex structures in two-dimensional tilings

Further understanding of the effect of anisotropy dimensions is needed to fabricate nanostructures that can mimic structures of molecular systems. The results presented in this thesis constitutes steps in this direction. Although this works presented a wide variety of complex structures both experimentally and numerically and design rules were drawn based on these results, however; more powerful framework that can guide the fabrication of the materials of the future is needed.

Guided by the design rules extrapolated from the two-dimensional results in this work, specially for the case of nanoplates, it is appealing to introduce further complexity in the structures of tilings. A logical question is related to the identification of design rules that would lead to the formation of two-dimensional quasicrystalline tilings, especially for the elusive quasi-periodic tilings in both experiments or simulations, e.g. octagonal, decagonal quasicrystal, among others (See Figure 7.1). These structures are of particular interest given their visual appeal and mechanical properties. Notice that these complex tilings can be represented with convex polygons and thus it is reasonable, based on the results in Chapter 3, to form nanoplates in experiments to assemble structures. With the proper introduction of selective short-ranged enthalpic forces to overcome macrophase demixing that favor proper edge-to-edge local motifs - e.g. local rules of particle between particles lead to the formation of some of the complex Penrose tilings- the self-assembly of such complex structures looks realizable in simulation. An identification of which is a minimal set of design rules to self-assemble such structures would be a great accomplishment and a confirmation that anisotropy is a favorable route towards self-assembly of complex structures.

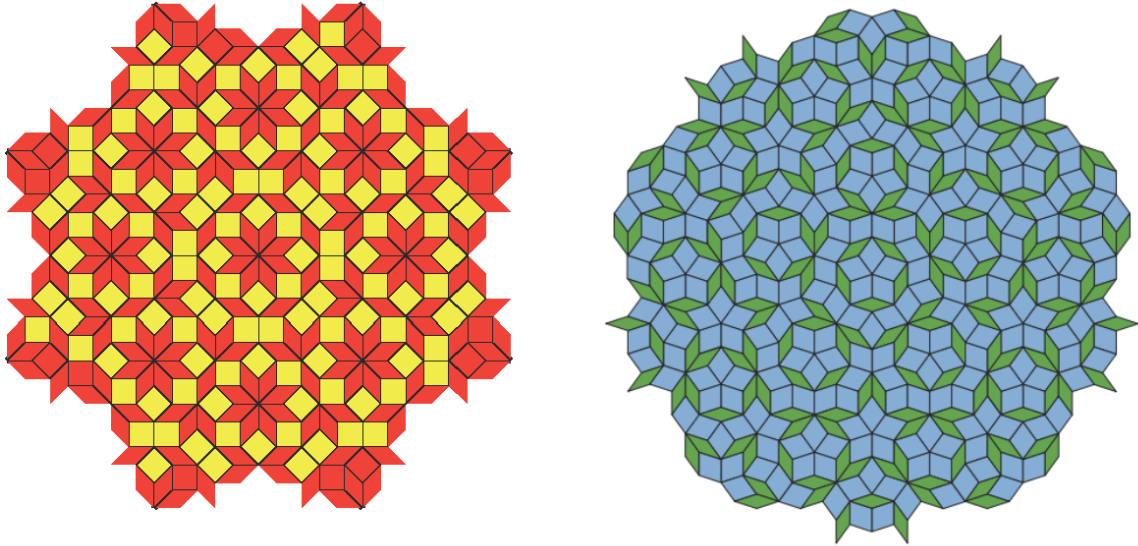


Figure 7.1: Octagonal quasicrystal (left) and P1 Penrose tiling (right).

7.1.3 Two-dimensional melting of hard and sticky with irregular shape

Melting in two-dimensions remains as a key topic, specially for the case of hard particles. Recent studies of hard disks show a melting scenario that differs from the Kosterlitz-Thouless-Halperin-Nelson-Young (KTNHY) standard melting, which predicts a continuous liquid-hexatic transition followed another continuous hexatic-solid transition. In fact, Krauth et al.¹⁷⁸ found a clear first-order liquid-hexatic transition that was later corroborated by Engel et al *via* different numerical approaches. Of great interest would be to understand the effect of shape on the melting scenerio in two dimensional shapes. For this purpose, current work done in the Glotzer group has recently focused on tthe melting of regular polygons (triangles, squares, pentagons, hexagons, heptagons) given that these shapes are commonly synthesized in the nanocrystal community. Preliminary results showed that pentagons do exhibit a liquid-rotator solid transition with no indication of a hexatic mesophase. Contrastingly, hexagons exhibit a continuous (pressure vs. packing) fraction equation of state and systematic analysis of thermodynamic state points showed continuous

liquid-hexatic and hexatic -(rotator) solid transformations. It remains to investigate if a hexatic and tetratic phases can be observed for triangles and squares, respectively. Studies of hard dimers (rhombs, rectangles, couple-pentagons, couple-hexagons) would be also of great interest given that these shapes are accessible to current synthesis techniques. An additional step in the model complexity would be the introduction of soft attractive interactions to these system model. Hard disks accompanied with soft interactions power law interactions $\propto r^{-n}$ show a continuous liquid-hexatic transition for $n \leq 6$. Thus interactions could potentially preclude or affect the type of liquid-hexatic transition.

7.1.4 Three-dimensional self-assembly from sticky polyhedral particles

In the case of three dimensional shapes, most of recent work focuses on hard systems. Damasceno showed that structure variety can be self-assemble solely from excluded volume effects alone¹⁵. Of particular interest would be to introduced enthalpic interactions, starting from those of short-ranges character given their ubiquitous presence in experiments. It would interesting to explore the 145 shapes that Damasceno *et al.*¹⁵ used in his simulations and compared the difference in structure assembly for each shape. given that sticky polygons self-assemble complex structures, three dimensional shapes can present the same richness in phase behavior.

Only one chapter was devoted to the three-dimensional case of binary systems, and in it we showed how novel binary structure can be self-assembled. We identify difficulties that may arise in multi-component systems and we also highlight how subtle interplay between entropic and enthalpic forces can come into agreement and self-assembly a seemingly more complex structure. Despite these amazing results, we must admit that this work focuses on possibly the most commonly synthesized nanoparticles, that is nanospheres and nanorods. Guided by these identified mech-

anism, it looks promising to explore the self-assembly of binary systems of binary systems, that exhibit both anisotropy in shape and patterning. A first step would be to select target structure that completely filled space and evaluate the hypothesis that sticky forces can overcome demixing, if this trend exist. If homogeneous interactions are not sufficient to form the target structure, an identification of the necessary selective interactions are desired.

BIBLIOGRAPHY

BIBLIOGRAPHY

- [1] Tapan K. Sau and Catherine J. Murphy. Self-assembly patterns formed upon solvent evaporation of aqueous cetyltrimethylammonium bromide-coated gold nanoparticles of various shapes. *Langmuir : the ACS journal of surfaces and colloids*, 21(7):2923–9, March 2005.
- [2] Masaharu Tsuji, Xinling Tang, Mika Matsunaga, Yoshinori Maeda, and Midori Watanabe. Shape Evolution of Flag Types of Silver Nanostructures from Nanorod Seeds in PVP-Assisted DMF Solution. *Crystal Growth & Design*, 10(12):5238–5243, December 2010.
- [3] Mukul Pradhan, Sougata Sarkar, Arun Kumar Sinha, Mrinmoyee Basu, and Tarasankar Pal. Morphology controlled uranium oxide hydroxide hydrate for catalysis, luminescence and SERS studies. *CrystEngComm*, 13(8):2878, April 2011.
- [4] Akrajas Ali Umar, Munetaka Oyama, Muhamad Mat Salleh, and Burhanuddin Yeop Majlis. Formation of High-Yield Gold Nanoplates on the Surface: Effective Two-Dimensional Crystal Growth of Nanoseed in the Presence of Poly(vinylpyrrolidone) and Cetyltrimethylammonium Bromide. *Crystal Growth & Design*, 9(6):2835–2840, June 2009.
- [5] Xingchen Ye, Joshua E Collins, Yijin Kang, Jun Chen, Daniel T N Chen, Arjun G Yodh, and Christopher B Murray. Morphologically controlled synthesis of colloidal upconversion nanophosphors and their shape-directed self-assembly. *Proc. Natl. Acad. Sci. U. S. A.*, 107(52):22430–22435, December 2010.
- [6] Ya Wen Zhang, Xiao Sun, Rui Si, Li Ping You, and Chun Hua Yan. Single-crystalline and monodisperse LaF₃ triangular nanoplates from a single-source precursor. *J. Am. Chem. Soc.*, 127(10):3260–3261, March 2005.
- [7] Huaibin Shen, Hongzhe Wang, Hang Yuan, Lan Ma, and Lin Song Li. Size-, shape-, and assembly-controlled synthesis of Cu₂xSe nanocrystals via a non-injection phosphine-free colloidal method. *CrystEngComm*, 14(2):555, 2012.
- [8] Rajiv Saini, Santosh Saini, and Sugandha Sharma. Nanotechnology: the future medicine. *Journal of cutaneous and aesthetic surgery*, 3(1):32–3, January 2010.
- [9] George M Whitesides and Bartosz Grzybowski. Self-assembly at all scales. *Science (New York, N. Y.)*, 295(5564):2418–21, March 2002.

- [10] Sharon C Glotzer and Michael J Solomon. Anisotropy of building blocks and their assembly into complex structures. *Nature Mater.*, 6(8):557–562, August 2007.
- [11] Lars Onsager. The effects of shape on the interaction of colloidal particles. *Annals of the New York Academy of Sciences*, 51(4):627–659, May 1949.
- [12] Wendell Meredith Stanley. Crystalline Tobacco-Mosaic Virus Protein Author (s): W . M . Stanley Published by : Botanical Society of America TOBACCO-MOSAIC W . M . Stanley. *American Journal of Botany*, 24(2):59–68, 2015.
- [13] Henk N W Lekkerkerker and A Stroobants. Ordering entropy. *Nature*, 393:305–306, February 1998.
- [14] Marie Adams, Zvonimir Dogic, SL Keller, and Seth Fraden. Entropically driven microphase transitions in mixtures of colloidal rods and spheres. *Nature*, 702(1997):590–593, 1998.
- [15] Pablo F Damasceno, Michael Engel, and Sharon C Glotzer. Predictive self-assembly of polyhedra into complex structures. *Science*, 337(6093):453–457, July 2012.
- [16] Sharon C. Glotzer. Self-Assembly of Patchy Particles. *Nano Letters*, 4(8):1407–1413, August 2004.
- [17] Taleb Mokari, Eli Rothenberg, Inna Popov, Ronny Costi, and Uri Banin. Selective growth of metal tips onto semiconductor quantum rods and tetrapods. *Science (New York, N. Y.)*, 304(5678):1787–90, June 2004.
- [18] Gang Zhang, Dayang Wang, and Helmuth Möhwald. Decoration of microspheres with gold nanodots—giving colloidal spheres valences. *Angewandte Chemie (International ed. in English)*, 44(47):7767–70, December 2005.
- [19] Zhiyong Tang, Zhenli Zhang, Ying Wang, Sharon C Glotzer, and Nicholas a Kotov. Self-assembly of CdTe nanocrystals into free-floating sheets. *Science (New York, N. Y.)*, 314(5797):274–8, October 2006.
- [20] Daan Frenkel and Anthony J. C. Ladd. New Monte Carlo method to compute the free energy of arbitrary solids. Application to the fcc and hcp phases of hard spheres. *The Journal of Chemical Physics*, 81(7):3188, 1984.
- [21] Nicholas Metropolis, Arianna W. Rosenbluth, Marshall N. Rosenbluth, Augusta H. Teller, and Edward Teller. Equation of State Calculations by Fast Computing Machines. *The Journal of Chemical Physics*, 21(6):1087, 1953.
- [22] Matthew R Jones, Robert J Macfarlane, Byeongdu Lee, Jian Zhang, Kaylie L Young, Andrew J Senesi, and Chad A Mirkin. DNA-nanoparticle superlattices formed from anisotropic building blocks. *Nature Mater.*, 9(11):913–917, November 2010.

- [23] Xiaomin Li, Huaibin Shen, Jinzhong Niu, Sen Li, Yongguang Zhang, Hongzhe Wang, and Lin Song Li. Columnar self-assembly of Cu₂S hexagonal nanoplates induced by tin(IV)-X complex as inorganic surface ligand. *Journal of the American Chemical Society*, 132(37):12778–9, September 2010.
- [24] Mark R Langille, Jian Zhang, Michelle L Personick, Shuyou Li, and Chad A Mirkin. Stepwise evolution of spherical seeds into 20-fold twinned icosahedra. *Science*, 337(6097):954–957, August 2012.
- [25] Aaron E Saunders, Ali Ghezelbash, Detlef M Smilgies, Michael B Sigman, and Brian A Korgel. Columnar self-assembly of colloidal nanodisks. *Nano Lett.*, 6(12):2959–2963, December 2006.
- [26] Elena V Shevchenko, Dmitri V Talapin, Christopher B Murray, and Stephen O’Brien. Structural characterization of self-assembled multifunctional binary nanoparticle superlattices. *J. Am. Chem. Soc.*, 128(11):3620–3637, March 2006.
- [27] M E Leunissen, C G Christova, A P Hynninen, C P Royall, A I Campbell, A Imhof, M Dijkstra, R van Roij, and A van Blaaderen. Ionic colloidal crystals of oppositely charged particles. *Nature*, 437(7056):235–240, September 2005.
- [28] Anand Yethiraj and Alfons van Blaaderen. A colloidal model system with an interaction tunable from hard sphere to soft and dipolar. *Nature*, 421(6922):513–517, January 2003.
- [29] Qian Chen, Sung Chul Bae, and Steve Granick. Directed self-assembly of a colloidal kagome lattice. *Nature*, 469(7330):381–384, January 2011.
- [30] Robert J Macfarlane, Byeongdu Lee, Matthew R Jones, Nadine Harris, George C Schatz, and Chad A Mirkin. Nanoparticle superlattice engineering with DNA. *Science*, 334(6053):204–208, October 2011.
- [31] Kyle J M Bishop, Christopher E Wilmer, Siowling Soh, and Bartosz A Grzybowski. Nanoscale forces and their uses in self-assembly. *Small*, 5(14):1600–1630, July 2009.
- [32] Kun Zhao, Robijn Bruinsma, and T.G. Mason. Entropic crystal–crystal transitions of Brownian squares. *Proc. Natl. Acad. Sci. U. S. A.*, 108(7):2684–2687, 2011.
- [33] Amir Haji-Akbari, Michael Engel, Aaron S Keys, Xiaoyu Zheng, Rolfe G Petschek, Peter Palffy-Muhoray, and Sharon C Glotzer. Disordered, quasicrystalline and crystalline phases of densely packed tetrahedra. *Nature*, 462(7274):773–777, December 2009.
- [34] Pablo F Damasceno, Michael Engel, and Sharon C Glotzer. Crystalline assemblies and densest packings of a family of truncated tetrahedra and the role of directional entropic forces. *ACS Nano*, 6(1):609–614, January 2012.

- [35] Umang Agarwal and Fernando A Escobedo. Mesophase behaviour of polyhedral particles. *Nature Mater.*, 10(3):230–235, March 2011.
- [36] Karol Miszta, Joost de Graaf, Giovanni Bertoni, Dirk Dorfs, Rosaria Brescia, Sergio Marras, Luca Ceseracciu, Roberto Cingolani, René van Roij, Marjolein Dijkstra, and Liberato Manna. Hierarchical self-assembly of suspended branched colloidal nanocrystals into superlattice structures. *Nature Materials*, 10(11):872–876, September 2011.
- [37] Joel Henzie, Michael Grünwald, Asaph Widmer-Cooper, Phillip L. Geissler, and Peidong Yang. Self-assembly of uniform polyhedral silver nanocrystals into densest packings and exotic superlattices. *Nature Mater.*, 11:131–137, November 2011.
- [38] Maryna I Bodnarchuk, Maksym V Kovalenko, Wolfgang Heiss, and Dmitri V Talapin. Energetic and entropic contributions to self-assembly of binary nanocrystal superlattices: temperature as the structure-directing factor. *J. Am. Chem. Soc.*, 132(34):11967–11977, September 2010.
- [39] Wiel H Evers, Bart De Nijs, Laura Filion, Sonja Castillo, Marjolein Dijkstra, and Daniel Vanmaekelbergh. Entropy-driven formation of binary semiconductor-nanocrystal superlattices. *Nano Lett.*, 10(10):4235–4241, October 2010.
- [40] Zhuoying Chen, Jenny Moore, Guillaume Radtke, Henning Siringhaus, and Stephen O’Brien. Binary nanoparticle superlattices in the semiconductor-semiconductor system: CdTe and CdSe. *J. Am. Chem. Soc.*, 129(50):15702–15709, December 2007.
- [41] Zhuoying Chen and Stephen O’Brien. Structure direction of II-VI semiconductor quantum dot binary nanoparticle superlattices by tuning radius ratio. *ACS Nano*, 2(6):1219–1229, June 2008.
- [42] Angang Dong, Xingchen Ye, Jun Chen, and Christopher B Murray. Two-dimensional binary and ternary nanocrystal superlattices: the case of monolayers and bilayers. *Nano Lett.*, 11(4):1804–1809, April 2011.
- [43] Matthew R Jones, Robert J Macfarlane, Andrew E Prigodich, Pinal C Patel, and Chad A Mirkin. Nanoparticle shape anisotropy dictates the collective behavior of surface-bound ligands. *J. Am. Chem. Soc.*, 133(46):18865–18869, November 2011.
- [44] Sharon C Glotzer. Nanotechnology: Shape matters. *Nature*, 481(7382):450–452, January 2012.
- [45] Clive R Bealing, William J Baumgardner, Joshua J Choi, Tobias Hanrath, and Richard G Hennig. Predicting nanocrystal shape through consideration of surface-ligand interactions. *ACS Nano*, 6:2118–2127, February 2012.

- [46] Matthew O Blunt, James C Russell, María Del Carmen Giménez-López, Juan P Garrahan, Xiang Lin, Martin Schröder, Neil R Champness, and Peter H Beton. Random tiling and topological defects in a two-dimensional molecular network. *Science*, 322(5904):1077–1081, November 2008.
- [47] Andrew Stannard, James C. Russell, Matthew O. Blunt, Christos Salesiotis, María Del Carmen Giménez-López, Nassiba Taleb, Martin Schröder, Neil R. Champness, Juan P. Garrahan, and Peter H. Beton. Broken symmetry and the variation of critical properties in the phase behaviour of supramolecular rhombus tilings. *Nature Chem.*, 4(2):112–117, February 2012.
- [48] Stephen Whitelam, Isaac Tamblyn, Peter Beton, and Juan Garrahan. Random and ordered phases of off-lattice rhombus tiles. *Phys. Rev. Lett.*, 108(3):1–4, January 2012.
- [49] Feng Wang, Yu Han, Chin Seong Lim, Yunhao Lu, Juan Wang, Jun Xu, Hongyu Chen, Chun Zhang, Minghui Hong, and Xiaogang Liu. Simultaneous phase and size control of upconversion nanocrystals through lanthanide doping. *Nature*, 463(7284):1061–1065, February 2010.
- [50] Andrew Stannard, Matthew O. Blunt, Peter H. Beton, and Juan P. Garrahan. Entropically stabilized growth of a two-dimensional random tiling. *Phys. Rev. E*, 82(4):041109, October 2010.
- [51] Kun Zhao and Thomas G Mason. Twinning of Rhombic Colloidal Crystals. *J. Am. Chem. Soc.*, 134:18125–18131, October 2012.
- [52] A Zalkin and D H Templeton. The crystal structures of YF₃ and related compounds. *J. Am. Chem. Soc.*, 75(10):2453–2458, 1953.
- [53] Angang Dong, Jun Chen, Patrick M Vora, James M Kikkawa, and Christopher B Murray. Binary nanocrystal superlattice membranes self-assembled at the liquid-air interface. *Nature*, 466(7305):474–477, July 2010.
- [54] van der Kooij F. M., K Kassapidou, and H. M. W. Lekkerkerker. Liquid crystal phase transitions in suspensions of polydisperse plate-like particles. *Nature*, 406(6798):868–871, August 2000.
- [55] Taejong Paik, Dong-Kyun Ko, Thomas R Gordon, Vicky Doan-Nguyen, and Christopher B Murray. Studies of liquid crystalline self-assembly of GdF nanoplates by in-plane, out-of-plane SAXS. *ACS Nano*, 5(10):8322–8230, October 2011.
- [56] Sylvie Roke, Otto Berg, Johan Buitenhuis, Alfons van Blaaderen, and Mischa Bonn. Surface molecular view of colloidal gelation. *Proc. Natl. Acad. Sci. U. S. A.*, 103(36):13310–13314, September 2006.

- [57] Radha Narayanan and Mostafa A El-Sayed. Catalysis with transition metal nanoparticles in colloidal solution: nanoparticle shape dependence and stability. *The journal of physical chemistry. B*, 109(26):12663–76, July 2005.
- [58] Benjamin J Wiley, Sang Hyuk Im, Zhi-Yuan Li, Joeseeph McLellan, Andrew Siekkinen, and Younan Xia. Maneuvering the surface plasmon resonance of silver nanostructures through shape-controlled synthesis. *The journal of physical chemistry. B*, 110(32):15666–75, August 2006.
- [59] Traci Jensen, Lance Kelly, Anne Lazarides, and GC Schatz. Electrodynamics of noble metal nanoparticles and nanoparticle clusters. *Journal of Cluster Science*, 10(2):295–317, 1999.
- [60] Costas M. Soukoulis and Martin Wegener. Past achievements and future challenges in the development of three-dimensional photonic metamaterials. *Nature Photonics*, 5(SEPTEMBER):523–530, July 2011.
- [61] Shanshan Lv, Daniel M Dudek, Yi Cao, M M Balamurali, John Gosline, and Hongbin Li. Designed biomaterials to mimic the mechanical properties of muscles. *Nature*, 465(7294):69–73, May 2010.
- [62] Y Charles Cao. Synthesis of square gadolinium-oxide nanoplates. *Journal of the American Chemical Society*, 126(24):7456–7, June 2004.
- [63] Y. Sun and Y. Xia. Triangular Nanoplates of Silver: Synthesis, Characterization, and Use as Sacrificial Templates For Generating Triangular Nanorings of Gold. *Advanced Materials*, 15(9):695–699, May 2003.
- [64] Ladislav Kavan, Jun-Ho Yum, and Michael Grätzel. Graphene nanoplatelets outperforming platinum as the electrocatalyst in co-bipyridine-mediated dye-sensitized solar cells. *Nano letters*, 11(12):5501–6, December 2011.
- [65] Lehui Lu, Atsuko Kobayashi, Keiko Tawa, and Yukihiro Ozaki. Silver Nanoplates with Special Shapes: Controlled Synthesis and Their Surface Plasmon Resonance and Surface-Enhanced Raman Scattering Properties. *Chemistry of Materials*, 18(20):4894–4901, October 2006.
- [66] Sukdeb Pal, Yu Kyung Tak, and Joon Myong Song. Does the antibacterial activity of silver nanoparticles depend on the shape of the nanoparticle? A study of the Gram-negative bacterium *Escherichia coli*. *Applied and environmental microbiology*, 73(6):1712–20, March 2007.
- [67] Youngsuk Kim, Hee Han, Yunseok Kim, Woo Lee, Marin Alexe, Sunggi Baik, and Jin Kon Kim. Ultrahigh density array of epitaxial ferroelectric nanoislands on conducting substrates. *Nano letters*, 10(6):2141–6, June 2010.
- [68] Zewei Quan and Jiye Fang. Superlattices with non-spherical building blocks. *Nano Today*, 5(5):390–411, 2010.

- [69] Yijin Kang, Jun Beom Pyo, Xingchen Ye, Rosa E Diaz, Thomas R Gordon, Eric A Stach, and Christopher B Murray. Shape-controlled synthesis of Pt nanocrystals: the role of metal carbonyls. *ACS nano*, 7(1):645–53, January 2013.
- [70] M.P. Pileni. Control of the Size and Shape of Inorganic Nanocrystals at Various Scales from Nano to Macrod domains. *Journal of Physical Chemistry C*, 111(26):9019–9038, July 2007.
- [71] Andrea R. Tao, Susan Habas, and Peidong Yang. Shape Control of Colloidal Metal Nanocrystals. *Small*, 4(3):310–325, March 2008.
- [72] Mathew M Maye, Oleg Gang, and Mircea Cotlet. Photoluminescence enhancement in CdSe/ZnS-DNA linked-Au nanoparticle heterodimers probed by single molecule spectroscopy. *Chemical communications (Cambridge, England)*, 46(33):6111–3, September 2010.
- [73] Trung Dac Nguyen and Sharon C Glotzer. Reconfigurable assemblies of shape-changing nanorods. *ACS nano*, 4(5):2585–94, May 2010.
- [74] Trung Dac Nguyen, Eric Jankowski, and Sharon C Glotzer. Self-assembly and reconfigurability of shape-shifting particles. *ACS nano*, 5(11):8892–903, November 2011.
- [75] Greg Van Anders, NK Ahmed, and Ross Smith. Entropically Patchy Particles Engineering Valence Through Shape Entropy. *ACS nano*, 2013.
- [76] Xingchen Ye, Jun Chen, Michael Engel, Jaime a. Millan, Wenbin Li, Liang Qi, Guozhong Xing, Joshua E. Collins, Cherie R. Kagan, Ju Li, Sharon C. Glotzer, and Christopher B. Murray. Competition of shape and interaction patchiness for self-assembling nanoplates. *Nature Chemistry*, 5(6):466–473, May 2013.
- [77] S Porel, S Singh, and T P Radhakrishnan. Polygonal gold nanoplates in a polymer matrix. *Chemical communications (Cambridge, England)*, 18:2387–9, May 2005.
- [78] Caixia Kan, Changshun Wang, Hongchen Li, Jingshan Qi, Jiejun Zhu, Zhaosheng Li, and Daning Shi. Gold microplates with well-defined shapes. *Small (Weinheim an der Bergstrasse, Germany)*, 6(16):1768–75, August 2010.
- [79] Hsin-Cheng Chu, Chun-Hong Kuo, and Michael H Huang. Thermal aqueous solution approach for the synthesis of triangular and hexagonal gold nanoplates with three different size ranges. *Inorganic chemistry*, 45(2):808–13, January 2006.
- [80] Bin Tang, Shuping Xu, Jing An, Bing Zhao, and Weiqing Xu. Photoinduced Shape Conversion and Reconstruction of Silver Nanoprisms. *The Journal of Physical Chemistry C*, 113(17):7025–7030, April 2009.

- [81] Younjin Min, Mustafa Akbulut, Kai Kristiansen, Yuval Golan, and Jacob Israelachvili. The role of interparticle and external forces in nanoparticle assembly. *Nature materials*, 7(7):527–38, July 2008.
- [82] Liang-shi Li and A. Alivisatos. Origin and Scaling of the Permanent Dipole Moment in CdSe Nanorods. *Physical Review Letters*, 90(9):097402, March 2003.
- [83] Stefan a Maier, Pieter G Kik, Harry a Atwater, Sheffer Meltzer, Elad Harel, Bruce E Koel, and Ari a G Requicha. Local detection of electromagnetic energy transport below the diffraction limit in metal nanoparticle plasmon waveguides. *Nature materials*, 2(4):229–32, April 2003.
- [84] W. Rechberger, a. Hohenau, a. Leitner, J.R. Krenn, B. Lamprecht, and F.R. Aussenegg. Optical properties of two interacting gold nanoparticles. *Optics Communications*, 220(1-3):137–141, May 2003.
- [85] Oleg Gang and Yugang Zhang. Shaping phases by phasing shapes. *ACS nano*, 5(11):8459–65, November 2011.
- [86] Y. Limon Duparcmeur, A. Gervois, and J. P. Troadec. Dense Periodic Packings of Regular Polygons. *Journal de Physique I*, 5(12):1539–1550, December 1995.
- [87] Jaime A Millan, Daniel Ortiz, Greg van Anders, and Sharon C Glotzer. Self-assembly of Archimedean tilings with enthalpically and entropically patchy polygons. *ACS nano*, 8(3):2918–28, March 2014.
- [88] R Nelson. Order, frustration, and defects in liquids and glasses. *Physical Review B*, 50(10):982–5535, 1983.
- [89] Leo Merz, Manfred Parschau, Laura Zoppi, Kim K Baldrige, Jay S Siegel, and Karl-Heinz Ernst. Reversible phase transitions in a buckyball monolayer. *Angewandte Chemie (International ed. in English)*, 48(11):1966–9, January 2009.
- [90] Suraj P. Gorkhali, Jun Qi, and Gregory P. Crawford. Switchable quasi-crystal structures with five-, seven-, and ninefold symmetries. *Journal of the Optical Society of America B*, 23(1):149, 2006.
- [91] Ting Chen, Zhenli Zhang, and Sharon C Glotzer. A precise packing sequence for self-assembled convex structures. *Proceedings of the National Academy of Sciences of the United States of America*, 104(3):717–22, January 2007.
- [92] Ting Chen, Zhenli Zhang, and Sharon C Glotzer. Simulation studies of the self-assembly of cone-shaped particles. *Langmuir : the ACS journal of surfaces and colloids*, 23(12):6598–605, June 2007.
- [93] Hyeong-chai Jeong and Paul J Steinhardt. Constructing Penrose-like tilings from a single prototile and the implications for quasicrystals. *Physical Review B*, 55(6):3520–3532, February 1997.

- [94] Yulun Tao, Yuhua Shen, Liangbao Yang, Bin Han, Fangzhi Huang, Shikuo Li, Zhuwang Chu, and Anjian Xie. Hierarchical self-assembly of hexagonal single-crystal nanosheets into 3D layered superlattices with high conductivity. *Nanoscale*, 4(12):3729–33, June 2012.
- [95] M. O’Keeffe and B. G. Hyde. Plane Nets in Crystal Chemistry. *Philosophical Transactions of the Royal Society A: Mathematical, Physical and Engineering Sciences*, 295(1417):553–618, February 1980.
- [96] E. Ressouche, V. Simonet, B. Canals, M. Gospodinov, and V. Skumryev. Magnetic Frustration in an Iron-Based Cairo Pentagonal Lattice. *Physical Review Letters*, 103(26):267204, December 2009.
- [97] Fei Zhang, Yan Liu, and Hao Yan. Complex Archimedean tiling self-assembled from DNA nanostructures. *Journal of the American Chemical Society*, 135(20):7458–61, May 2013.
- [98] Peter Stampfli. A dodecagonal quasi-periodic lattice in 2 dimensions. *Helv. Phys. Acta*, 59:1260–1263, 1986.
- [99] K. Kuo, Y. Feng, and H. Chen. Growth Model of Dodecagonal Quasicrystal Based on Correlated Tiling of Squares and Equilateral Triangles. *Physical Review Letters*, 61(15):1740–1743, October 1988.
- [100] Marjolein N van der Linden, Jonathan P K Doye, and Ard a Louis. Formation of dodecagonal quasicrystals in two-dimensional systems of patchy particles. *The Journal of chemical physics*, 136(5):054904, February 2012.
- [101] Geoffrey C. Shepherd Branko, Grünbaum. *Tilings and Patterns*. W H Freeman and Co, New York, 1987.
- [102] J. Veerman and D. Frenkel. Phase diagram of a system of hard spherocylinders by computer simulation. *Physical Review A*, 41(6):3237–3244, March 1990.
- [103] Michael H Huang and Po-Heng Lin. Shape-Controlled Synthesis of Polyhedral Nanocrystals and Their Facet-Dependent Properties. *Advanced Functional Materials*, 22(1):14–24, 2011.
- [104] Xiao-Feng Wu, Hai-Yan Song, Jeong-Mo Yoon, Yeon-Tae Yu, and Yun-Fa Chen. Synthesis of core-shell Au@TiO₂ nanoparticles with truncated wedge-shaped morphology and their photocatalytic properties. *Langmuir : the ACS journal of surfaces and colloids*, 25(11):6438–47, June 2009.
- [105] Stephanie H. Lee, Yanning Song, Ian D. Hosein, and Chekesha M. Liddell. Magnetically responsive and hollow colloids from nonspherical core-shell particles of peanut-like shape. *Journal of Materials Chemistry*, 19(3):350, 2009.

- [106] Yugang Zhang, Fang Lu, Daniel van der Lelie, and Oleg Gang. Continuous phase transformation in nanocube assemblies. *Physical Review Letters*, 107(13):135701, September 2011.
- [107] Kaifu Bian, Joshua J Choi, Ananth Kaushik, Paulette Clancy, Detlef-m Smilgies, and Tobias Hanrath. Shape-anisotropy driven symmetry transformations in nanocrystal superlattice polymorphs. *ACS nano*, 5(4):2815–23, April 2011.
- [108] Y. Yang, S. Matsubara, L. Xiong, T. Hayakawa, and M. Nogami. Solvothermal Synthesis of Multiple Shapes of Silver Nanoparticles and Their SERS Properties. *Journal of Physical Chemistry C*, 111(26):9095–9104, July 2007.
- [109] Tapan K Sau and Catherine J Murphy. Seeded high yield synthesis of short Au nanorods in aqueous solution. *Langmuir : the ACS journal of surfaces and colloids*, 20(15):6414–20, July 2004.
- [110] S. Sun. Monodisperse FePt Nanoparticles and Ferromagnetic FePt Nanocrystal Superlattices. *Science*, 287(5460):1989–1992, March 2000.
- [111] Dmitri V Talapin and Christopher B Murray. PbSe nanocrystal solids for n- and p-channel thin film field-effect transistors. *Science (New York, N.Y.)*, 310(5745):86–9, October 2005.
- [112] Joseph M Luther, Matt Law, Matthew C Beard, Qing Song, Matthew O Reese, Randy J Ellingson, and Arthur J Nozik. Schottky solar cells based on colloidal nanocrystal films. *Nano letters*, 8(10):3488–92, October 2008.
- [113] Yongcai Qiu, Wei Chen, and Shihe Yang. Double-Layered Photoanodes from Variable-Size Anatase TiO₂ Nanospindles: A Candidate for High-Efficiency Dye-Sensitized Solar Cells. *Angewandte Chemie*, 122(21):3757–3761, May 2010.
- [114] Kepler Johannes. *Harmonices Mundi*. Johannes Planck, Linz, 1619.
- [115] Lasko Basnarkov and Viktor Urumov. Diffusion on Archimedean lattices. *Physical Review E*, 73(4):046116, April 2006.
- [116] Mi McMahan, O Degtyareva, and Rj Nelmes. Ba-IV-type incommensurate crystal structure in group-V metals. *Physical review letters*, 85(23):4896–9, December 2000.
- [117] U Schlickum, R Decker, F Klappenberger, G Zoppellaro, S Klyatskaya, W Auwärter, S Neppel, K Kern, H Brune, M Ruben, and J V Barth. Chiral kagomé lattice from simple ditopic molecular bricks. *Journal of the American Chemical Society*, 130(35):11778–82, September 2008.
- [118] Kazukuni Tahara, Shuhei Furukawa, Hiroshi Uji-i, Tsutomu Uchino, Tomoyuki Ichikawa, Jian Zhang, Wael Mamdouh, Motohiro Sonoda, Frans C De Schryver, Steven De Feyter, and Yoshito Tobe. Two-dimensional porous molecular networks of dehydrobenzo[12]annulene derivatives via alkyl chain interdigitation. *Journal of the American Chemical Society*, 128(51):16613–25, December 2006.

- [119] Bin Chen, Xiangbing Zeng, Ute Baumeister, Goran Ungar, and Carsten Tschierske. Liquid crystalline networks composed of pentagonal, square, and triangular cylinders. *Science (New York, N.Y.)*, 307(5706):96–9, January 2005.
- [120] A. Takano, W. Kawashima, A. Noro, Y. Isono, N. Tanaka, T. Dotera, and Y. Matsushita. A mesoscopic Archimedean tiling having a new complexity in an ABC star polymer. *Journal of Polymer Science Part B: Polymer Physics*, 43(18):2427–2432, September 2005.
- [121] Jules Mikhael, Johannes Roth, Laurent Helden, and Clemens Bechinger. Archimedean-like tiling on decagonal quasicrystalline surfaces. *Nature*, 454(7203):501–4, July 2008.
- [122] S Ithurria, M D Tessier, B Mahler, R P S M Lobo, B Dubertret, and Al L Efos. Colloidal nanoplatelets with two-dimensional electronic structure. *Nature materials*, 10(12):936–41, December 2011.
- [123] Greg Van Anders, NK Ahmed, and Daphne Klotsa. Unified Theoretical Framework for Shape Entropy in Colloids. *arXiv:1309.1187*, 2013.
- [124] Benjamin D Smith, Kristen a Fichthorn, David J Kirby, Lisa M Quimby, Derek a Triplett, Pedro González, Darimar Hernández, and Christine D Keating. Asymmetric van der Waals Forces Drive Orientation of Compositionally Anisotropic Nanocylinders within Smectic Arrays: Experiment and Simulation. *ACS nano*, December 2013.
- [125] Zhihong Chen, Yu-Ming Lin, Michael J. Rooks, and Phaeton Avouris. Graphene nano-ribbon electronics. *Physica E: Low-dimensional Systems and Nanostructures*, 40(2):228–232, December 2007.
- [126] Gang Xu, Xiaoqiang Huang, Vladimir Krstic, Shuquan Chen, Xin Yang, Chunying Chao, Ge Shen, and Gaorong Han. Hydrothermal synthesis of single-crystalline tetragonal perovskite PbTiO_3 nanosheets with dominant (001) or (111) facets. *CrystEngComm*, 16(21):4373, 2014.
- [127] J Alex Lee, Linli Meng, David J Norris, L E Scriven, and Michael Tsapatsis. Colloidal crystal layers of hexagonal nanoplates by convective assembly. *Langmuir : the ACS journal of surfaces and colloids*, 22(12):5217–9, June 2006.
- [128] Kang Hyun Park, Kwonho Jang, and Seung Uk Son. Synthesis, optical properties, and self-assembly of ultrathin hexagonal In_2S_3 nanoplates. *Angewandte Chemie (International ed. in English)*, 45(28):4608–12, July 2006.
- [129] Yugang Sun and Younan Xia. Shape-controlled synthesis of gold and silver nanoparticles. *Science (New York, N.Y.)*, 298(5601):2176–9, December 2002.
- [130] Yunxia Chen, Xin He, Xiujian Zhao, Qihua Yuan, and Xingyong Gu. Preparation, characterization, and growth mechanism of a novel aligned nanosquare

- anatase in large quantities in the presence of TMAOH. *Journal of colloid and interface science*, 310(1):171–7, June 2007.
- [131] Amar B Pawar and Ilona Kretzschmar. Fabrication, assembly, and application of patchy particles. *Macromolecular rapid communications*, 31(2):150–68, January 2010.
- [132] Christopher R Iacovella and Sharon C Glotzer. Complex crystal structures formed by the self-assembly of ditethered nanospheres. *Nano letters*, 9(3):1206–11, March 2009.
- [133] S Sacanna, W T M Irvine, P M Chaikin, and D J Pine. Lock and key colloids. *Nature*, 464(7288):575–8, March 2010.
- [134] Renko de Vries. Depletion-induced instability in protein-DNA mixtures: Influence of protein charge and size. *The Journal of chemical physics*, 125(1):014905, July 2006.
- [135] Xingchen Ye, Jaime a Millan, Michael Engel, Jun Chen, Benjamin T Diroll, Sharon C Glotzer, and Christopher B Murray. Shape alloys of nanorods and nanospheres from self-assembly. *Nano letters*, 13(10):4980–8, October 2013.
- [136] Ananth P Kaushik and Paulette Clancy. Explicit all-atom modeling of realistically sized ligand-capped nanocrystals. *Journal of Chemical Physics*, 136(11):114702, March 2012.
- [137] Krzysztof Witold Wojciechowski and Daan Frenkel. Tetratic phase in the planar hard square system. *Comp Met Sci Technol*, 10:235–255, 2004.
- [138] Marjolein Dijkstra, René van Roij, and Robert Evans. Phase diagram of highly asymmetric binary hard-sphere mixtures. *Physical Review E*, 59(5):5744–5771, May 1999.
- [139] Erik D. Demaine and Martin L. Demaine. Jigsaw Puzzles, Edge Matching, and Polyomino Packing: Connections and Complexity. *Graphs and Combinatorics*, 23(S1):195–208, June 2007.
- [140] J O Fjærestad. The 3-edge-colouring problem on the 4–8 and 3–12 lattices. *Journal of Statistical Mechanics: Theory and Experiment*, 2010(01):P01004, January 2010.
- [141] J. An, B. Tang, X. Ning, J. Zhou, W. Xu, B. Zhao, C. Corredor, and J.R. Lombardi. Photoinduced Shape Evolution: From Triangular to Hexagonal Silver Nanoplates. *Journal of Physical Chemistry C*, 111(49):18055–18059, December 2007.
- [142] Yujie Xiong, Joseph M McLellan, Jingyi Chen, Yadong Yin, Zhi-Yuan Li, and Younan Xia. Kinetically controlled synthesis of triangular and hexagonal nanoplates of palladium and their SPR/SERS properties. *Journal of the American Chemical Society*, 127(48):17118–27, December 2005.

- [143] Menghua Li, Liqiang Xu, Changhui Sun, Zhicheng Ju, and Yitai Qian. Thermal-induced shape evolution from uniform triangular to hexagonal r-BN nanoplates. *Journal of Materials Chemistry*, 19(43):8086, 2009.
- [144] Huizhang Guo, Yuanzhi Chen, Hemei Ping, Laisen Wang, and Dong-Liang Peng. One-pot synthesis of hexagonal and triangular nickel-copper alloy nanoplates and their magnetic and catalytic properties. *Journal of Materials Chemistry*, 22(17):8336, 2012.
- [145] Bo Zhou, Yong Ji, Yu-Fei Yang, Xing-Hua Li, and Jun-Jie Zhu. Rapid Microwave-Assisted Synthesis of Single-Crystalline Sb₂Te₃ Hexagonal Nanoplates. *Crystal Growth & Design*, 8(12):4394–4397, December 2008.
- [146] L.Q. Xu, J. H. Zhan, J.Q. Hu, Y. Bando, X.L. Yuan, T. Sekiguchi, M. Mitome, and D. Golberg. High-Yield Synthesis of Rhombohedral Boron Nitride Triangular Nanoplates. *Advanced Materials*, 19(16):2141–2144, August 2007.
- [147] Chuan Zhang And and Yongfa Zhu*. Synthesis of Square Bi₂WO₆ Nanoplates as High-Activity Visible-Light-Driven Photocatalysts. *Chemistry of Materials*, June 2005.
- [148] Xintai Su, Feng Xiao, Yani Li, Jikang Jian, Qingjun Sun, and Jide Wang. Synthesis of uniform WO₃ square nanoplates via an organic acid-assisted hydrothermal process. *Materials Letters*, 64(10):1232–1234, May 2010.
- [149] Mihyun Park, Nohyun Lee, Seung Hong Choi, Kwangjin An, Seung-Ho Yu, Jeong Hyun Kim, Seung-Hae Kwon, Dokyoon Kim, Hyoungsu Kim, Sung-Il Baek, Tae-Young Ahn, Ok Kyu Park, Jae Sung Son, Yung-Eun Sung, Young-Woon Kim, Zhongwu Wang, Nicola Pinna, and Taeghwan Hyeon. Large-Scale Synthesis of Ultrathin Manganese Oxide Nanoplates and Their Applications to T1 MRI Contrast Agents. *Chemistry of Materials*, 23(14):3318–3324, July 2011.
- [150] Guangcheng Xi and Jinhua Ye. Synthesis of bismuth vanadate nanoplates with exposed {001} facets and enhanced visible-light photocatalytic properties. *Chemical communications (Cambridge, England)*, 46(11):1893–5, March 2010.
- [151] Taejong Paik, Thomas R Gordon, Andrew M Prantner, Hongseok Yun, and Christopher B Murray. Designing Tripodal and Triangular Gadolinium Oxide Nanoplates and Self-Assembled Nanofibrils as Potential Multimodal Bioimaging Probes. *ACS nano*, February 2013.
- [152] Yaping Zeng, Hongxing Li, Boyuan Xiang, Haiqing Ma, Baihua Qu, Mingxia Xia, Yicheng Wang, Qinglin Zhang, and Yanguo Wang. Synthesis and characterization of phase-purity Cu₉BiS₆ nanoplates. *Materials Letters*, 64(9):1091–1094, May 2010.

- [153] Dmytro Nykypanchuk, Mathew M Maye, Daniel van der Lelie, and Oleg Gang. DNA-guided crystallization of colloidal nanoparticles. *Nature*, 451(7178):549–552, January 2008.
- [154] Xingchen Ye, Jun Chen, and Christopher B Murray. Polymorphism in self-assembled AB6 binary nanocrystal superlattices. *Journal of the American Chemical Society*, 133(8):2613–2620, March 2011.
- [155] Xingchen Ye, Linghua Jin, Humeyra Caglayan, Jun Chen, Guozhong Xing, Chen Zheng, Vicky Doan-Nguyen, Yijin Kang, Nader Engheta, Cherie R Kagan, and Christopher B Murray. Improved Size-Tunable Synthesis of Monodisperse Gold Nanorods through the Use of Aromatic Additives. *ACS Nano*, 6(3):2804–2817, February 2012.
- [156] Ana Sánchez-Iglesias, Marek Grzelczak, Jorge Pérez-Juste, and Luis M Liz-Marzán. Binary self-assembly of gold nanowires with nanospheres and nanorods. *Angewandte Chemie International Edition*, 49(51):9985–9989, December 2010.
- [157] T Ming, X S Kou, H J Chen, T Wang, H L Tam, K W Cheah, J Y Chen, and J F Wang. Ordered Gold Nanostructure Assemblies Formed By Droplet Evaporation. *Angewandte Chemie International Edition*, 47(50):9685–9690, 2008.
- [158] Yasutaka Nagaoka, Tie Wang, Jared Lynch, Derek LaMontagne, and Y Charles Cao. Binary assembly of colloidal semiconductor nanorods with spherical metal nanoparticles. *Small*, 8(6):843–846, March 2012.
- [159] Taejong Paik and Christopher B Murray. Shape-Directed Binary Assembly of Anisotropic Nanoplates: A Nanocrystal Puzzle with Shape-Complementary Building Blocks. *Nano Letters*, 13(101):2952–2956, May 2013.
- [160] P Davide Cozzoli, Andreas Kornowski, and Horst Weller. Low-temperature synthesis of soluble and processable organic-capped anatase TiO₂ nanorods. *Journal of the American Chemical Society*, 125(47):14539–14548, 2003.
- [161] Catherine J Murphy, Tapan K Sau, Anand M Gole, Christopher J Orendorff, Jinxin Gao, Linfeng Gou, Simona E Hunyadi, and Tan Li. Anisotropic metal nanoparticles: Synthesis, assembly, and optical applications. *Journal of Physical Chemistry B*, 109(29):13857–13870, 2005.
- [162] Tie Wang, Jiaqi Zhuang, Jared Lynch, Ou Chen, Zhongliang Wang, Xirui Wang, Derek LaMontagne, Huimeng Wu, Zhongwu Wang, and Y Charles Cao. Self-Assembled Colloidal Superparticles from Nanorods. *Science*, 338(6105):358–363, 2012.
- [163] Peter Bolhuis and Daan Frenkel. Numerical study of the phase diagram of a mixture of spherical and rodlike colloids. *Journal of Chemical Physics*, 101(11):9869–9875, 1994.

- [164] Tomonori Koda, Manabu Numajiri, and Susumu Ikeda. Smectic-A Phase of a Bidisperse System of Parallel Hard Rods and Hard Spheres. *Journal of the Physics Society Japan*, 65(11):3551–3556, November 1996.
- [165] M Adams and S Fraden. Phase behavior of mixtures of rods (tobacco mosaic virus) and spheres (polyethylene oxide, bovine serum albumin). *Biophysical Journal*, 74(1):669–677, January 1998.
- [166] G A Vliegenthart and H N W Lekkerkerker. Phase behavior of colloidal rod-sphere mixtures. *Journal of Chemical Physics*, 111(9):4153–4157, 1999.
- [167] Z Dogic, D Frenkel, and S Fraden. Enhanced stability of layered phases in parallel hard spherocylinders due to addition of hard spheres. *Physical Review E*, 62:3925–3933, September 2000.
- [168] Matthias Schmidt. Density functional theory for colloidal rod-sphere mixtures. *Physical Review E*, 63(5):1–4, April 2001.
- [169] Dmytro Antypov and Douglas J. Cleaver. Orientational and phase-coexistence behaviour of hard rod-sphere mixtures. *Chemical Physics Letters*, 377(3-4):311–316, August 2003.
- [170] Dmytro Antypov and Douglas J Cleaver. The role of attractive interactions in rod-sphere mixtures. *Journal of Chemical Physics*, 120(21):10307–10316, June 2004.
- [171] S K Lai and Xuhui Xiao. Phase diagram of colloid-rod system. *Journal of Chemical Physics*, 132(4):044905, January 2010.
- [172] Alexey V Titov and Petr Král. Modeling the self-assembly of colloidal nanorod superlattices. *Nano Letters*, 8(11):3605–3612, 2008.
- [173] Mihir R Khadilkar and Fernando A Escobedo. Self-assembly of binary space-tessellating compounds. *The Journal of chemical physics*, 137(19):194907, November 2012.
- [174] Ludovico Cademartiri, Kyle J M Bishop, Phillip W Snyder, and Geoffrey A Ozin. Using shape for self-assembly. *Philosophical Transactions Series A*, 370(1969):2824–47, June 2012.
- [175] Adam B. Hopkins, Frank H. Stillinger, and Salvatore Torquato. Densest binary sphere packings. *Physical Review E*, 85(2):021130, February 2012.
- [176] B. Derjaguin. Untersuchungen über die Reibung und Adhäsion, IV. *Kolloid-Zeitschrift*, 69(2):155–164, November 1934.
- [177] Lee R White. On the Deryaguin approximation for the interaction of macrobodies. *Journal of Colloid and Interface Science*, 95(1):286–288, September 1983.

- [178] S.C. Kapfer and W. Krauth. Two-step melting in two dimensions: First-order liquid-hexatic transition. *Phys. Rev. Lett.*, 107:155704, Oct 2011.